Innovative Pavement Research Foundation (IPRF)
IPRF – Project 04-02

Final Report

Improved Overlay Design Parameters for Concrete Airfield Pavements

(IPRF Project FAA-01-G-002-04-2)

Submitted by

Quality Engineering Solutions, Inc.
405 Water Street, PO Box 3004
Conneaut Lake, PA 16316
Phone: (814) 382-0373
Fax: (814) 382-0375
www.QESpavements.com

Quality Engineering Solutions

Engineering • Inspection • Construction

Innovative Pavement Research Foundation (IPRF)
IPRF – Project 04-02

Final Report

Improved Overlay Design Parameters for Concrete Airfield Pavements
(IPRF Project FAA-01-G-002-04-2)

Principal Investigator

Shelley Stoffels, D.E.
The Pennsylvania State University

Contributing Authors
Dennis Morian, P.E., Quality Engineering Solutions, Inc.
Anastasios Ioannides, Ph.D., P.E., University of Cincinnati
Shie-Shin Wu, Ph.D., P.E., Pavement Consultant
Suri Sadasivam, Ph.D., Quality Engineering Solutions, Inc.
Lin Yeh, The Pennsylvania State University
Hao Yin, Ph.D., The Pennsylvania State University

June 2008

This report has been prepared by the Innovative Pavement Research Foundation under the Airport Concrete Pavement Technology Program. Funding is provided by the Federal Aviation Administration under Cooperative Agreement Number 01-G-002. Dr. Satish Agarwal is the Manager of the FAA Airport Technology R&D Branch and the Technical Manager of the Cooperative Agreement. Mr. Jim Lafrenz is the Program Director for the IPRF.

The Innovative Pavement Research Foundation and the Federal Aviation Administration thank the Technical Panel that willingly gave of their expertise and time for the development of this report. They provided oversight and technical direction to the research team. Members of the Technical Panel for this project include:

Mr. Adil M. Godiwalla, P.E., R.P.S.	Houston Airport System
Mr. Carl Rapp, P.E.	CRD & Associates, Inc.
Mr. Ray Rollings	Pavement Engineering Consultant
Mr. Dean Rue, P.E.	CH2M Hill Aviation
Dr. Gordon Hayhoe, P.E.	National Airport Pavement Research Center
Mr. Edward L. Gervais, P.E.	Boeing Airport Technology Group

LIST OF ACRONYMS

ABG - Allemeine Baumashinin Gesellchaft paving machine

AC – Asphalt Concrete

ASTM – American Society for Testing and Materials

BDF - Bridge Deck Finisher

CBR – California Bearing Ratio

CMS – Curing Monitoring System

FAA - Federal Aviation Administration

HWD – Heavy Falling Weight Deflectometer

KSI – Thousand Pounds per Square Inch

LPT – Linear Position Transducer

LTE – Load Transfer Efficiency

MUX – Multiplexor

NAPTF - National Airfield Pavement Test Facility

PCI – Pounds per Cubic Inch

PSI – Pounds per Square Inch

PVC – Polyvinyl Chloride

QC – Quality Control

QES – Quality Engineering Solutions

SCI - Structural Condition Index

SPU – Signal Processing Unit

TTI - Texas Transportation Institute

TABLE OF CONTENTS

Page

TABLE OF CONTENTS (cont'd)

TABLE OF CONTENTS (cont'd)

Page

TABLE OF CONTENTS (cont'd)

LIST OF FIGURES

Page

LIST OF FIGURES (cont'd)

Page

LIST OF FIGURES (cont'd)

Page

LIST OF TABLES

Page

LIST OF TABLES (cont'd)

Page

1. INTRODUCTION.

1.1 PURPOSE.

The Innovative Pavement Research Foundation (IPRF) has an objective of improving the current understanding of the influence of design parameters on unbonded concrete overlays of airfield pavements, thus enabling improvement of design methodologies. In 2005, IPRF contracted for this study to prioritize the necessary research and technology activities for the design of unbonded concrete overlays for airfields. The four major project components were:

- Identification of the factors that affect performance of airfield unbonded concrete overlays.

- Development of an experimental roadmap for research and technology activities to achieve the long-term goal of providing an improved unbonded overlay design methodology for airfield pavements, through a series of full-scale tests at the Federal Aviation Administration (FAA) National Airfield Pavement Test Facility (NAPTF).

- Construction of the first series of test items for full-scale testing, the first stage in the roadmap, at the NAPTF and performance of subsequent testing.

- Documentation and summarization of the data, and preliminary analysis to support the overall roadmap progress, which can be used to improve mechanistic design models for unbonded concrete overlays.

1.2 BACKGROUND.

Airport pavements have been constructed using portland cement concrete pavement for many decades. While these pavements perform well, eventually all pavements require rehabilitation or replacement. An unbonded concrete overlay offers an attractive alternative for several reasons. One reason is that by leaving the existing pavement in place, the in situ conditions of subgrade and base layers are essentially undisturbed, minimizing any opportunity for additional consolidation or settlement to take place during use. Another very advantageous reason is that the existing pavement can be taken into consideration in structural design, typically resulting in a thinner and less costly required pavement layer.

Unbonded overlays have been used successfully in the past, and yet much is still unknown about the mechanisms by which they perform, and consequently room for improvement exists for design procedures. Past researchers, including Rollings (1988) recognized the need for additional controlled performance data. Advanced design procedures, including those developed by the FAA (Brill, 2003 and Guo, 2005), allow greater precision in design, but require supporting calibration data. Again, this opportunity indicates that additional cost savings can be realized in the form of design improvements and enhanced performance. The current design program for the FAA, FAARFIELD, is an example of such an advanced methodology.

One of the major issues, both in considering the feasibility of rehabilitation with an unbonded overlay and in the thickness design methodology, is the condition of the existing pavement. Rollings (1988) developed the Structural Condition Index (SCI) based upon visual surveys of the pavement condition. The SCI considers only structural distresses, not surface distresses, and is used to modify the stiffness of the existing pavement in the overlay design methodology. Examination of the SCI in the context of mechanistic-empirical design is a major component of this research.

Other issues of perhaps even more fundamental value in improving the understanding of the performance of unbonded overlays were also to be considered. Those factors included the relative thickness of the overlay and underlay, the correspondence between predicted and measured responses, and the relationship of the failure mechanisms in the existing pavement and overlay. Additional design issues include the matching of joints, interlayer and bond.

In 2001, the IPRF undertook a research project to develop an experimental design plan to be conducted at the FAA NAPTF. The result of that effort was the FAA/IPRF report *Improved Concrete Overlay Parameters for Airfield Pavements* (Khazanovich, 2001). This study was initiated to refine that plan by dividing it into executable stages, and then completing the first of those smaller experiments.

1.3 ROADMAP.

The development of the unbonded concrete overlay roadmap utilized dimensional analysis to help characterize the design and input parameters that have the greatest impact on pavement responses. The benefit of dimensional analysis is that the multitude of variables, and their permutations, can be reduced to a smaller series of dimensionless parameters. Those parameters make it possible to examine a broad range of potential variable values without constructing the full factorial of test items with different thicknesses and other conditions. The dimensionless parameters, as identified and ranked, are summarized in table 1. Full details of the development of the parameters are included in *Improved Overlay Design Parameters for Concrete Airfield Pavements, 20% Report* (2006).

With consideration of these parameters, the roadmap was divided into three expected construction cycles of full-scale testing accelerated testing experiments. These construction and testing steps were not designed to test and study three unique and separate performance or design issues, but rather to provide as much as possible of the overall needed information in an incremental and efficient manner. The test items proposed for each construction step were developed to test for realistic values of the dimensionless parameters in table 1, while covering much of the reasonable range. However, in order to meet the facility constraints, the proposed cross-sections are on average thinner than typical for overlaid airfields. The proposed objectives and parameters for the experiments are briefly summarized in table 2.

TABLE 1. RANKED DIMENSIONLESS EXPERIMENTAL PARAMETERS

1. Structure and Condition Parameters $E_{ol}h_{ol}/E_{sl}h_{sl}$ – Primary h_{ol}/h_{sl} and E_{ol}/E_{sl} – Secondary	h_{ol} and h_{sl} = Overlay and underlying slab thicknesses, respectively. E_{ol} and E_{sl} = Overlay and underlying slab elastic moduli, respectively. X_T and X_L = Transverse joint and longitudinal joint offsets, respectively ℓ = Radius of relative stiffness $= [(E_{ol}*(h_{ol}^3+(E_{sl}/E_{ol})*h_{sl}^3))/(12*(1-\mu)*k)]^{0.25}$ μ = Poisson's ratio = 0.15 k = Modulus of subgrade reaction ESWR = Equivalent Single Wheel Radius AGG = Stiffness of the elastic joint D = Composite (springs in a series) shear stiffness of the joint s = Dowel spacing heW = In situ (working) effective thickness, determined from HWD testing heB = Effective thicknesses assuming fully bonded conditions heU = Effective thicknesses assuming no bond
2. Discontinuity Parameters x_L / ℓ x_T / ℓ	
3. Gear Configuration Variables ESWR / ℓ	
4. Load Transfer Parameters AGG/(k* ℓ) – undoweled joints D/ (s*k* ℓ) – doweled joints	
5. Support Variables k*ℓ	
6. Interlayer/Adhesion Parameters (heW-heU)/(heB-heU) heU/h_{ol} $(heU/h_{sl})* (E_{ol}/E_{sl})$	

Though the roadmap and research program for testing unbonded concrete overlays for rigid airfield pavements at NAPTF will give many results, the overreaching goals are to:

- Improve the understanding of how underlying pavement's condition affects the unbonded overlay's performance.
- Verify whether the measured responses match the predicted responses from the current models and overlay design methods.
- Refine the relationship between the underlying pavement's condition (E-value of the underlying slab) and the structural condition index (SCI) by comparing predicted and actual response data.
- Quantify the differences in responses (strains, pressures, and deflections) and the resulting impacts on failure criteria between dual tandem and triple dual tandem gears on unbonded overlay performance.
- Improve the understanding of the interaction between the unbonded overlay's system layers (original pavement, interlayer, and overlay).

There are several issues related to testing of unbonded concrete overlays at NAPTF that may be important for the design and construction of unbonded overlays that this roadmap does not address. These issues are not included because the project team does not consider those issues to be feasible or desirable for a full-scale testing facility such as the NAPTF.

TABLE 2. ROADMAP OVERVIEW

Objectives	Approach	Variables	Values
I. Baseline Experiment • Verify Composite Action of Overlay and Underlying Slabs • Calibrate/Validate Structural Responses • Calibrate/Validate Gear Effects • Verify Failure Mechanisms • Formulate Overall "Life Prediction" • Determine Effects of Discontinuities (Mismatched Joints and Cracks) on Stresses and Deflections	• Use medium subgrade only. • Construct underlying pavement; measure responses. • Joints in underlying pavement will be utilized to model both joints and cracks (no dowels). • Construct overlay; measure responses; load to failure. • Remove overlay; examine condition of underlay.	$E_{ol}h_{ol}/E_{sl}h_{sl}$	0.60, 1.0, 1.50 ($E_{ol} = E_{sl} = 4x10^6$ psi)
		Long. Jt. Offset	4 ft.
		Trans. Jt. Offset	0 ft., 1 ft. & 4 ft.
		Gear Configuration and Weight	Dual tandem, triple dual tandem 10,000 lb to 60,000 lb
		Subgrade Support	Medium subgrade
		Load Transfer	Overlay – Doweled Underlay – No dowels
		Interlayer Adhesion	Minimize bonding

II. Structural Condition Index Study
• Determine Effects of Underlying Condition on Overlay Response:
  • Different levels of SCI
  • Effects of specific distress types
  • Examine varying effect of SCI w/ load and subgrade interactions (low, medium CBR)
• Determine Effects of Load Transfer:
  • Effect on structural response
  • Examine impacts on failure and distress
	• Re-use baseline pavement. Replace/ repair, as necessary.
	• Induce SCI levels and distress modes.
	• Add adjacent test items on low subgrade.
	• Construct new overlay over all and load to failure.
	• Remove overlay and examine condition of underlay.
		$E_{ol}h_{ol}/E_{sl}h_{sl}$	1.14 – 3.75 ($E_{ol} = 4x10^6$ psi)

		Target SCI Levels	40, 60, 80 (Baseline results)
		SCI Distress Modes	Surface, cracking, shattered
		Long. Jt. Offset	0 and 4 ft.
		Trans. Jt. Offset	0 ft., 1 ft. & 4 ft.
		Gear Configuration and Weight	Dual tandem, triple dual tandem 10,000 to 60,000 lb
		Subgrade Support	Low, medium subgrade
		Load Transfer	Overlay – Some doweled
		Interlayer Adhesion	Minimize bonding

III. Effects of Underlying Condition
• Examine Varying Effects of SCI with Load and Subgrade Interactions (medium and high CBR)
• Examine Effects of Interlayer Design:
  • Determine effects of interlayer thickness
  • Determine effects of interlayer adhesion
	• Re-use portion of underlying pavement, if possible. Replace/ repair, as necessary.
	• Induce distress & SCI levels.
	• Add adjacent test items on high subgrade.
	• Construct new overlay over all and load to failure.
	• Remove overlay and examine condition of underlying pavement.
		$E_{ol}h_{ol}/E_{sl}h_{sl}$	0.69 – 2.4 ($E_{ol} = 4x10^6$ psi)

		SCI Levels	30 – 80 (SCI Study results)
		SCI Distress Modes	Cracking, shattered slabs
		Long. Jt. Offset	0 and 4 ft.
		Trans. Jt. Offset	0 ft., 1 ft. & 4 ft.
		Gear Configuration and Weight	Dual tandem, triple dual tandem 10,000 lb to 60,000 lb
		Subgrade Support	Medium and High Subgrade
		Load Transfer	Overlay – Some doweled
		Interlayer Adhesion	1 to 4 in. separation course No bond breaking actions

Issues not addressed in the roadmap include:

- The impact of environmental factors, such as temperature cycles and precipitation. Humidity and temperature will be documented within the facility and within the pavement cross-sections. The concrete will be wetted regularly to avoid excessive drying shrinkage. The facility is not temperature controlled, and no attempt will be made to simulate any seasonal variations.
- The impact of variations in subbase, interlayer and concrete materials will not be explored in the full-scale testing. These materials will be as uniform as possible throughout the phases of the proposed testing, and will be as representative of "typical" materials as is feasible.
- Various loading speeds will not be employed. While faster loading speeds may have the effect of creating a stiffer interlayer response, thus creating more of a bonded overlay effect, the testing speed will be held constant at three mph.
- While slab size may have some effect on stress distributions and overlay performance, the slabs will be held at a relatively constant size. The limitations on slab thickness make larger slabs problematic, while the size of the loading gears makes smaller slabs unrealistic.
- The performance of overlays may be significantly impacted by the differences between as-designed and as-constructed characteristics. The construction conditions within the NAPTF differ substantially from those in the field, making it an unrealistic laboratory for the exploration of such issues.
- A wander pattern that has been determined as typical will be utilized for the majority of the testing, and for all of the fatigue testing to failure. Variation of wander pattern is not anticipated during the full-scale testing.
- Partially bonded overlays will not be considered within the testing plan.

1.4 THE BASELINE EXPERIMENT.

During the development of the roadmap, it was determined that in order to mechanistically model different SCI values and underlying pavement conditions, it was first necessary to mechanistically model stresses, strains, and deflections for differing discontinuity (joints and/or cracks) conditions in both the overlay and underlying slab. These underlying discontinuity conditions include intact slabs with matched joints, intact slabs with mismatched joints, and various degrees of match/mismatch, simulating a substantially deteriorated underlying slab. Therefore, the first stage of the roadmap, called the Baseline Experiment, was designed to verify responses to these conditions.

The Baseline Experiment consists of a 300-foot test pavement that has three structural cross-sections and is constructed on the medium subgrade. The underlying slabs were not designed to be distressed (no shattered or cracked slabs), but to have different joint matching conditions to determine how underlying discontinuities (including cracks) affect the overlay's performance. In addition to determining how underlying discontinuities affect the overlay's performance, this allows investigation of deterioration of the underlying pavement due to overlay loading.

The Baseline Experiment is intended to address the following four questions:

- How does the overlay respond?
- How do underlying discontinuities affect overlay response?
- What is the relative deterioration of the overlay and underlying pavement after loading?
- How do the overlay and underlying pavement deteriorate, in terms of distress and structural response, as compared to Rollings' SCI model?

The design of the Baseline Experiment drew from the information assembled during the roadmap activity. A refined design matrix was developed, specific to the Baseline Experiment conditions. Further, it was determined that it was not reasonable to attempt to address too many parameters at once. A finite space was available for the experiment construction. When practical joint spacing was considered, it became clear that it would be necessary to limit the number of variables addressed, particularly when replication of factors was considered. Constraints are provided by the physical geometry of the test area, the loading range of the loading device, and the necessity to develop cross-sections that could be failed by repetitive loading within a reasonable testing time.

The analysis for this experiment will focus on these aspects:

- Verification of the mechanistic strain predictions in the unbonded overlay,
- Verification of the effects on overlay response of an underlying discontinuity,
- Verification of the failure mechanisms and relative deterioration of the overlay,
- Comparison of the predicted loads to failure with the experimental observations, and
- Verification of the deterioration of the failure mechanisms and distress in the underlying pavement, as a result of the traffic loading.

For the Baseline Experiment, it was not possible to include some of the variables contained in the roadmap, for example high and low strength subgrades. The predominant factors were determined to be the ratios of combined slab thickness and concrete elastic modulus factors for the underlying and overlay slabs. The same concrete mix was used for the construction of both top and bottom slabs, so the initial elastic modulus values were constant. The project team also considered it important to address the effect of joints and cracks being matched or mismatched in the overlying slab. After consideration of this condition, it was concluded that by creating a significant weakened plane, cracks and joints could both be reasonably modeled as the same condition. A D/2 saw cut was determined to be a reasonable means of introducing this discontinuity into the bottom slab. The interface condition was established as a single partially bonded level determined by the asphalt interlayer. For the Baseline Experiment, the interface condition remained constant.

Loading was planned using both dual tandem and triple dual tandem gears, therefore it was important that the pavements constructed perform in a reasonable manner, and fail in a reasonable number of passes, for both configurations. Extensive analysis was conducted using a variety of programs and fatigue equations, including the FAA programs, FEDFAA and LEDFAA, and the finite element program, EverFE. The details of the analysis are documented in *Improved Overlay Design Parameters for Concrete Airfield Pavements, 20% Report* (2006).

A number of cross-sections were evaluated, incorporating appropriate values of the dimensionless parameters, and integrating those with the physical testing constraints. Other constraints included the load capacity of the test vehicle (approximate maximum wheel load of 60,000 pounds), elevation constraints such that both the top and bottom slabs could be loaded with the test vehicle, joint spacing constraints such that the gear load could be accommodated on each slab, reasonable ratios of slab thickness and size with regard to design practices and the avoidance of curl and corner breaks, dowel requirements on thin overlay sections including bearing stress considerations, edge constraints in the 60-foot wide facility, and the need to provide for redundancy in both the test slabs and instrumentation. Another constraint was the need to have enough slabs in each test item to be able to calculate meaningful values of SCI.

The risks and consequences of various test item designs were carefully tabulated and considered. The final design for the Baseline Experiment consists of six test items, in three structural sections of varying thicknesses constructed on the medium-strength subgrade. The test items are separated by transition slabs in both the longitudinal and transverse directions. By providing two test items in each structural section, different loading configurations could be applied. The final experimental configuration is illustrated in figure 1 and figure 2. Figure 1 shows the three structural cross-sections, numbered 1, 2 and 3 from west to east. Figure 2 shows the transverse cross-section, indicating that each test item has two 12.5-ft wide lanes, with a 10-ft transition slab between the test items. The test items are also summarized in table 3. Each test item consists of 12 slabs. The overlay slabs were designed with both longitudinal and transverse dowels, but not doweled to the longitudinal transition slabs. The underlay slabs were designed to be undoweled to provide greater discontinuities in support. The design passes for the final cross-sections, for various programs and equations, varied from 1 to 7500 passes of a 60,000-lb wheel load.

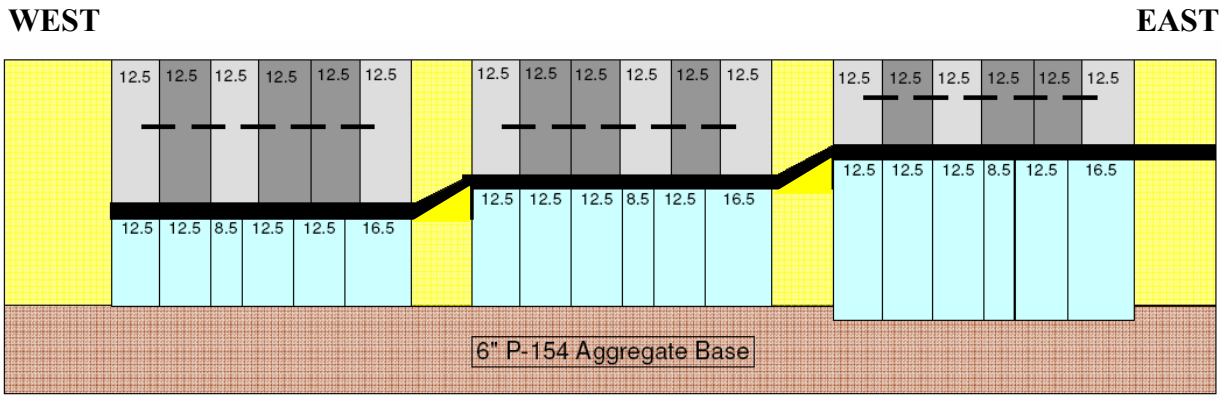

FIGURE 1. EXPERIMENTAL DESIGN CONFIGURATION, SHOWING TRANSVERSE JOINT SPACINGS

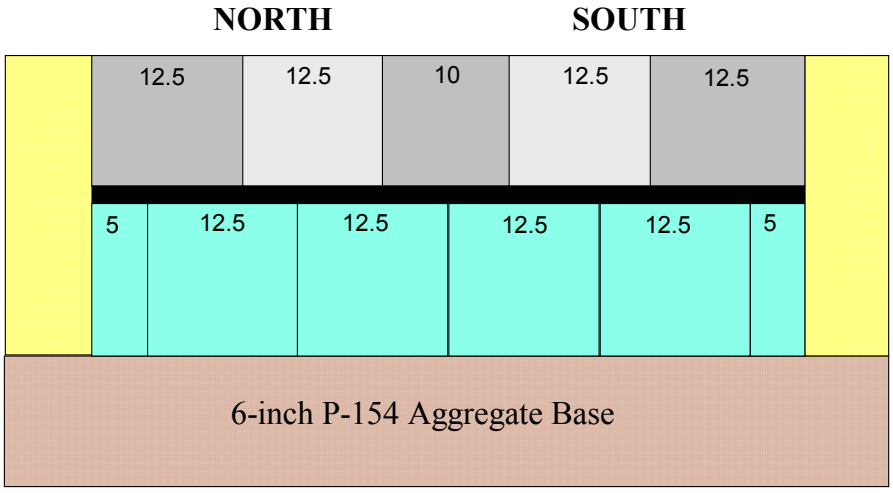

FIGURE 2. END VIEW OF LONGITUDINAL JOINT LOCATIONS FOR OVERLAY AND UNDERLAY SLABS

TABLE 3. SUMMARY OF DESIGN TEST ITEMS FOR BASELINE EXPERIMENT

Test Item Designation	Design Overlay Thickness (in)	Design Underlay Thickness (in)	Planned Gear Loading
North 1 (N1)	9	6	Triple Dual Tandem
South 1 (S1)	9	6	Dual Tandem
North 2 (N2)	7.5	7.5	Triple Dual Tandem
South 2 (S2)	7.5	7.5	Dual Tandem
North 3 (N3)	6	10	Triple Dual Tandem
South 3 (S3)	6	10	Dual Tandem

2. CONSTRUCTION AND INSTRUMENTATION.

2.1 CONSTRUCTION.

The design-build process used to develop the experiment streamlined the design and construction time and cost, and eliminated the need to advertise, evaluate, and contract a third party contractor. It also gave a single point responsibility to QES for the project and improved the likelihood for success by consolidating decision making and the conduct of the work.

The construction of the IPRF unbonded overlay Construction Cycle 4 (CC4) Baseline Experiment took place between November 2005 and May 2006. This construction schedule had some advantages, including the availability of construction crews and loading during warm weather. The division of the construction effort between the FAA and QES was clearly defined. The FAA was responsible for the subgrade preparation, and QES was responsible for all construction above the subgrade. Table 4 shows the overall construction schedule.

TABLE 4. CC4 CONSTRUCTION SCHEDULE

Activity	**Date**
Subgrade preparation by FAA	Nov. 28, 2005 – Jan. 24, 2006
Subbase construction	Jan. 31 - Feb. 2, 2006
Underlying pavement instrumentation	Feb. 13 – 17
Underlying pavement construction set up (forms, paver, & other mob activities)	Feb. 20 – 23
Paving of underlying pavement	Feb. 27 – 28
Cut joints	Feb. 28 – Mar. 2
Curing of underlying pavement	Feb. 28 – Mar. 10
Underlying slab testing	Mar. 13 – 16
Overlay instrumentation	Mar. 20 – 24
AC interlayer paving	Mar. 22
Overlay pavement construction set-up	Mar. 27 – 28
Overlay concrete paving	Mar. 29
Cut joints	Mar. 29 – 30
Demobilization	Mar. 30 – 31
Curing of overlay pavement	Mar. 30 – May 8
Overlay surface instrumentation	May 8 – 12
Final construction activities (shoulder fill, insert backer rod, etc)	May 8 – 12

2.1.1 Subgrade Preparation.

The FAA prepared the medium-strength subgrade for CC4 between November 28, 2005 and January 23, 2006. The subgrade target CBR value was 8 with a tolerance of -2 to +1 (range from 6 to 9). The final elevation was located at -23 inches below the zero point, which is elevation 56.08 at the facility.

Based upon testing completed by the FAA, the calculated and estimated ranges for the CBR were within the established criteria. Consequently, it was determined, based on prior experience, that it would only be necessary to rework the top of subgrade. The procedure used by the FAA to achieve the required results included trimming to final grade, tilling to a minimum depth of 12 inches, monitoring moisture content, and making adjustments until the target CBR value was achieved. The vane shear test was used to check material uniformity during the operation, and final in-place CBR tests were conducted upon completion. The final CBR subgrade values are shown in table 5.

TABLE 5. FINAL SUBGRADE CBR VALUES

Lot ID	Test Item	Sublot ID	Test ID	Station	Lane	CBR	Test Avg.	Lot Avg.	Moisture, %
Lot 1	1	A	1	369	North	8.0	7.9	7.9	
			2	369	North	7.6			30.01
			3	369	North	8.1			
	2	B	1	464	North	8.2	7.5		
			2	464	North	6.8			29.26
			3	464	North	7.5			
	3	C	1	572	North	9.2	8.4		
			2	572	North	8.1			30.64
			3	572	North	8.0			
Lot 2	1	A	1	369	South	7.0	7.7	8.0	
			2	369	South	7.5			30.04
			3	369	South	8.5			
	2	B	1	454	South	7.5	7.6		
			2	454	South	7.5			29.6
			3	454	South	7.7			
	3	C	1	568	South	8.0	8.8		
			2	568	South	9.0			29.45
			3	568	South	9.4			
					High	**9.4**	**8.8**	**8.0**	
					Low	**6.8**	**7.5**	**7.9**	

The subgrade was left 2 inches above the final subgrade elevation as a means of protecting the final elevation's subgrade condition between the end of the subgrade construction and the beginning of the base construction. Previous work at NAPTF has shown that the immediate surface's condition shifts due to condensation under the plastic sheeting or drying if the air gets very cold and dry; but, that this effect is confined to the immediate surface only as long as it is

only for a short duration (i.e., a couple of weeks). Just prior to base construction, the FAA trimmed the subgrade to the final elevation. Results were within +/- ¾" of the design grade.

Final subgrade elevations were determined by completing a rod and level survey of the entire test area on a 10 ft. by 10 ft. grid. Table 6 shows the subgrade elevation deviations, in inches from the target value of 56.08. Figure 3 shows the same information graphically, except the results are expressed in feet.

TABLE 6. DEVIATION OF CC4 SUBGRADE FROM TARGET ELEVATION (EI = 56.08 FT), INCHES

	Offset (ft)						
Station	**-30**	**-20**	**-10**	**0**	**10**	**20**	**30**
320	0.32	0.08	0.08	-0.16	-0.04	0.20	0.32
330	-0.76	-0.04	0.44	0.08	-0.64	0.08	-0.40
340	-0.28	0.08	0.20	0.20	-0.04	0.08	0.68
350	0.56	-0.28	0.32	0.20	0.08	0.08	0.08
360	-0.40	-0.40	0.20	-0.04	0.20	-0.04	-0.52
370	0.92	0.08	0.44	0.20	-0.40	-0.04	0.20
380	0.68	0.44	0.44	0.32	-0.16	0.08	0.80
390	0.44	0.44	0.68	0.68	-0.40	-0.04	0.08
400	0.80	0.32	-0.40	-0.64	0.44	-0.40	0.20
410	0.44	0.20	-0.04	0.44	-0.28	-1.00	-0.04
420	0.08	0.44	0.20	-0.16	0.32	0.44	-0.04
430	0.92	0.08	0.20	0.44	0.44	-0.28	0.08
440	0.92	0.44	0.20	0.80	-0.16	-0.64	0.20
450	1.28	0.56	0.56	0.80	0.32	0.20	0.08
460	0.80	0.32	0.56	0.20	-0.04	0.32	0.08
470	0.44	0.68	0.92	0.44	-0.28	-0.04	0.20
480	0.92	0.56	0.44	0.08	0.32	0.08	0.32
490	0.80	0.44	1.16	0.80	0.44	0.32	0.20
500	1.04	0.80	0.44	0.32	0.32	-0.16	0.92
510	0.32	0.92	0.56	0.80	0.32	0.32	0.44
520	0.20	1.16	1.28	0.44	-0.04	0.08	-0.04
530	0.20	0.32	0.68	0.08	0.68	0.08	0.20
540	-0.04	0.92	0.80	0.32	0.44	0.20	0.80
550	0.68	0.56	0.80	0.44	0.68	0.44	0.80
560	0.32	1.04	0.56	0.56	0.32	0.32	0.44
570	0.92	0.80	0.20	0.56	1.04	0.80	0.80
580	1.64	0.68	0.32	0.80	0.56	0.44	0.80
590	1.40	0.80	-0.28	-0.04	0.32	-1.00	0.32

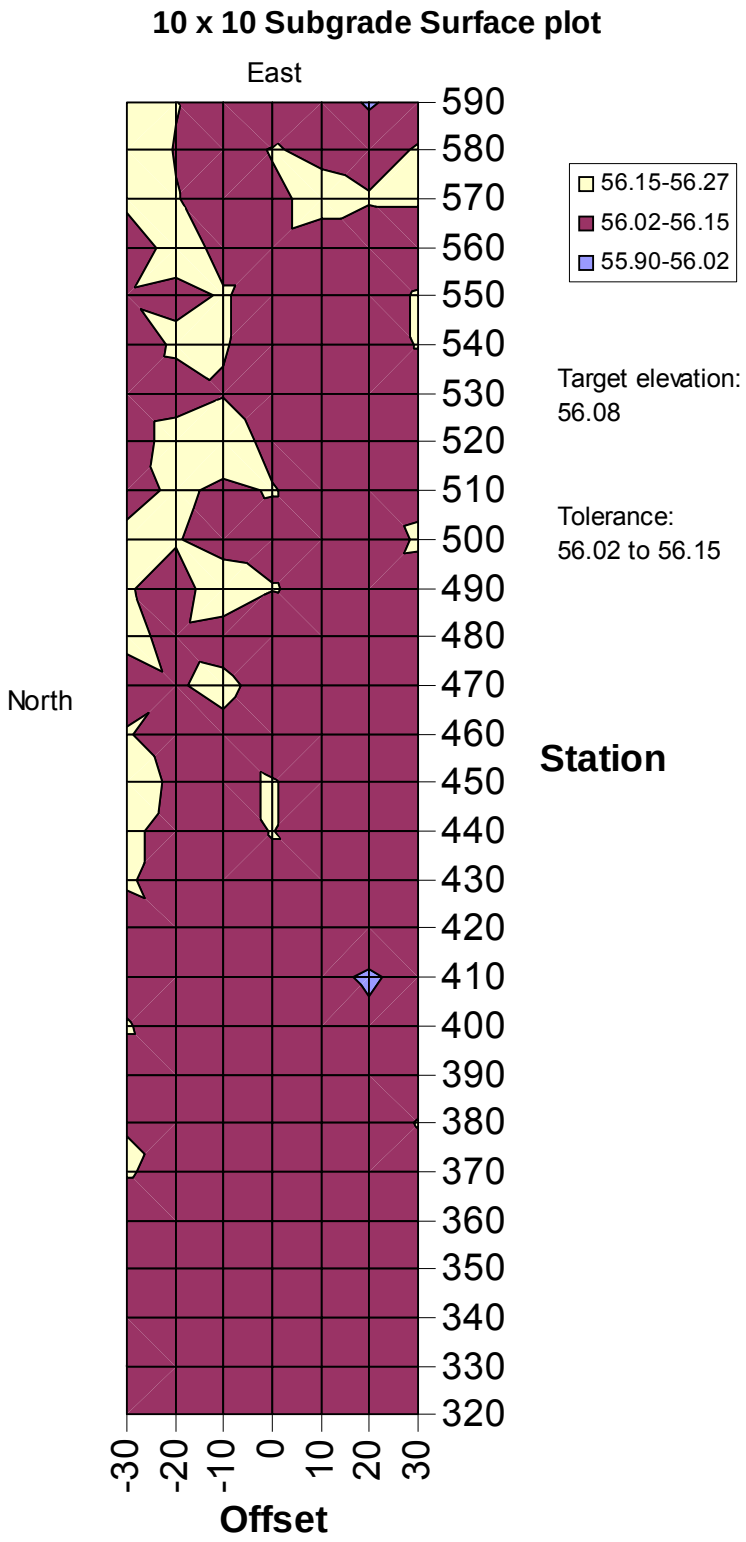

FIGURE 3. ELEVATION (FT) OF CC4 SUBGRADE (TARGET ELEVATION = 56.08 FT)

2.1.2 Base Construction.

A P-154 granular base course was placed on the FAA-prepared subgrade on February 1, 2006. Laser level control was used to establish the finished base grade. The equipment used included a dozer and vibratory roller. It was originally planned to place this material with an Allemeine Baumashinin Gesellchaft (ABG) machine, but there was concern that the subgrade would not support the equipment, so the alternate plan was used. As a result of the process used for spreading the material, some material segregation was experienced, and the final grade variation was slightly greater than was hoped for, but remained within acceptable "real world" construction tolerance. However, subsequent inspection found that this segregation was isolated in the top layer of the aggregate base and seemed to occur most during the trimming operation.

Moisture, gradation, and density testing were conducted on the basis of 50 square yard sublots, to control the base material and placement. Gradation samples showed the material to be slightly finer between the 2 and 5 mm particle sizes (sieves No. 4 and No. 8) than the P-154 specification limit. Samples were taken from the unloaded stockpiles, and while stockpile sampling techniques were used, the observed segregation may have affected the gradation test results, as the stockpiles were dynamic throughout placement. The average density was 94.9 percent, and the average moisture content was 4.6 percent. The moisture content was slightly lower than the optimum moisture value established by Proctor testing, but acceptable density was achieved.

The target base elevations for structural sections 1 and 2 were set at 56.58 feet, which corresponds to a 6-inch base. The target elevation for structural section 3 was set at 56.5 feet, which corresponds to a 5-inch base. This was done so that the finished overlay slab surface would be at the same elevation for all three structural sections. As with the subgrade, the final elevations were determined by a rod and level survey of the entire test area on a 10 ft by 10 ft grid. Figure 4 shows the final base elevations expressed in feet.

Using the rod and level surveys from both the subgrade and base courses, it is possible to get an indication of the base thickness over the entire grid. As illustrated in table 7, the average base thickness for all three test areas is slightly low, although the ranges are reasonable.

Moisture and density testing were used to control the compaction effort and to ensure the base was compacted at the appropriate levels. From the material supplier (National Paving Co. Inc., Berlin, NJ), maximum density was 139.1 lbs/ft^3 at a moisture content of 5.5 percent. QES performed Proctor testing to confirm this. Base construction started on the west end and proceeded east. Since the as-delivered material was very dry, moisture was added to the base materials during placement in order to reach target density (95 percent of Proctor). This was initially accomplished using the NAPTF Bridge Deck Finisher (BDF) which worked well until the machine had mechanical problems. Hand watering was used to complete the compaction process. This process was suspected of producing uneven moisture contents, with some areas being significantly wetter than others. Therefore, the base course was covered and allowed to "even out" for 10 days. At that point, the base was re-rolled to achieve final density. Table 8 shows the final results.

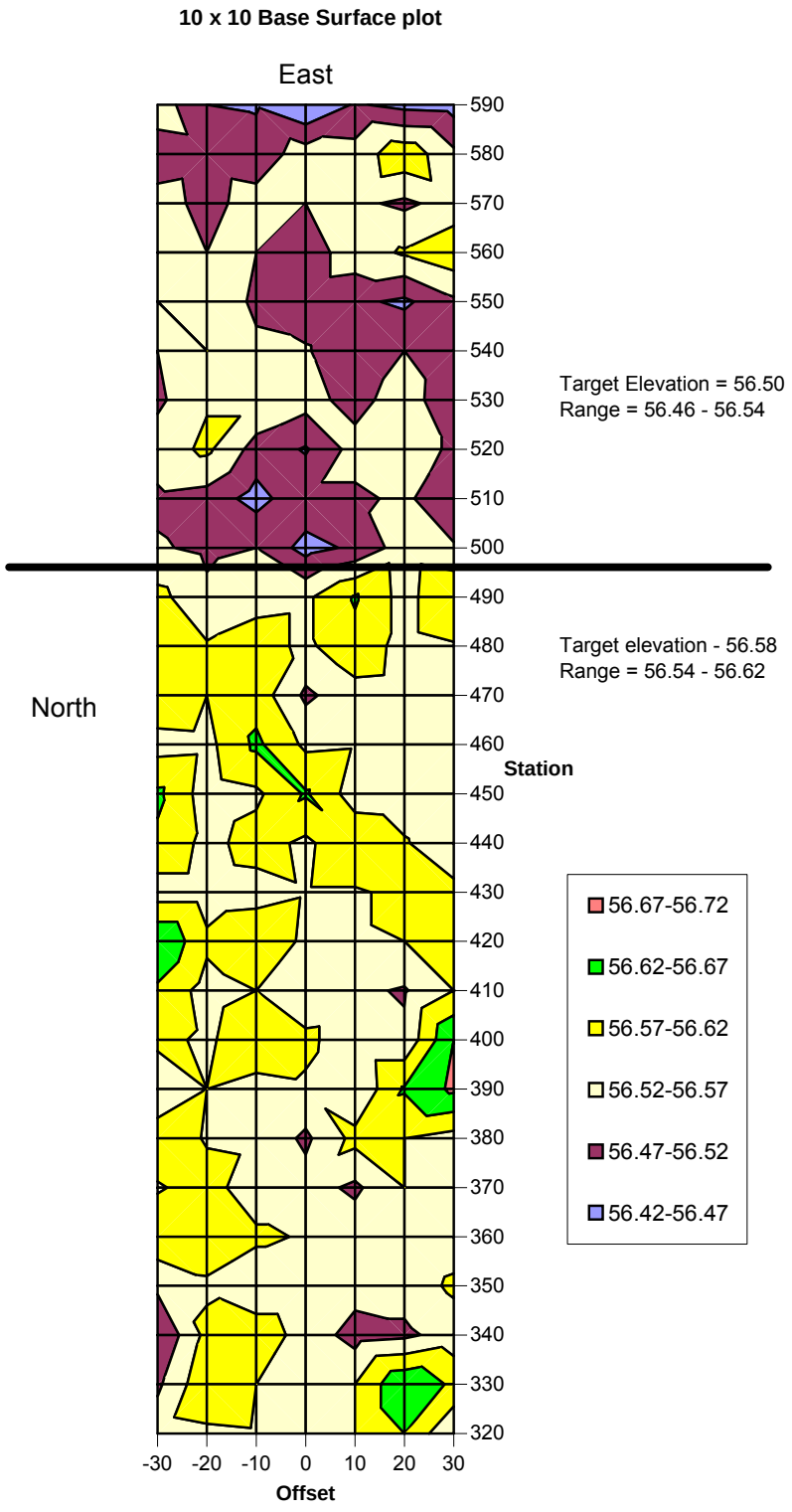

FIGURE 4. ELEVATION (FT) OF CC4 BASE (TARGET ELEVATION = 56.58 FT)

TABLE 7. THICKNESS OF BASE

Station	South			Offset			North
(ft)	30	20	10	0	-10	-20	-30
320	4.92	6.24	5.88	5.94	5.70	5.64	5.28
330	6.72	6.90	6.48	5.16	5.40	6.36	5.88
340	4.80	5.04	5.04	5.40	6.00	5.94	4.92
350	5.88	5.40	5.40	5.16	5.04	6.00	4.80
360	6.00	5.34	5.40	5.82	5.76	6.72	6.66
370	5.58	5.88	5.52	5.28	5.04	6.00	4.86
380	4.80	5.76	6.18	4.80	5.28	5.34	5.58
390	7.08	6.54	5.70	5.04	4.92	5.40	4.80
400	6.84	5.76	4.92	6.66	6.72	5.40	5.22
410	5.88	6.18	5.64	4.80	5.88	5.40	5.88
420	6.24	5.40	5.46	5.88	6.12	5.52	6.96
430	5.94	6.24	5.34	5.34	5.40	5.46	4.62
440	5.16	6.54	6.48	4.92	5.88	5.22	5.40
450	5.16	5.28	5.22	5.70	5.16	4.98	5.28
460	5.64	5.04	5.82	5.52	6.00	5.34	4.80
470	5.40	5.58	5.88	4.68	5.28	5.16	5.88
480	5.46	5.52	5.94	5.64	5.64	5.34	5.52
490	6.24	5.28	6.06	4.92	4.50	4.92	5.22
500	4.38	5.70	4.44	4.08	4.80	4.32	4.26
510	4.32	5.04	4.80	4.32	3.84	4.08	4.80
520	5.16	5.52	5.52	4.14	3.72	4.80	5.34
530	4.50	5.52	4.32	5.40	5.10	5.46	4.92
540	3.96	5.04	4.32	4.98	4.56	4.92	5.28
550	4.32	4.08	4.08	4.44	4.32	5.16	5.16
560	5.82	5.58	5.28	4.32	4.68	4.20	4.92
570	4.68	4.32	4.32	4.68	5.28	4.26	4.56
580	4.56	5.82	4.92	4.74	4.56	4.32	3.24

TABLE 8. CC4 BASE MOISTURE AND DENSITY TEST

Test	Sample Station	Density, %	Moisture, %
1	316	94.78	4.50
2	322	95.84	4.35
3	330	99.53	5.91
4	333	95.23	5.53
5	346	97.01	4.74
6	353	96.57	3.87
7	356	94.63	3.71
8	368	96.07	5.32
9	376	98.27	6.07
10	378	94.02	6.36
11	385	94.49	5.56
12	392	95.37	6.13
13	401	96.92	5.37
14	408	99.23	4.93
15	421	94.48	4.60
16	425	94.05	4.44
17	435	94.82	3.50
18	437	93.42	3.97
19	444	96.33	4.73
20	458	95.19	5.20
21	462	94.82	4.96
22	470	94.64	3.08
23	480	96.05	4.65
24	490	94.97	3.92
25	500	92.47	4.32
26	510	94.5	3.37
27	520	98.23	3.54
28	530	92.88	2.36
29	540	99.36	5.1
30	550	93.23	4.93
31	560	93.17	4.7
32	570	92.5	6.03
33	580	90.12	3.24
34	590	93.25	5.02
Final Density Avg, %		**94.86**	

One of the concerns of the FAA was that the segregation and moisture addition to the base course could adversely affect the moisture conditions of the subgrade. To address this, the base was excavated in seven areas and vane shear tests were taken at 1.5 inches, 3 inches, and 4.5 inches below the subgrade surface. These results showed that while the top 1.5 inches may have been adversely affected, tests at 3 and 4.5 inches remained in the condition provided by the FAA.

The FAA performed plate load tests at a number of locations on both the subgrade and base. Initially, it was planned to perform the plate load testing of both subgrade and aggregate base material at the same location. However, this could not be accomplished because it conflicted with instrument locations that were in place. One plate load test was conducted within each test item, on both north and south sides. While the plate load test results for both layers exhibited some variation, the average k value for both layers was determined to be the same, 143 psi/in. on the north side, and 146 psi/in. on the south side.

2.1.3 Underlying Slab Instrumentation.

Prior to the underlying slab construction beginning, all base and underlying slab instrumentation had to be installed. The instrumentation itself is discussed in section 2.2; this section discusses the construction aspects only. For the underlying slab, a total of 69 instruments were placed. These consisted of the following:

- 5 Soil Pressure Gages
- 20 Linear Position Transducers (LPTs)
- 40 Embedded Strain Gages
- 3 Thermistor Trees (each location had a top, middle, and bottom thermistor)
- 1 Moisture Tree (3 Moisture Gages)

In order for the soil pressure gages to produce consistent and long term results, they had a 90-degree bend 12 inches outside the plate for the oil reservoir that needed to be inserted down into the subgrade. For installation the base and subgrade were removed and the gage placed so that the top plate of the pressure cell was at the base surface. The plate of the gage itself was surrounded by a thin layer of sand in order to prevent angular points in the base aggregate from puncturing the cell plates. Figure 5 shows an installed soil pressure gage.

FIGURE 5. INSTALLED SOIL PRESSURE GAGE

With respect to the LPT and embedded strain gages, the difficult part of the instrumentation construction plan dealt with how to place these instruments at their desired locations, while still allowing paving in a production manner. The final solution was to survey all instruments into their final x-y locations, placing them on rebar chairs to hold them at the correct elevations, and then protect them with PVC "cans" during concrete placement. For the LPTs and bottom embedded strain gages, the rebar chairs were adjusted so that the instruments were at the correct location prior to placement. The top strain gages were placed in the correct location during construction.

In order to keep the instrumentation wiring out of the underlying slabs, trenches were dug in the base course and wires placed within them. Prior to placement of the underling slab, these trenches were backfilled with concrete sand and compacted using hand tampers.

During the slab construction, the instrumentation cans were carefully hand filled with concrete completely encasing the instruments. Next, concrete was piled around the cans to hold them in place as the Bidwell finishing machine went over the instrumentation. After the finishing machine had passed, the cans were carefully pulled out of the concrete, the top embedded strain gages placed, and the surface repaired and finished (figure 6).

2.1.4 Underlying Slab Construction.

The initial proposal called for the construction of approximately three concrete slabs per day using forms and a vibrating screed or tube roller. However, during the development of the roadmap, QES decided to place the concrete slabs at the sixty-foot width using a Bidwell pavement finishing machine that would ride on the rails used by the loading machine. The three primary benefits of doing this are:

- Improved thickness control in the test items,
- Improved material uniformity in the test items, and
- Expedited construction.

The construction team was a combination of QES and Trumbull Corporation personnel. Structural section 1 (test items N1 and S1) was designed to have a 6-inch slab thickness, structural section 2 (test items N2 and S2) a 7.5-inch slab thickness, and structural section 3 (test items N3 and S3) a 10-inch slab thickness. All underlay slabs were non-reinforced slabs with no dowels.

LPT instrument

Embedded strain gages

Instrument cans in place

Placing concrete into cans

Instrument cans piled with concrete

Pulling instrument can

FIGURE 6. LPT AND STRAIN GAGE INSTRUMENTATION PLACEMENT

2.1.4.1 Underlying Slab Construction Set-up.

The set-up work for the underlying slab construction started on February 20, 2006. The primary set up activities consisted of placing side forms; assembling and adjusting the Bidwell finishing machine; assembling the construction bridge from which the finishing would be completed and the cans pulled; setting the stringline for elevation guidance; and performing a "dry run."

A single 17-inch side form was used along the north and south rails so that the same forms could be used to place both the underlying slabs and overlay slabs. These side forms were placed at a top surface elevation of 58.00 (1-inch above the final grade for the overlay (El = 57.92 ft.). In addition to staking the forms into the base and subgrade, the forms were braced against the concrete side walls of the test machine tracks (figure 7).

FIGURE 7. PLACING SIDE FORMS

In order to be able to place instrumentation wires for the overlay, conduit had to be placed under the forms so that wire could be run under the form to be installed into the NAPTF data loggers. Similarly, for the surface gages, PVC pipes were placed in the transitions so that surface strain gage wires on the north side could be run under the pavement to the south side and the NAPTF data loggers. Conduits are shown in figure 8.

FIGURE 8. CONDUIT SET-UP FOR INSTRUMENTATION WIRES

The paver used for this project was a Bidwell 5000 Form Riding Concrete Paving machine (figure 9). This machine has a paving carriage that strikes off the concrete and textures it with augers, paving rollers, drag pan and texturing. It has an automatic internal concrete vibration system to consolidate the concrete. Grade control is accomplished using a stringline sensing system. For this project, the machine was expanded so that the full 60 ft width of the test area could be placed in a single pass. Surface elevation control was also improved by the fact that the Bidwell machine rode on the rails installed for the test vehicle.

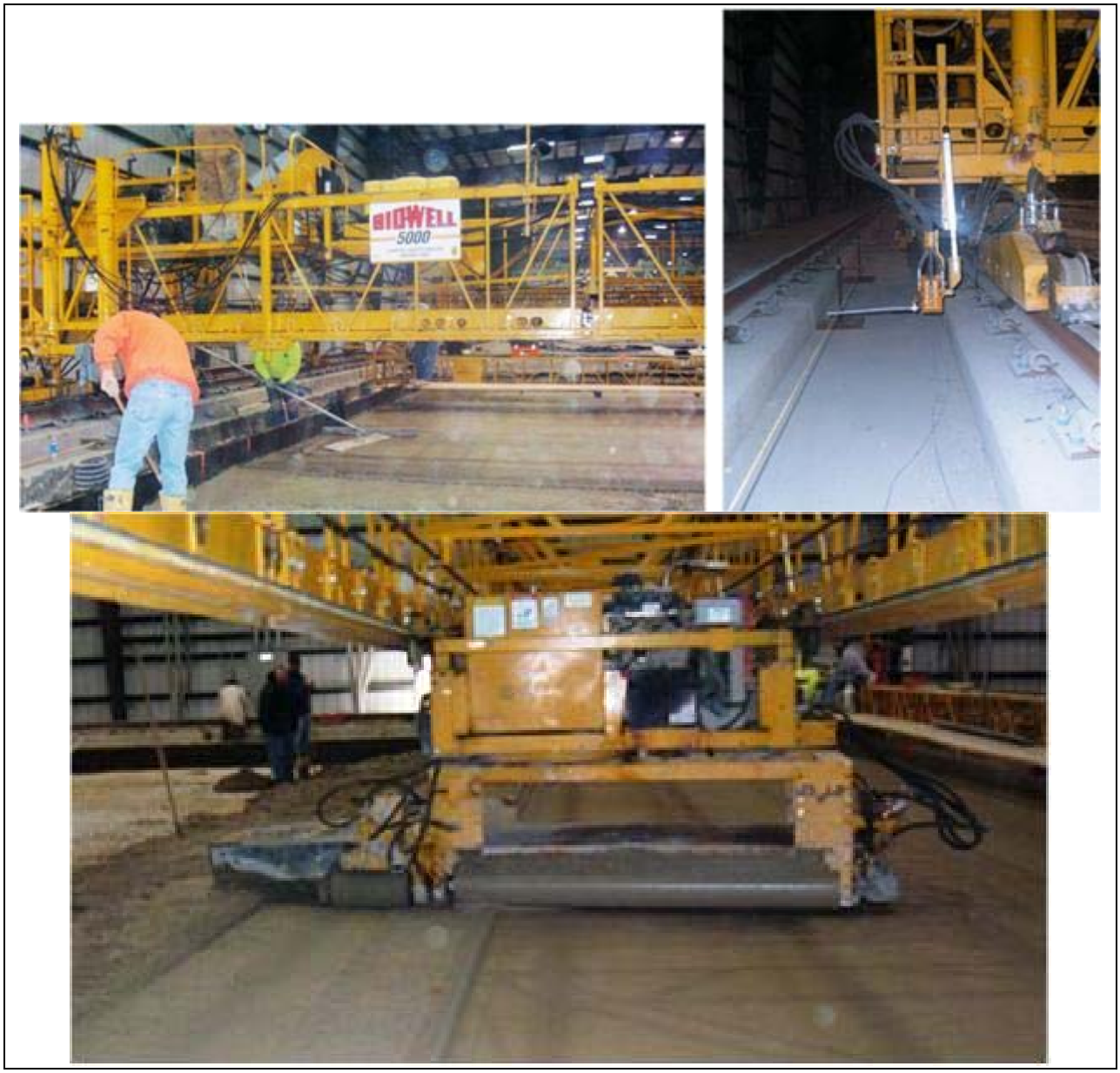

FIGURE 9. BIDWELL 5000 FORM RIDING CONCRETE PAVING MACHINE

In addition to the concrete paver spanning the entire distance over the pavement, a work bridge was also used so that the pavement could be finished, cure could be placed, and instrumentation cans could be pulled. No texture was applied to the underlying slab. Instead, it was left smooth so that the surface could be examined more easily after the overlay and interlayer would be removed at the end of the experiment.

The dry run was used to verify that the machine was operating correctly, meeting grade, and was able to clear all the instrumentation cans. The cans were designed so that their top surface was 0.5 inches below the concrete finished surface. Once the setup was complete, the base course was covered with plastic to maintain the moisture conditions until paving took place.

2.1.4.2 Concrete Mix.

Based on past NAPTF experience with concrete mixes, QES decided to use the same concrete mix as used in the Construction Cycle 2 experiment (table 9). This mix was specifically designed to control flexural strength so that it would not become abnormally high. Mixes previously used at the NAPTF containing standard FAA material proportions were found to obtain flexural strengths well above 900 psi, giving rise to the concern that the concrete at the test center would not represent standard mixes used at airports throughout the United States. The target strength for the mix was 750 psi flexural strength.

TABLE 9. CONCRETE MIX PROPORTIONS

Material	Proportions
#57 Coarse Aggregate (Millington)	1,685 lbs/cy
NJ Sand	1,555 lbs/cy
Type 1 Cement	250 lbs/cy
Class C Flyash	250 lbs/cy
Water	250 lbs/cy
Water/Cementitious Ratio	0.50

In order to track strength gain in the mix, QES developed maturity curves for the concrete mix. This was done to help control timing for joint sawing, since paving would take place during the winter months and there was uncertainty about how long it would take the concrete to set. Figure 10 and figure 11 show both flexural and compressive strength maturity curves that were developed and used on the project. More information on maturity is available in the IPRF Report *Using Maturity Testing for Airfield Concrete Pavement Construction and Repair* (2006).

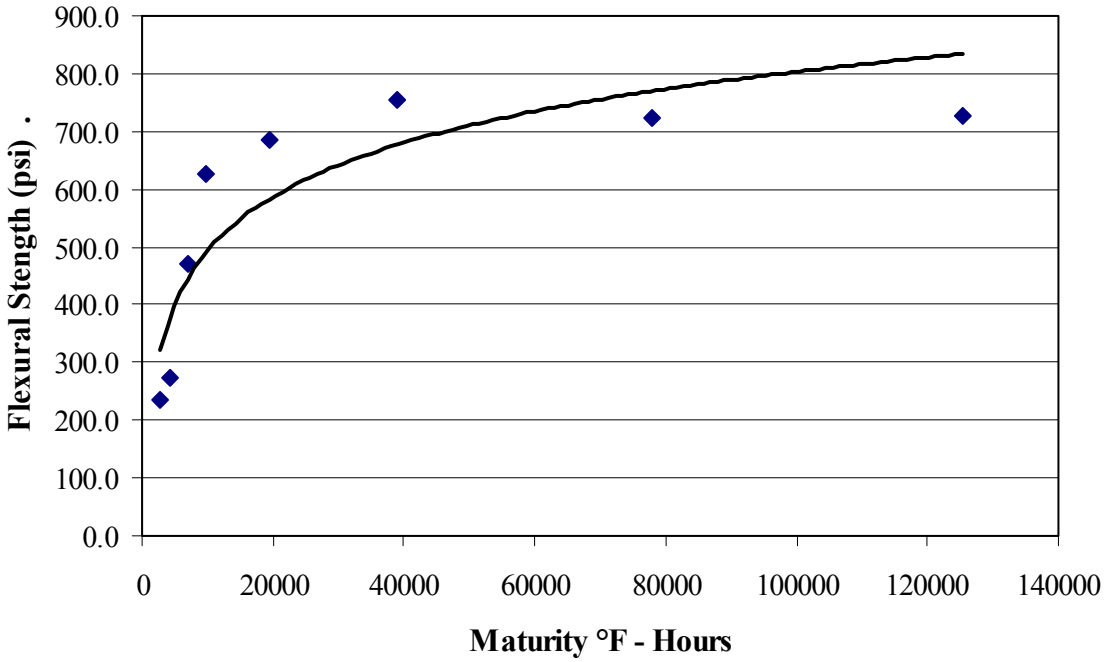

FIGURE 10. FLEXURAL MATURITY CURVE FOR CC4 BASELINE EXPERIMENT CONCRETE MIX

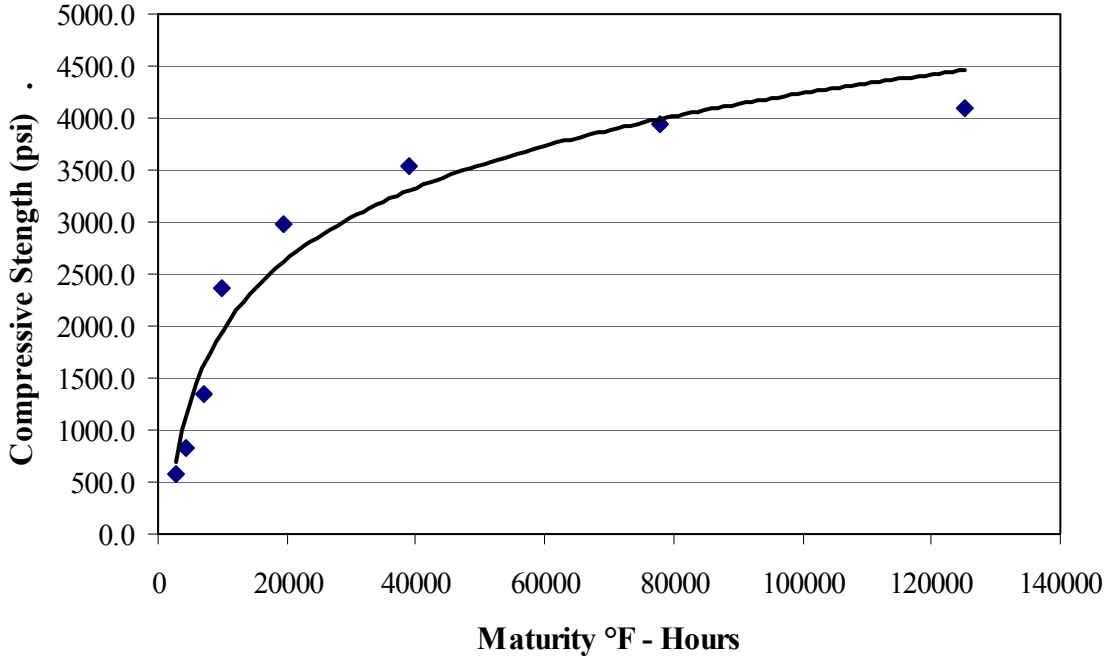

FIGURE 11. COMPRESSIVE MATURITY CURVE FOR CC4 BASELINE EXPERIMENT CONCRETE

2.1.4.3 Concrete Paving of the Underlying Slabs.

Concrete paving occurred on Monday, February 27 and Tuesday, February 28. The average outside temperature for Monday was 23.7°F and 30.2°F for Tuesday. The concrete producer was Clayton Concrete, which was delivering the material from the plant approximately two miles away from the project site. Since the concrete trucks could not travel on the aggregate base without damaging it, concrete was delivered to the paver using a Putzmeister 36M pump truck.

Paving began on the west end of the project (station 300) and proceeded east. For each day of paving, the pump truck set up on the east end of the project (station 625). For Monday's paving, the pump truck's boom could only reach 125 feet into the structural section (to station 500) and as such, a slick line had to be attached to the end of the pump to get the concrete the remaining distance to the paver, as shown in figure 12.

To place the concrete, the slick line was moved across the pavement, from the north side to the south side, placing between an 8 to 10 foot wide swath of concrete at the approximate pavement thickness (swath width depended on thickness). Once the slick line reached the south side, a section of the slick line was removed, the hose backed up and reattached, and then concrete placement continued to the north side where the process repeated itself.

Pump truck

Placing concrete

Breaking slick line apart

FIGURE 12. PLACING CONCRETE FROM SLICK LINE

Monday's paving started at 8:30 am with the arrival of the first truck. Concrete was delivered on a regular basis in about 15 to 20 minute increments. Paving continued throughout the day until approximately 3:15 pm. Paving was completed from station 300 to station 500. Tuesday's paving continued in the same manner, with the first truck arriving at 8:30 am. Paving continued until approximately 2:00 pm. Paving started at station 500 and continued to station 600. For the two days of paving, a total of 461 cubic yards of concrete was placed (264 cubic yards on Monday and 197 cubic yards on Tuesday). Paving without a slick line is shown in figure 13.

FIGURE 13. PLACING CONCRETE WITHOUT A SLICK LINE

At the end of each day's paving, a layer of polyethylene sheets, a layer of insulated blankets, and then a second layer of polyethylene sheets were placed over the concrete, as shown in figure 14, in order to keep the concrete as warm as possible.

FIGURE 14. PLACEMENT OF POLYETHYLENE SHEETS AND BLANKETS

2.1.4.4 Concrete Quality Control Testing.

On-site quality control testing consisted of concrete temperature, slump, air content and unit weight. For Monday's paving, the first three trucks showed high air content, however, this was corrected by the fourth truck. For structural section 1, the temperature ranged from 59 to 61°F (average of 60), the slump ranged from 3.0 to 7.0 inches (average of 4.8), air content ranged from 5.8 to 8 percent (average of 6.4), and the unit weights varied from 148.6 to 152.4 pounds per cubic foot (average of 150.8). Reported values for structural section 2 showed the temperature ranged from 62 to 64°F (average of 63.7), the slump ranged from 0.8 to 3.8 inches (average of 2.4), air content was consistently 4.2 percent and the unit weights varied from 155.0 to 155.5 pounds per cubic foot (average of 155.2). Structural section 3 had similar values with the temperature ranging from 60 to 67°F (average of 62.8), the slump ranging from 2.3 to 7.5 inches (average of 4.8), air content ranging from 2.3 to 4.8 percent (average of 3.7) and the unit weights varying from 152.8 to 156.9 pounds per cubic foot (average of 154.7).

In addition to the above tests, concrete maturity probes were inserted into each structural section to help monitor the concrete temperature. A single probe was inserted into structural sections 1 and 2, while structural section 3 received two probes; one at each end. Figure 15 and figure 16 show concrete temperatures and maturity for each structural section's placement for the initial 72 hours.

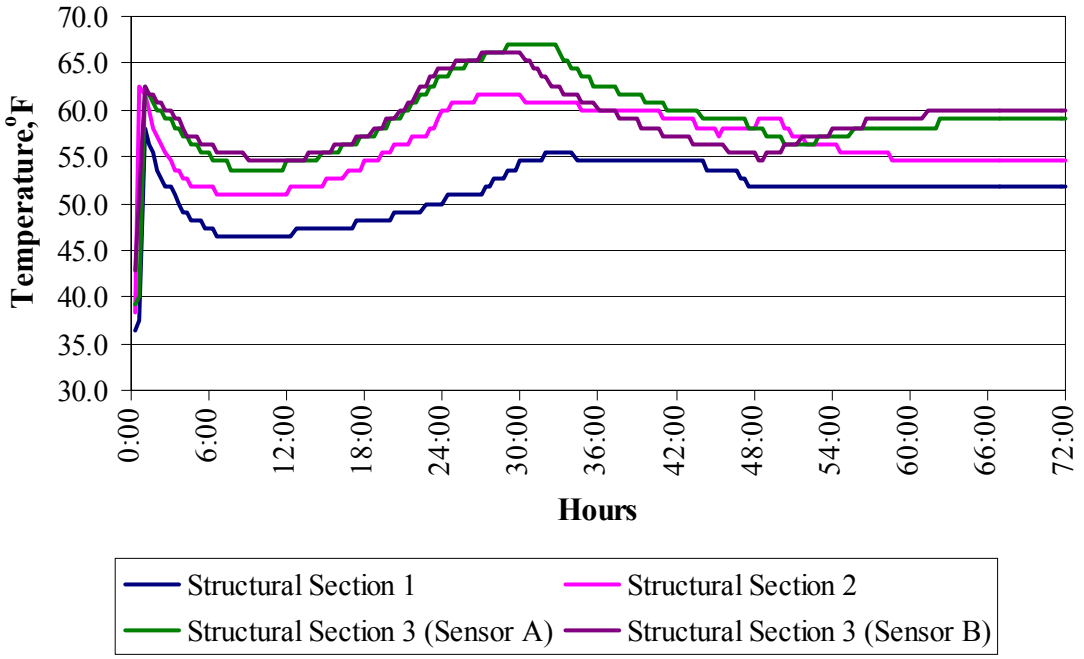

FIGURE 15. CONCRETE TEMPERATURES FOR EACH STRUCTURAL SECTION (FIRST 72 HOURS)

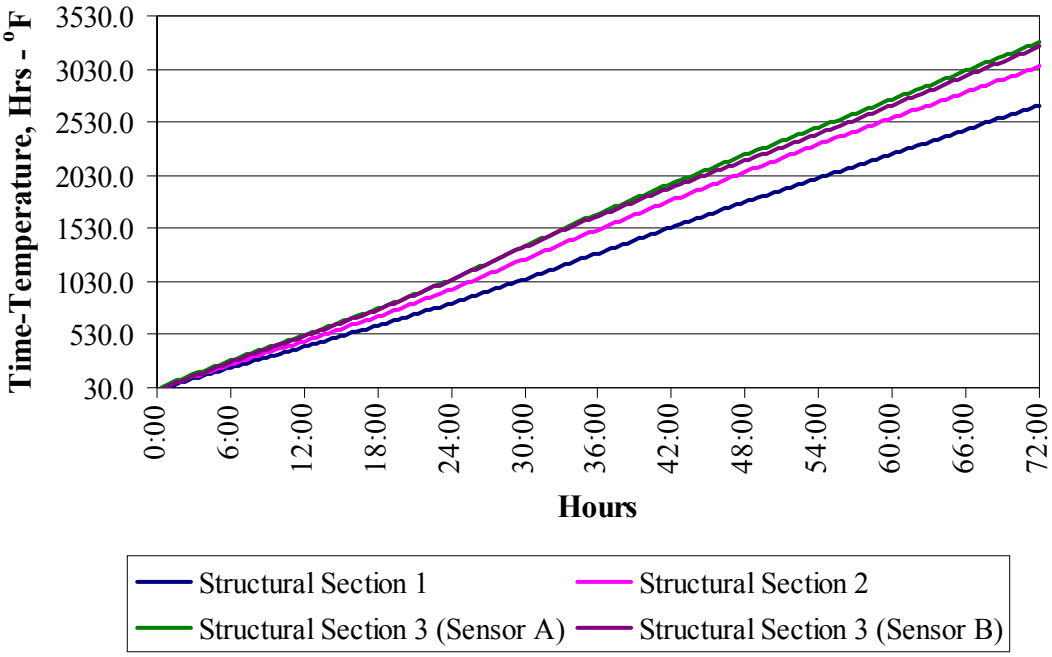

FIGURE 16. CONCRETE MATURITY FOR EACH STRUCTURAL SECTION (FIRST 72 HOURS)

2.1.4.5 Joint Sawing.

One of the key aspects to having the maturity data available on site was that QES could estimate the approximate time that the joints could be sawn. Several reports have found that the optimum compressive strength for joint sawing is between 300 and 1000 psi. For this project, it was decided to target a strength of 500 psi at the time of sawing. Using the compressive strength maturity data, it was determined that the concrete would gain this strength at a maturity of approximately 1200 to 1500°F–hrs. Therefore, it was determined that sawing could begin approximately 30 hours after placement for all three structural sections.

Joint sawing started on February 28 with sawing in test items N1, S1, N2 and S2, and was completed on March 1 in test items N3 and S3. The process consisted of removing the polyethylene sheeting and covers, surveying the joint locations, marking the joints with string and paint, and then sawing the joints. All joints, except those at Transitions 5 and 6 were sawn at D/2. The joints at stations 390, 410, 485 and 500 were sawn as deep as the saws would go, (approximately 7 inches), in an attempt to isolate the transitions from the test items.

The as-constructed joint layout is shown in appendix A. In test items N3 and S3, the original plans for construction had been designed as an 8.5-foot slab at the third slab (between joints at stations 525 to 533.5). However, the third slab was inadvertently laid out for a 12.5 ft slab and the fourth slab became the 8.5 ft slab (between joints at stations 537.5 and 546) on the construction drawing.

In an effort to minimize the adhesion between the asphalt layer and the underlying slab, the saw slurry was left on the surface. During the construction of the AC interlayer, it was noted that, as planned, the AC layer did not bond to the underlying slab.

2.1.4.6 Curing.

Because the underlying pavement was being constructed in the winter, there was concern with maintaining both the moisture and temperature condition of the underlying pavement. With respect to the moisture during construction, workers applied a layer of clear coat cure compound from the work bridge. At the end of the each day, the pavement was covered with polyethylene and blankets to maintain moisture, as well as heat in the slab.

Finally, as mentioned above, instead of vacuuming the slurry up from the sawing operations, it was left on the surface in order to minimize the adhesion between the concrete and asphalt interlayer. This benefited the curing process, in that the pavement was essentially wet cured as the slurry under the polyethylene held in the water and did not start to dry until after the cover and polyethylene sheets were removed on March 9 and 10, 2006.

With respect to maintaining the temperature in the slab, the pavement was covered, as mentioned earlier, but it was also heated using a ground heating system. The system consisted of a fuel oil burner mounted on a trailer, with a pair of continuous loop hoses filled with a heat exchange fluid. Heat is transferred from the burner to the slab through these hoses. The heater hoses applied additional heat to the top of the slab, under the insulation covers to help as a catalyst for the internal hydration process needed within the concrete at the relatively low ambient temperatures. Table 10 shows the thicknesses as measured on the 10' by 10' grid.

2.1.5 Asphalt Interlayer Construction.

A one-inch asphalt interlayer was planned for this work, based on prior experience with unbonded overlays. The asphalt interlayer was placed and compacted using conventional asphalt paving techniques on March 22, 2006. Lindy Paving performed the actual placement using a CAT paver and compaction using the same 10-ton roller as was used on the aggregate base course. Wooden blockouts were used to create top slab instrumentation wire channels in the asphalt, which did cause some issues with construction. The asphalt mix used during this effort was the same as was being produced for NJDOT I-5. At the time of placement, the concrete pavement surface was about 45°F. As a result of problems with the screed catching on the blockouts, and the cool substrata, the asphalt mat density achieved in the interlayer varied from the middle 80^{th} percentile to the low 90^{th} percentile range of maximum theoretical density. Although the nominal thickness was one inch, some variation was observed, particularly at startup where the lift was as thick as two inches in the transition.

The thickness and density variations can largely be attributed to the difficulty caused by the blockouts, as the boards used to form the instrument wire channels were being dislodged by the paver. Additional nails were added, but ultimately it appeared the screed was adjusted slightly higher, and the problem ceased.

TABLE 10. THICKNESS OF UNDERLAY SLAB

Station	South			Offset			North
(ft)	30	20	10	0	-10	-20	-30
320	7.32	5.88	6.24	6.30	6.30	6.48	6.72
330	6.12	5.10	6.00	6.60	6.00	5.64	7.08
340	6.84	6.96	6.84	6.24	5.76	6.06	7.68
350	6.24	6.60	6.36	6.60	6.60	6.48	6.96
360	6.60	6.66	6.12	6.06	5.76	5.52	6.06
370	6.66	6.24	6.84	6.48	6.48	5.88	6.66
380	6.84	6.24	5.70	6.72	6.12	6.18	5.82
390	5.16	5.34	6.66	6.24	6.24	6.12	7.08
400	5.52	6.72	6.48	5.82	5.40	6.36	6.30
410	6.72	7.02	6.96	7.08	6.48	6.84	6.48
420	7.32	7.44	7.50	7.56	6.84	7.32	6.60
430	7.98	7.68	7.74	7.74	7.92	7.98	8.58
440	8.28	7.62	7.20	7.80	7.56	7.86	7.68
450	8.40	8.16	8.10	7.02	7.56	7.86	6.96
460	7.80	8.16	7.62	7.68	6.96	7.86	8.04
470	7.80	7.74	7.56	7.56	6.72	7.32	7.20
480	7.74	7.92	7.14	7.56	7.20	7.62	7.56
490	7.20	7.68	6.66	7.56	7.62	7.92	7.50
500	8.46	8.22	9.00	9.36	8.28	8.40	8.82
510	9.96	9.36	9.60	9.60	10.32	9.96	9.72
520	9.84	9.36	9.60	10.38	10.08	9.24	9.78
530	10.62	9.48	10.08	9.48	9.30	9.42	10.32
540	10.32	9.96	10.32	9.66	9.72	9.24	10.08
550	10.08	10.80	10.56	10.20	10.20	9.48	9.84
560	9.06	9.66	9.96	10.56	10.32	10.32	10.20
570	10.08	10.56	10.32	10.32	10.08	10.62	10.44
580	10.44	9.42	10.20	10.14	10.92	10.80	11.04

Subsequently, the NAPTF loading machine was used to apply a 15,000 pound load on one dual tire configuration. Loading was applied to the pavement centerline as a test to assure the asphalt would not sustain major damage. None was observed. Then the test load was applied to the instrument line along the wheel path on the north side, to capture instrument response. This was used to assess the effect of adding the asphalt to the concrete, which was previously checked for response to 15,000 pound load. Table 11 shows the thicknesses as measured on the 10'x10' grid.

TABLE 11. THICKNESS OF ASPHALT INTERLAYER

Station	South			Offset			North
(ft)	30	20	10	0	-10	-20	-30
320	2.04	1.44	1.44	0.84	0.48	1.32	1.20
330	1.32	1.68	1.68	1.20	1.32	0.96	1.68
340	0.72	0.96	1.44	1.08	1.08	1.08	1.44
350	1.20	0.84	1.44	0.96	0.96	1.08	1.80
360	1.44	1.20	1.68	1.08	1.56	1.56	1.80
370	0.96	1.08	1.20	0.96	0.96	1.20	0.96
380	1.08	1.08	1.44	0.72	0.72	1.44	0.96
390	1.32	1.32	1.20	0.72	0.72	1.20	0.96
400	1.44	1.44	1.68	1.32	1.56	1.44	1.44
410	2.16	2.16	2.04	1.80	1.80	1.80	1.56
420	1.32	1.44	1.44	1.32	1.32	1.44	1.80
430	0.72	0.96	1.08	0.84	0.96	0.96	0.60
440	0.96	0.96	0.96	0.60	0.48	0.96	0.72
450	1.68	0.96	0.84	0.60	0.96	1.20	1.20
460	1.56	0.96	1.08	0.72	0.72	1.20	1.08
470	1.32	1.44	1.44	1.44	1.44	1.44	1.20
480	1.80	1.20	1.20	0.96	1.08	0.96	0.60
490	1.92	1.68	1.80	1.44	1.44	1.44	1.08
500	2.16	2.04	1.92	1.68	1.80	1.92	1.68
510	1.92	1.56	1.80	1.20	1.20	0.96	1.56
520	1.56	1.20	1.20	0.96	0.84	0.72	0.60
530	1.44	1.08	1.32	0.96	0.84	0.84	0.48
540	2.04	1.32	1.80	1.56	1.08	1.56	1.20
550	0.96	0.84	1.32	1.32	1.20	1.32	0.84
560	0.48	0.60	0.96	0.84	0.96	1.20	1.08
570	0.36	0.48	0.84	0.60	0.60	0.60	0.60
580	0.12	0.48	0.60	0.48	0.12	0.36	0.24

2.1.6 Concrete Overlay Slab Construction.

The concrete overlay was placed on March 29, 2007 using materials and procedures similar to the underlying slab construction. The major difference was the addition of dowel bars in both the longitudinal and transverse directions. The dowel bars were one-inch diameter bars placed on 12-inch centers. Although three different overlay thicknesses were placed, the design of the experiment resulted in the final surface being at a constant elevation for all three structural sections as previously indicated.

2.1.6.1 Overlay Slab Construction Set-up.

The same forms and rails as used for the underlying pavement slabs were used for the overlay construction. Also, similar instrumentation was placed in the overlay slabs, and the installation methods for these instruments were the same as previously discussed. Wiring for the overlay slab instruments were placed in the blockouts in the asphalt interlayer. These blockouts were then backfilled with cold patch material and compacted prior to placement of the concrete.

One-inch diameter by 18-inch long dowel bars were installed, using dowel baskets aligned and installed (nailed to the asphalt layer) prior to placement of the concrete. For the longitudinal joints, the baskets were set such that the bar spacing was a consistent 12 inches center-to-center. For the transverse joints, the baskets were set such that the bars had a center-to-center spacing of 12 inches, with one bar being skipped at each longitudinal joint. Structural section 1 (test items N1 and S1) received a 9-inch overlay and the dowel bars were placed with the center of the bars five inches above the asphalt. Structural section 2 (test items N2 and S2) received a 7.5-inch overlay, and the centers of the bars were four inches above the asphalt. The structural section (test items N3 and S3) included a 6-inch overlay, and the centers of the dowel bars were four inches above the asphalt.

2.1.6.2 Concrete Mix.

The overlay mix design was identical to that of the underlying slabs as provided in appendix A. The target mix strength was 750 psi in flexure, but the mix actually achieved a flexural strength of only approximately 500 psi.

2.1.6.3 Concrete Paving of the Overlay Slab.

Placement of the overlay slabs followed the same basic process as the underlying slabs. Concrete paving took place on March 29, 2006 with an average outside temperature of 48°F Clayton Concrete provided this mix from their plant located two miles from the project site. Once again, concrete was delivered to the paver using a Putzmeister 36M pump truck, although since the pump truck could traverse the asphalt layer without causing damage, no slick line was required for the overlay placement.

The final surface finish was a light broom texture in the transverse direction. The instrumentation cans were pulled, the surface gages placed and the surface repaired. This was followed by an application of a liquid based curing compound applied at an approximate rate of 0.015 gallons per square yard. The curing compound was applied by hand sprayer from the work bridge. Upon completion of the paving, a layer of polyethylene sheets, a layer of insulated blankets, and then a second layer of polyethylene sheets was placed over the concrete in order to keep the concrete as warm as possible. Table 12 shows the thicknesses as measured on the 10’x10’ grid.

TABLE 12. THICKNESS OF OVERLAY SLAB

Station (ft)	South 30	20	10	Offset 0	-10	-20	North -30
320	7.56	8.16	8.40	8.76	9.12	8.04	7.92
330	8.52	8.28	8.40	8.76	8.64	8.88	7.68
340	9.12	8.88	8.64	8.88	8.88	8.76	8.16
350	8.64	8.76	8.40	8.52	8.52	8.28	7.56
360	8.88	9.00	8.64	9.00	8.76	8.64	7.92
370	9.00	8.88	8.88	9.00	9.00	8.88	8.52
380	8.88	9.12	8.76	9.36	9.36	8.64	8.88
390	8.76	9.00	8.88	9.24	9.36	8.88	8.64
400	8.40	8.64	8.52	8.88	8.76	8.52	8.28
410	7.56	7.80	7.80	7.92	7.92	7.80	7.80
420	7.32	7.44	7.44	7.44	7.68	7.44	6.96
430	7.56	7.56	7.44	7.68	7.56	7.68	7.56
440	7.56	7.68	7.56	7.80	7.80	7.56	7.44
450	6.72	7.32	7.44	7.68	7.68	7.32	7.32
460	6.72	7.32	7.32	7.56	7.44	6.96	7.08
470	7.20	7.08	7.20	7.56	7.32	7.20	7.20
480	6.72	7.20	7.20	7.44	7.32	7.20	7.08
490	6.24	6.84	6.72	6.84	6.84	6.84	7.08
500	6.12	6.24	6.00	6.12	6.12	6.00	5.76
510	5.52	5.76	5.40	5.88	5.88	5.88	5.64
520	5.52	6.00	5.76	6.00	6.00	5.88	5.88
530	5.40	5.88	5.52	5.88	5.88	5.64	5.88
540	5.04	5.52	5.04	5.28	5.64	5.16	5.40
550	5.76	5.64	5.16	5.28	5.28	5.40	5.52
560	6.48	6.12	5.64	5.76	5.40	5.16	5.28
570	6.36	5.76	5.40	5.52	5.52	5.40	5.40
580	6.36	5.88	5.76	5.64	5.76	5.52	5.52

2.1.6.4 Concrete Quality Control Testing.

On-site quality control (QC) testing consisted of concrete temperature, slump, air content and unit weight. QC test results from the placement of both top and bottom slabs are summarized in table 13.

TABLE 13. BOTTOM CONCRETE SLAB QC DATA SUMMARY

Bottom Slab				
Test Item	**Temp (degrees F)**	**Slump (inches)**	**Entrained Air (percent)**	**Unit Weight (pounds/cubic foot)**
1	61-59	7.0-3.0	8-5.8	152.428-148.588
2	64-62	3.75-0.75	4.2-4.2	155.517-154.974
3	67-60	7.5-2.75	4.8-2.3	156.936-152.845
Average	62.2	4	4.8	153.6
Top Slab				
1	72	3.52	3.4	157.03
2	73	3.63	4.5	154.89
3	73	3.79	4.3	152.89
Average	72	3.71	4.0	155.63

The QC results indicate that while there was some variation between the top and bottom slab placements, particularly in mix temperature, overall the concrete provided for the experiment was consistent.

Results from strength testing were also fairly consistent, even though the strength achieved was not that expected. Flexural test results are summarized in table 14.

TABLE 14. SUMMARY OF 90-DAY CONCRETE FLEXURAL STRENGTH FOR BASELINE EXPERIMENT

Sample	**Placement**		
QES (field cured)		**Flexural Strength, psi**	
	Bottom Slab	503	
	Top Slab	560	

A subsequent assessment of the factors which may have changed since the Construction Cycle 2 concrete material testing, and the placement of the Construction Cycle 4 experiment concluded that the probable cause for the relatively low strength, using the same mix design and producer, was variation in the fly ash component.

2.1.6.5 Joint Layout and Sawing.

Joint patterns were established to create matched and mismatched joints in the underlying slab and the concrete overlay, as a part of the experimental matrix. Joints in the bottom slabs were sawn to approximately D/2 (one-half slab thickness) for specific test item thickness. Joints in the overlaying pavement were cut using early entry sawcut technology. In both cases, joints were laid out and sawn using typical joint sawing techniques. Concrete maturity data, as shown in figure 16 was used to monitor the strength gain of the slabs, and to assure that joints were cut

before too much strength was obtained. The window identified for sawcutting was the range of 500-1,000 psi. This was successfully achieved using the maturity curve (figure 10) as a guide.

2.1.6.6 Curing.

Since the temperatures inside the NAPTF facility were staying in the range of 40 to 45°F during the construction period, it was decided to wet cure the concrete overlay slabs for a minimum of 28 days. The cure cover actually remained in place for five weeks before being removed. Prior to that, concrete strength test results were obtained from test specimens cast during the placement. Maturity data was also used to monitor the strength gain of the concrete.

During the cure period, ground heater equipment was used to increase the concrete temperature, to assure that significant hydration took place. The ground heater hoses were placed under the curing blankets, but on the plastic moisture barrier.

During the first two days following placement, experimentation with ground heater operation and effects on concrete temperature was conducted. Ultimately, it was decided the most efficient benefit to be gained was to set the heater unit at around 95°F. The heater was left in place for four weeks, and then removed. The temperature data collected from the maturity sensors in the slabs showed that the effect of the heaters was to increase slab temperature to 55 to 65°F, with the thick structural section having the highest temperatures.

2.1.7 Pavement Marking.

A painting plan was developed as a guide for work to be carried out during testing. The plan included slab identification, underlying slab joint locations, safety zones, and heavyweight falling deflectometer test locations.

Individual slab identification numbers consistent with the slab numbering plan were painted at slab corners. Blue lines were painted on the pavement surface to help delineate the location of joints sawn in the underlying slab. Solid yellow lines were located 5 feet from the north and south slab edges, for safety. A dashed yellow line represented the longitudinal center line of the experimental pavement area. Solid circles with a crossed “tail” attached indicated the location and direction of deflection testing.

2.2 INSTRUMENTATION.

2.2.1 Selection of Gages.

The selection of gages was based on reliability, accuracy, price, and ease of handling at the construction site. Gage manufacturer and model information are summarized in table 15. The instrumentation layout for top and bottom slabs is provided in appendix B. Details of the number of gages installed are summarized in table 16.

TABLE 15. GAGE MODEL

Gage	Manufacturer	Model
Soil Pressure	Geokon	
Surface Strain	Texas Measurement	PL-120-11
Embedded Strain	Texas Measurement	KM-100B
Dowel Bar Strain	Texas Measurement	FLA-6-11
LPT	Honeywell	MLT001N 1500 F5C
Thermistor	Omega	44005

TABLE 16. NUMBER OF GAGES

Gage	Layer	Test Item						Total	Remarks
		N1	S1	N2	S2	N3	S3		
Soil Pressure Cell	Subgrade	2	0	0	0	2	1	5	Corner of the slab
LPT	Underlay	3	3	4	4	3	3	20	Corner of slab
	Overlay	14	6	17	8	14	6	65	Corner and center of slab
Embedded Strain Gage (temperature-integrated)	Underlay	6	6	8	8	6	6	40	Two per location
	Overlay	6	6	6	6	6	6	36	Two per location
Surface Strain Gage	Overlay	9	9	9	9	9	9	54	
Strain Gage	Dowel Bar	8	0	4	0	8	0	20	Two per dowel bar
Thermistor	Underlay	0	3	0	3	0	3	9	Three per tree
	Overlay	0	3	0	3	0	3	9	Three per tree
Thermocouple	Subgrade		1		1		1		
	Underlay	0	2	0	0	0	3	5	On top of bond breaker
Soil Moisture Sensor	Subgrade	1	1	1	1			4	Under the center of the slab

The gear loads are applied to the pavement in a wander pattern around the longitudinal joint between the two full slabs. Therefore, to collect the greatest response of the slab under load, most of the gages are located along the *loaded longitudinal joint*. Two slabs were selected per test item per lane for instrumentation.

2.2.2 Mechanical Response Data.

2.2.2.1 Soil Pressure.

Vertical pressure on subgrade was monitored by a soil pressure cell. Cells were installed near the top of the subbase to measure pressure induced by the underlay slab during the loading test.

All cells were under the wheel track at the corner of a slab. Five pressure cells were installed, two in test item north 1 (N1), two in test item north 3 (N3), and one in test item south 3 (S3).

2.2.2.2 Vertical Movement of the Slab.

Vertical movement of the slab was monitored by LPTs. To install LPTs for the underlay slabs, a steel bar was driven into the subgrade to serve as a stationary reference point. Each LPT was attached to the steel bar, and a rebar chair was used to secure the height of the LPT at its mid-position as the slab was constructed to make sure that both up and down movement from the as-built position could be recorded. Installation of LPTs for the overlay slab was by the same procedure, except that a hole was cored through the underlay slab and the anchor was driven through the hole into subgrade. The hole in the underlying slab was sealed with expansive foam to prevent intrusion from the concrete placed as the overlay. The rest of the installation procedure was the same.

Three LPTs were installed along the loaded longitudinal joint at the corner of two selected underlay slabs. The movement of two underlay slabs per test item per lane was monitored.

The movements of the overlay slabs were monitored more elaborately. The two selected slabs were fully instrumented; LPTs were installed at all four corners and the center of the slab to monitor movement throughout the entire slab. Since readings of the LPT represent the position of the slab relative to the zero reference, the pre-load position was the position of the slab under the environmental conditions at the time of installation.

2.2.2.3 Strain.

A pair of embedded strain gages was installed at each location to measure strain near the top and bottom of the slab in the longitudinal direction. These gages were usually located at the mid slab (transverse center of the slab) of the loaded joint. Embedded strain gages were installed during the paving operation, as previously described. Rebar chairs were used to make certain the top gages were set at the proper height, one inch below the top surface. A spacer was used to make sure that the bottom gage was completely covered by concrete and any part of the gage could not rub against the surface of the substrate layer when the slab moves.

After the overlay was cured, three strain gages were mounted on the surface at mid-slab just outside the wander path and mid-slab near the outside edge of the pavement on each of the selected slabs. These gages were installed to monitor the longitudinal surface strain. Gages were installed to monitor three slabs per test item per lane.

Dowel bars with strain gages were fabricated to monitor the bending force on the dowels. Two gages were mounted on opposite sides of each bar at the center. This arrangement provided measurement of the strain on the top and bottom of the bar. These instrumented bars were substituted for the manufactured bars nearest the corner. A pair of dowel bars was installed at each corner location, one in the longitudinal joint and the other in the transverse joint. All instrumented dowel bars were installed in the north lane. Two pairs of instrumented dowels were installed in test items 1 and 3, and only one pair was installed in test item 2.

2.2.3 Environmental Data.

Environmental data was collected continuously using the NAPTF (MUX3) static data collection system. The two environmental factors monitored during the testing period were moisture and temperature.

2.2.3.1 Texas Transportation Institute Moisture Study.

The Texas Transportation Institute (TTI) was contracted to monitor the early age moisture in the concrete. It was believed that valuable information regarding the effect of early age moisture, and curing methodology, could be gained from this effort. To establish a material baseline specific tests were conducted by TTI as follows:

- Measuring the free shrinkage of the concrete (ASTM C 157 1999)
- Relative humidity monitoring of the actual slabs
- Penetration testing of the mix (ASTM C 803 1999)
- Determining the time and conditions, including maturity, of concrete set

This information was used to establish the relative humidity-shrinkage curve, and to establish the set temperature and moisture gradients in each layer. The latter can be derived from the penetrometer-maturity relationship.

The TTI work included two three-day monitoring periods beginning at the placement of each layer, and three one-day (24 hour) monitoring periods to establish moisture trends in each layer before and after the placement of the top layer. Two sets of monitoring were carried out at the site: one for cure monitoring and the other for temperature and moisture profiles. The first was used to track curing quality, maturity (moisture based), and moisture loss; the second was used to provide data on how the temperature and moisture profiles develop over time throughout the concrete hardening process.

For each slab placement (overlay and underlay) a 12 inch diameter PVC casing (slightly lower than the slab thickness) was cast into the slab with fixtures for insertion of the slab monitoring instruments after placement. The PVC casing was filled with sand during the actual concrete placement process. This is shown in figure 17.

FIGURE 17. PVC CASING

In addition, the TTI monitoring activities included the following instrumentation:

- Two CMS units (each monitoring the surface and 1 inch below) - 4 nodes
- One independent chilled mirror unit
- One hand held capacitance unit
- One moisture monitoring unit, with three individual nodes.

From the data collected during the slab placement processes, the temperature and moisture gradients were obtained from the actual measurements recorded to characterize the concrete thermal conductivity and moisture diffusivity. Further analysis was subsequently carried out to calculate the temperature and moisture gradients in the other experiment test items. Set temperature and moisture gradients were calculated based on the set maturity, and equivalent linear temperature and moisture gradients were calculated for further mechanical analysis purposes. Results from this work are presented in a separate IPRF report, *Monitoring, Characterization, and Analysis of Early Age Concrete Pavement Behavior at FAA National Airport Pavement Test Facility (NAPTF)* (2007).

A similar setup for concrete moisture monitoring was considered for the QES experiment for longer term monitoring. However, the instrumentation was not installed for long term monitoring, and no data were collected using this methodology.

2.2.3.2 Temperature.

Thermistor trees were installed in both top and bottom slabs to monitor slab temperature gradients. Thermistors were located near top, bottom, and center of the slabs, regardless of slab thickness. The thermistor is a delicate device and requires extreme care for installation during construction. It is calibrated to provide a true temperature reading.

Six thermistor trees were fabricated and installed. Each tree consists of three thermistors to measure temperature at the bottom, middle and top of the slab. One thermistor tree is installed in the underlay and one in the overlay in the south test items. The thermistor tree in the overlay in test item S1 consists of four thermistors at the top, bottom, and one-third points.

2.3 SUMMARY.

Construction of the unbonded overlay test items at the NAPTF went reasonably well. While all aspects of the work were not perfect, the final pavement cross-sections complied with the instructions of the project advisory panel to construct a "real world" pavement. In other words, typical construction tolerances were achieved.

Several factors not typical of normal construction included the relatively low construction temperature and the indoor environment. Previous work at the facility had shown that slab curling/warping often associated with indoor slab construction was to be expected. Subsequent monitoring confirmed this expectation. Cold weather concreting techniques were required, but the indoor environment provided consistent temperatures and protection from all precipitation and direct solar radiation effects.

3. BASELINE EXPERIMENT TESTING AND OBSERVED RESULTS.

3.1 DATA ACQUISITION.

Data acquisition from the embedded instruments began immediately after construction of each pavement layer. Data were collected through two data acquisition boxes (identified as SPU3 and SPU4), each with three cards. In addition, the thermistor data sets, which are entirely static (not load-dependent) were collected separately, and supplied by the FAA in spreadsheet files. During loading, data sets from each SPU card were stored in a separate file for each load pass. Between loading periods, data was collected at regular time intervals, typically every hour, so that changes due to environmental conditions could be monitored.

The FAA provided the data in raw data files, and also provided a program for the conversion of the files to processed voltages or to engineering units; that program is called "TenView," as the responses from ten gages can be viewed on the screen at once. The TenView program was utilized directly for the monitoring of responses during the experiment. For subsequent data analysis, selected files were processed with TenView and full data sets stored in Excel. Spreadsheet macros were then developed for extracting the needed values. This procedure required each individual file to be processed separately using the series of programs. The development of a complete database of all responses is beyond the scope of the IPRF project.

3.2 DEFLECTION TESTING.

The FAA conducted heavy falling weight deflectometer (HWD) testing at requested intervals. The planned HWD testing pattern was painted on the pavement, as shown in appendix C. This testing plan included extensive joint and corner testing. The joint load transfer values did not change quickly over time, and the collection of this data was very time consuming. In addition, the planned testing pattern did not include center slab testing on all slabs. The center slab testing, which could be used for backcalculation of modulus values, and for monitoring the changing support conditions, was determined to be of greater value during the course of the project. Therefore, as the experiment progressed, fewer load transfer tests were performed, and all center slabs were tested on a more frequent basis. The actual (enhanced) HWD testing plan that was utilized for later testing is also included in appendix C.

The KUAB HWD testing was conducted with a four-drop loading sequence beginning with an approximate 36,000-lb seating load. The subsequent loads were approximately 12,000 lbs, 24,000 lbs, and 36,000 lbs. Nine sets of deflection testing were conducted on the overlay slabs. Deflection testing was also performed directly on the underlay at the 12,000-lb load level. Plots of the deflection basins are included in appendix D, both by test item and by date. The overlay plots in the appendix are normalized to a load of 36,000 lbs. While these plots each contain a large amount of data, they do allow an overall observation of the changes in deflection with time. While the maximum deflections increased as the test items deteriorated, the degree of variability between the responses of the individual slabs within each test item also clearly increased. For example, figure 18 shows the relatively low values of deflection and variability between test items and slabs before the initiation of loading. Figure 19 shows the increase in both deflection values and variability at the conclusion of loading on the overlay.

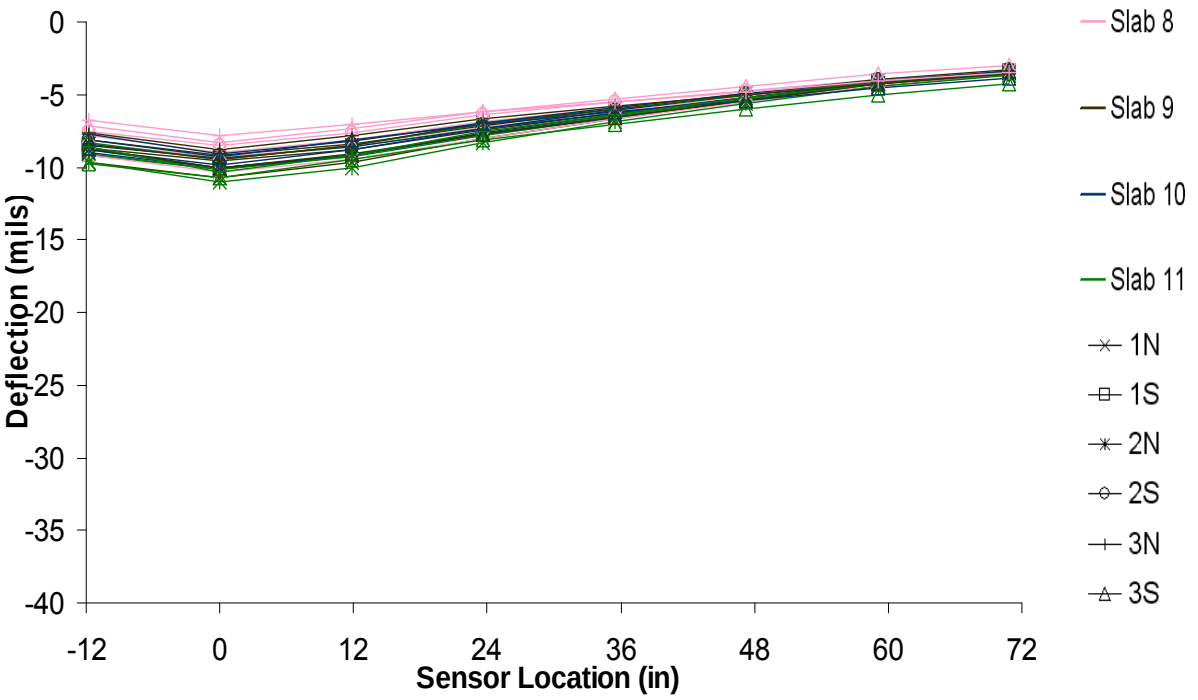

FIGURE 18. DEFLECTION BASINS ON 7/24/2006 PRIOR TO LOADING (NORMALIZED TO A 36,000-LB LOAD)

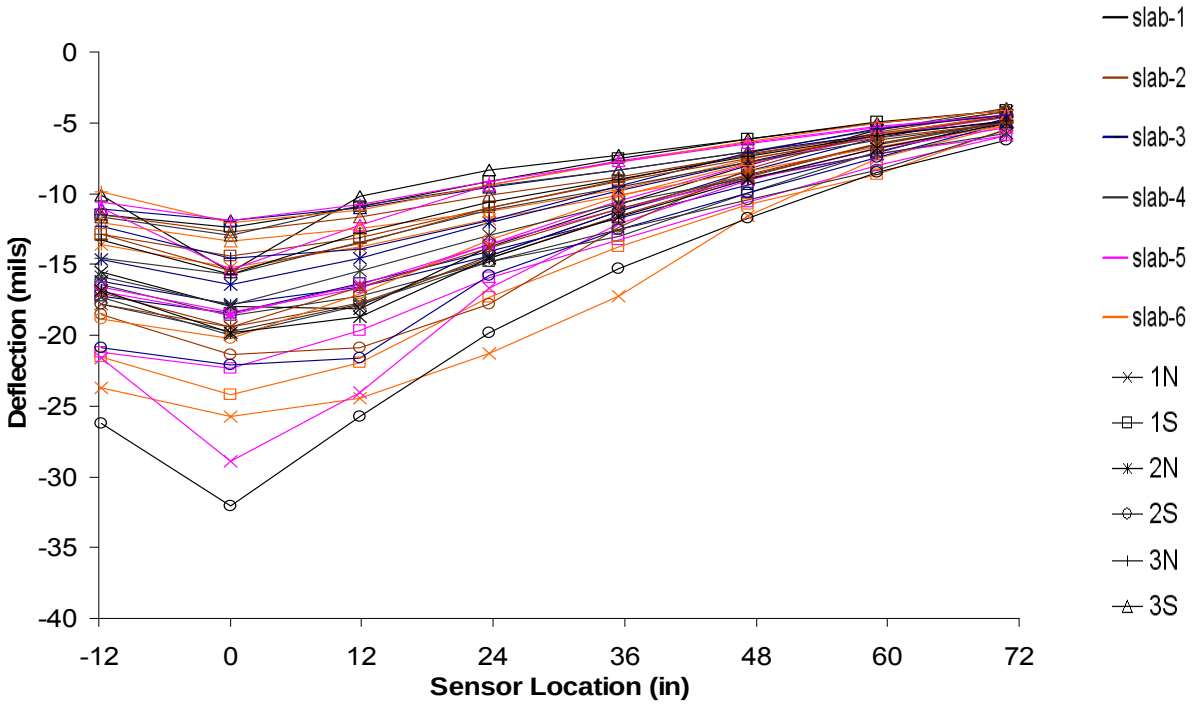

FIGURE 19. DEFLECTION BASINS ON 11/7/2006 AFTER 16567 PASSES ON S2, 12142 PASSES ON S1 AND S3, AND 5146 PASSES ON NORTH TEST ITEMS (NORMALIZED TO A 36,000-LB LOAD)

3.3 ENVIRONMENTAL MONITORING.

3.3.1 Pavement Temperatures.

Environmental data, including data from the embedded thermistor trees, were collected at half-hour intervals throughout the experiment. The internal temperatures of the slabs are graphically presented in appendix E, with the plots focused on a number of dates spread over the course of the experiment. The selected dates are 7/14/2006, 7/25/2006, 8/15/2006, 8/31/2006, 09/10/06, 9/26/2006, 10/21/2006 and 11/12/2006. Figure 20 is an example of a plot of the temperature profiles throughout the cross-section of test item S3, including the three thermistors in the 6-inch overlay and the three thermistors in the 10-inch underlay. From these plots, the gradient reversals over a day can be observed.

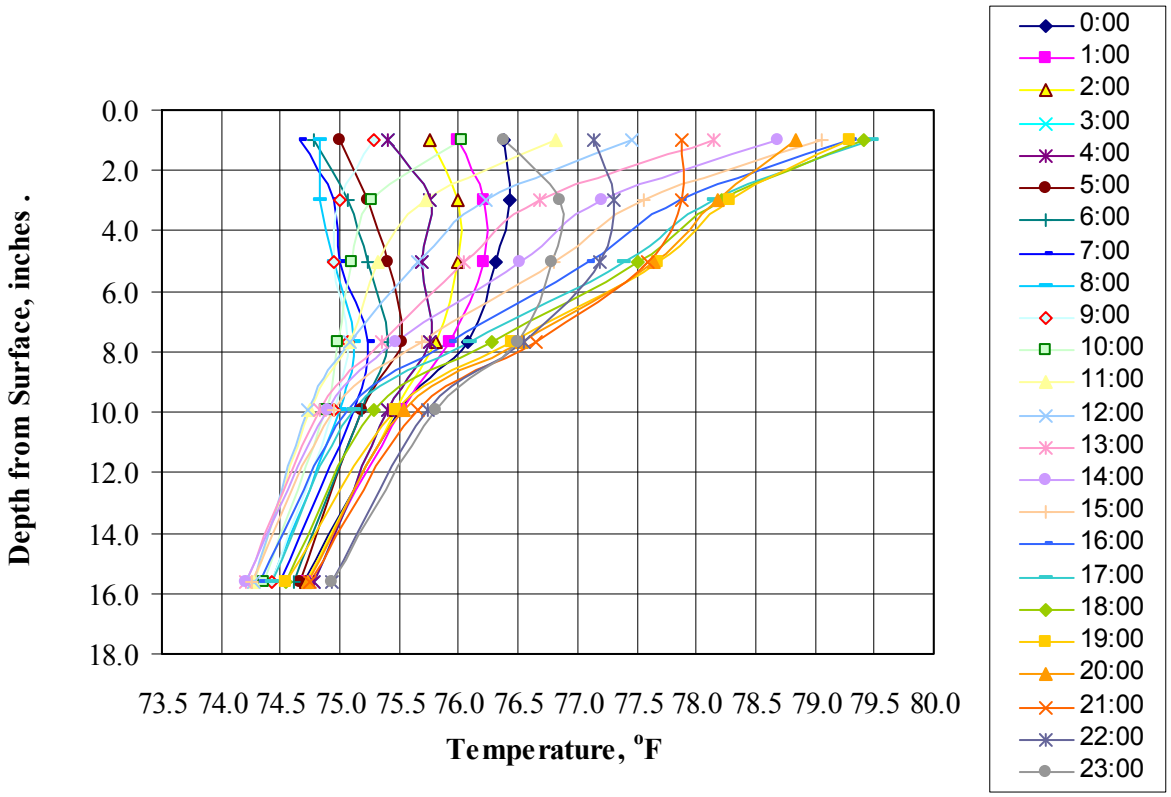

FIGURE 20. TEMPERATURE PROFILES AT HOURLY INTERVALS ON 7/14/2006 FOR TEST ITEM S3

Additional plots in appendix E were prepared to examine the temperature changes over the entire experimental period. Those plots were prepared for approximately 5:00 a.m. That approximate time was utilized for other monitoring as well, as there are typically relatively smaller temperature gradients and less testing activity. An example plot, showing the temperatures in test item S3 from July to November, is shown in figure 21. Plots were also generated to examine the temperature gradients in both overlay and underlay slabs on different dates, and the diurnal changes over the course of those days. Those graphs are also included in appendix E.

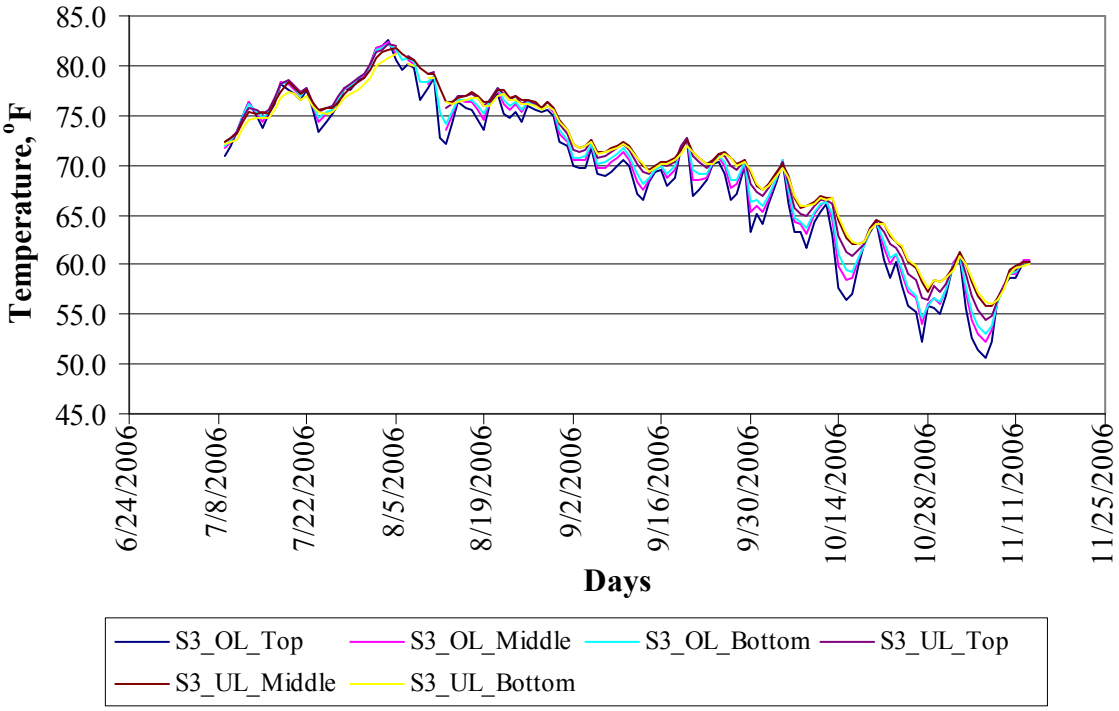

FIGURE 21. TEMPERATURE OF SLABS AT 5:00 A.M. FOR TEST ITEM S3

3.3.2 Monitoring and Watering for Control of Curl.

Readings for all remaining gages were collected at regular intervals when loading was not in process. Typically, data were recorded at one hour intervals. The primary use of this data has been for monitoring elevations with the LPTs, as the slabs respond to changes in temperature and internal humidity.

While the experiment was conducted indoors at the NAPTF facility, no heating or cooling was available. Further, the FAA's past experience and monitoring has shown that shrinkage is accentuated in the drier indoor environment. So, while temperature gradients are somewhat damped from the outdoor environment, attention had to be given to the monitoring and attempted control of corner curl of the slabs.

The slabs were watered in order to minimize moisture gradients. Watering increases the humidity in the top surface and thereby reduces the negative moisture gradient and minimizes upward curling. The curl was monitored, using the LPTs, to help establish the watering schedule. The concrete slabs were watered generally twice a week during the months of August, September and October of 2006. The watering dates are presented in figure 22, with the letter "W" indicating the days of watering. The slabs were typically watered in the afternoon, after loading or other testing and monitoring activities.

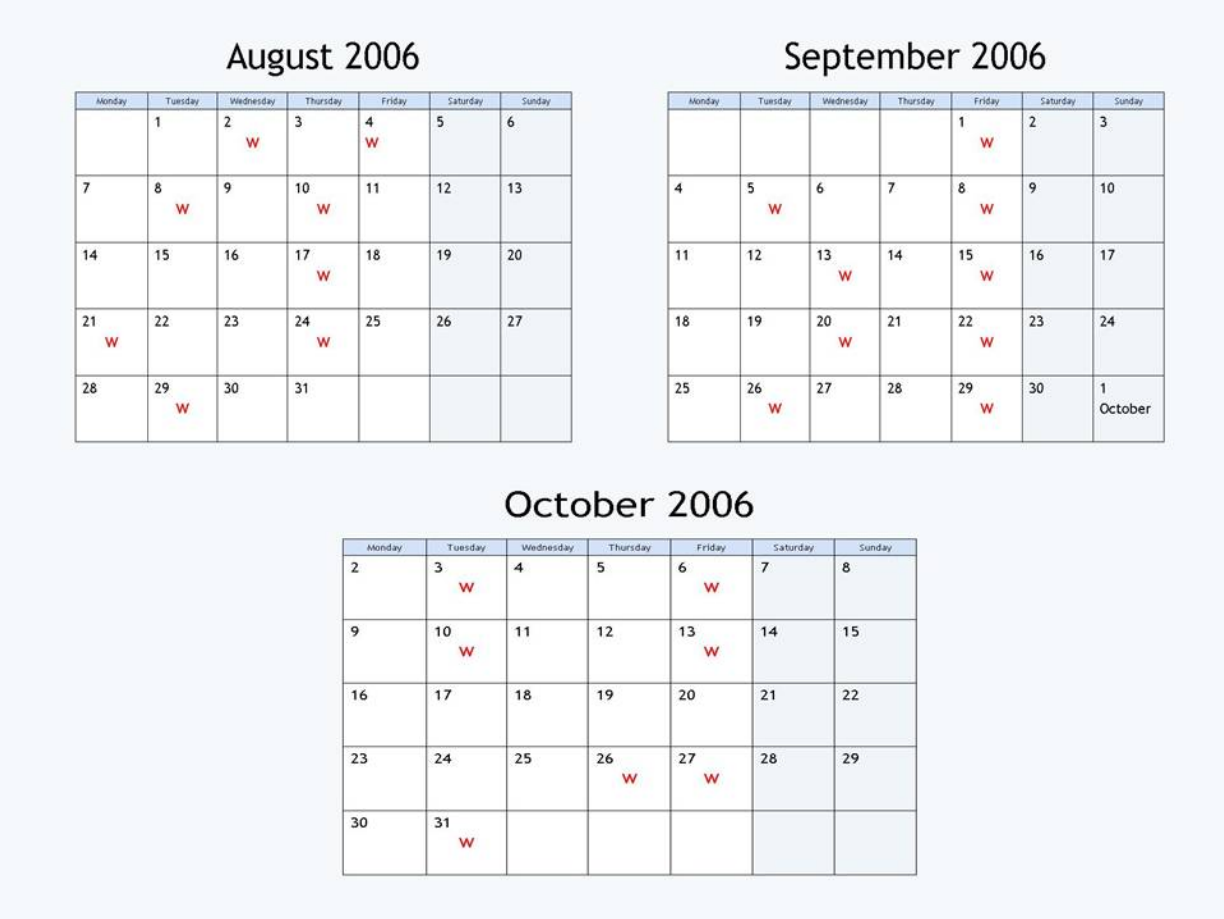

FIGURE 22. DATES OF SURFACE WATERING (W INDICATES WATERING DAYS)

3.3.2.1 Diurnal Variations of Slab Movements.

The diurnal variations of environmental factors such as temperature and humidity influence the movement of slabs; the resulting movements were monitored with the LPTs. Four LPTs (LPT-O-N2-3, LPT-O-N1-11, LPT-O-N2-5 and LPT-O-N3-9) were selected from different areas of the pavement and positions for four selected days extracted. Figure 23 and figure 24 show the movement of the LPTs on May 1 and June 2, 2006, indicating diurnal variations on different locations of the pavement before and after a seating load was applied. The LPT readings were normalized to their corresponding readings at 12 a.m. (midnight) for comparison purposes.

The diurnal variations of LPTs on May 1, 2006, shown in figure 23, indicate that the LPTs in the corners and the outside edge moved upwards between 5:00 a.m and 9:00 a.m. and moved downwards between 15:00 and 19:00 hours, whereas the LPT-O-N3-9 in the midslab location moved inversely. These trends are indicative of typical concrete slab movements. The diurnal variations on June 2, 2006, shown in figure 24, indicate a similar behavior of LPTs in the corners and the outside edge. The midslab LPT exhibited a similar inverse trend of much smaller variations. This trend may be due to the effect of the seating load applied on May 22, 2006, with the midslab restrained with the asphalt interlayer and self-weight.

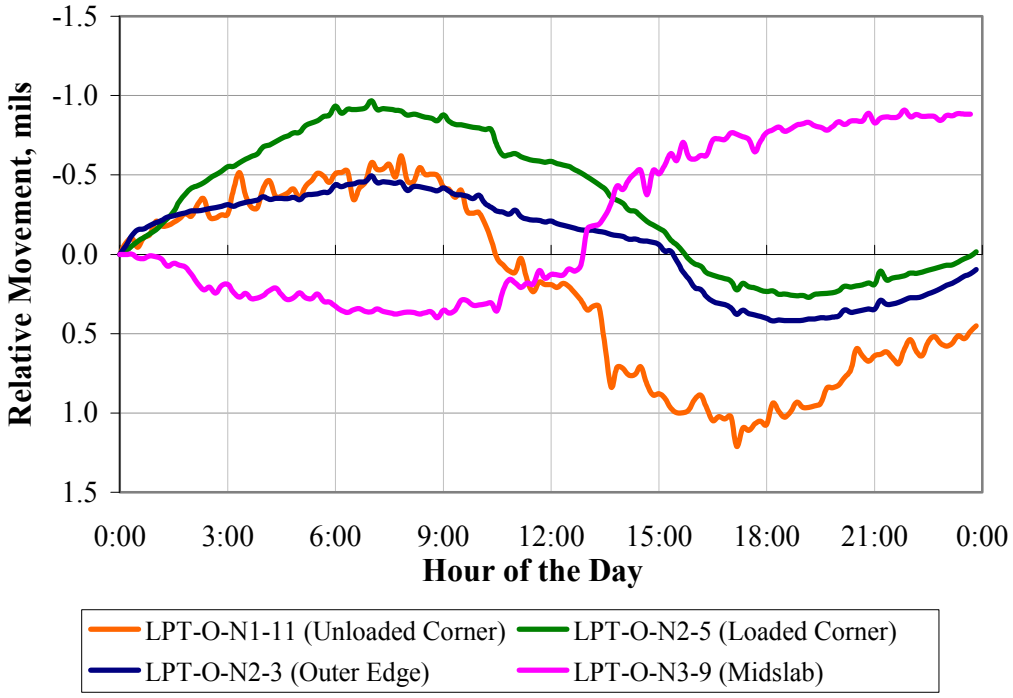

FIGURE 23. DIURNAL VARIATIONS OF LPTS ON MAY 1, 2006 (BEFORE SEATING LOAD)

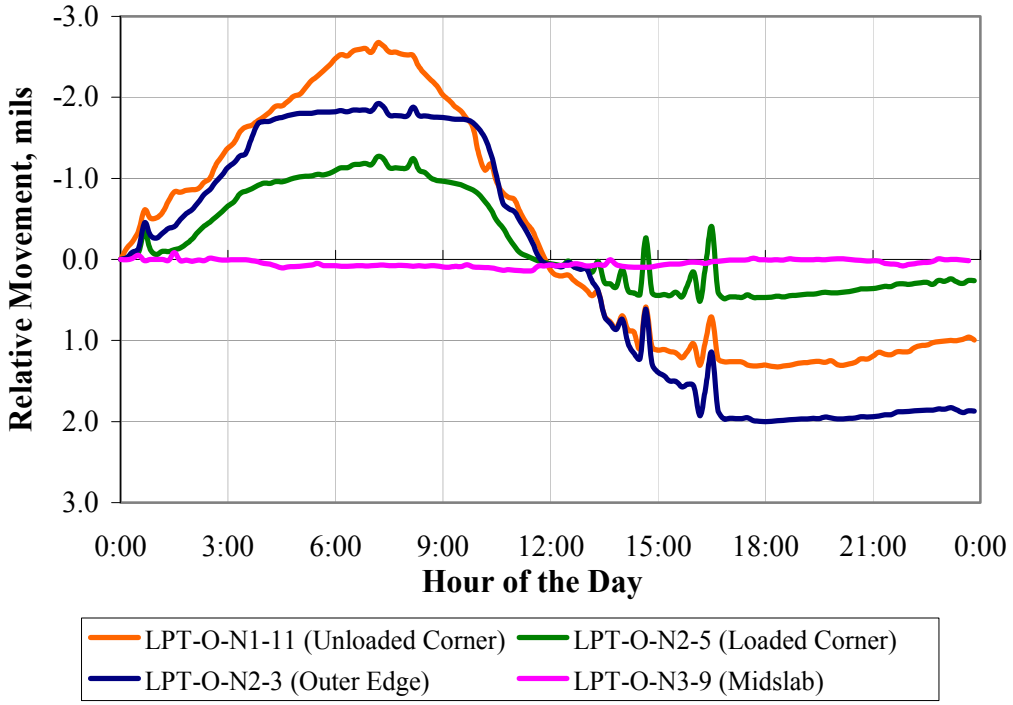

FIGURE 24. DIURNAL VARIATIONS OF LPTS ON JUNE 2, 2006 (AFTER SEATING LOAD)

The diurnal movements of LPTs on August 5 and September 30, 2006, are shown in figure 25 and figure 26, respectively, after loading had begun. The variations on August 5 indicate the early distress condition of the overlay, with a few longitudinal cracks. On August 5, the LPT in the loaded corner (LPT-O-N2-5) exhibited significant increase in upward curl between 1:00 a.m. and 4:30 a.m., followed by a significant decline for an hour, and another steep increase in upward curl between 5:30 a.m. and 9:00 a.m. This steep rise and fall of the LPT can be attributed to crack development and aggregate interlock. The other two LPTs on the unloaded corner and edge exhibited typical behavior. The midslab LPT exhibited a typical inverse trend with much smaller variations not exceeding 0.1 mils.

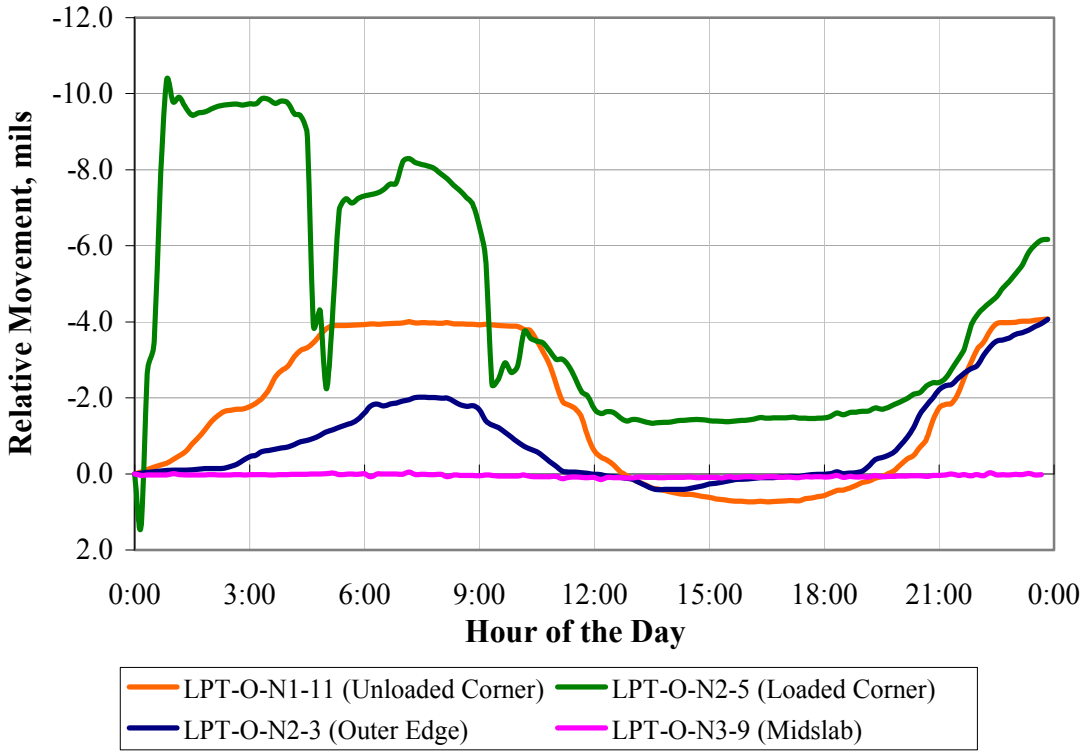

FIGURE 25. DIURNAL VARIATIONS OF LPTS ON AUGUST 5, 2006 (INITIAL LOADING PHASE)

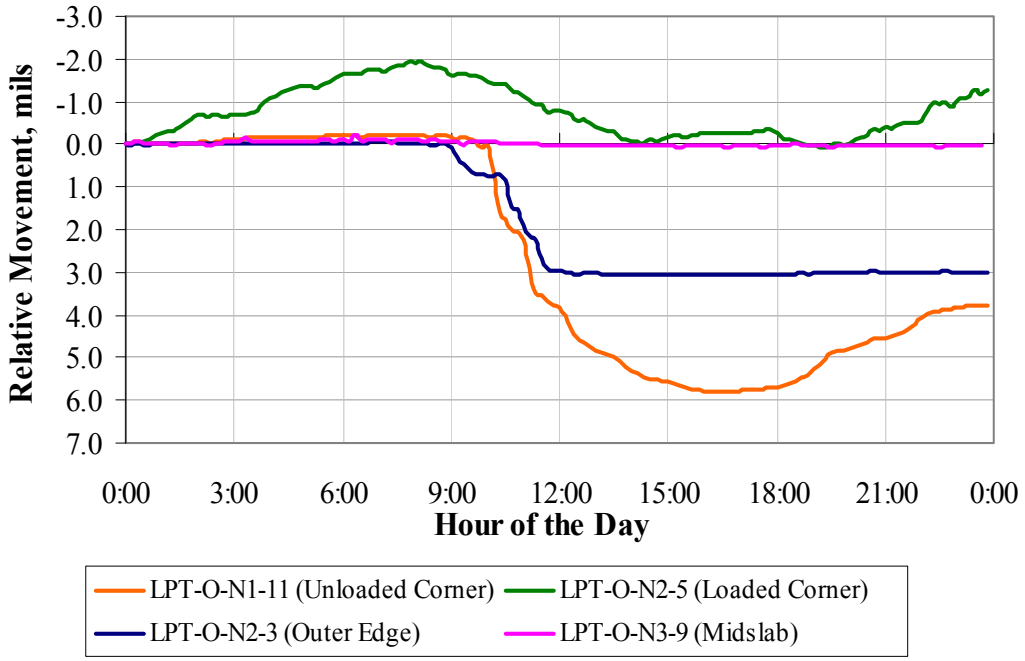

FIGURE 26. DIURNAL VARIATIONS OF LPTS ON SEPTEMBER 30, 2006 (FINAL LOADING PHASE)

On September 30, the north test items had reached their final distressed condition. The LPTs in the loaded corner exhibited significant upward curl in the early morning and insignificant downward curl in the late afternoon. The LPTs in the unloaded corner and the edge exhibited little or no upward curl in the morning and significant downward curl in the afternoon. The midslab LPT-O-N3-9 exhibited similar behavior to LPT-O-N2-5, opposite to its usual trends, but with much smaller magnitudes. Cracks had developed all around the vicinity of LPT-O-N3-9.

3.3.2.2 Effects of Watering on Slab Movements.

The LPT readings were extracted for the days of watering as well as for the days after watering. The time of measurement was generally between 5:00 a.m. and 7:30 a.m., to maintain consistency. The total number of days watered was 24, but suitable data was only available for 18 days, due to loading occurring at that time of day on other dates. The slabs are expected to accumulate downward deflection under continued loading passes, and thus loading intervals may not be suitable for evaluating the effects of watering.

Four LPTs were selected for a test item, representing an edge, loaded corner, midslab and unloaded corner. The sensor readings were collected from August 17, 2006 through October 26, 2006 from static (nonloading) files. The difference between the LPT readings on the day after watering and the day of watering was calculated. A positive difference indicates that the point has moved downwards. The differences in LPT readings are plotted for each of the north test items in figure 27, figure 28 and figure 29, respectively. The overlay LPTs, N1-2, N2-1 and N3-1, are located at the edge of the test items, whereas LPTs N1-10, N2-11 and N3-10 are located in

midslab locations. Overlay LPTs N1-5, N2-7 and N3-4 are located in the loaded corners of the slabs, and LPTs N1-12, N2-14 and N3-14 are located in the unloaded corners of the slabs.

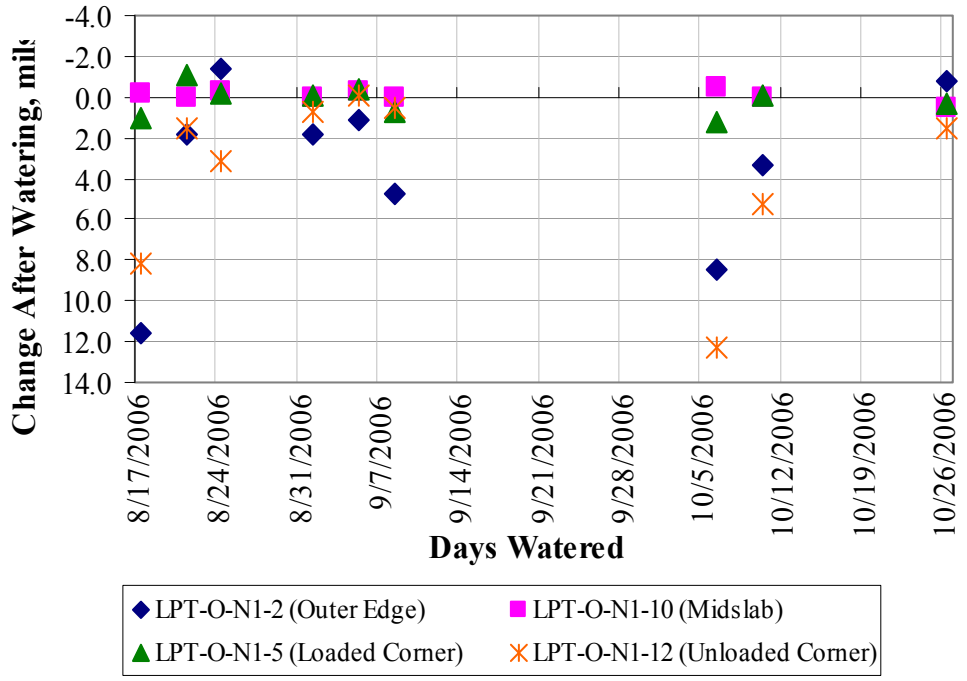

FIGURE 27. CHANGES IN LPT RESPONSES DUE TO WATERING, TEST ITEM N1

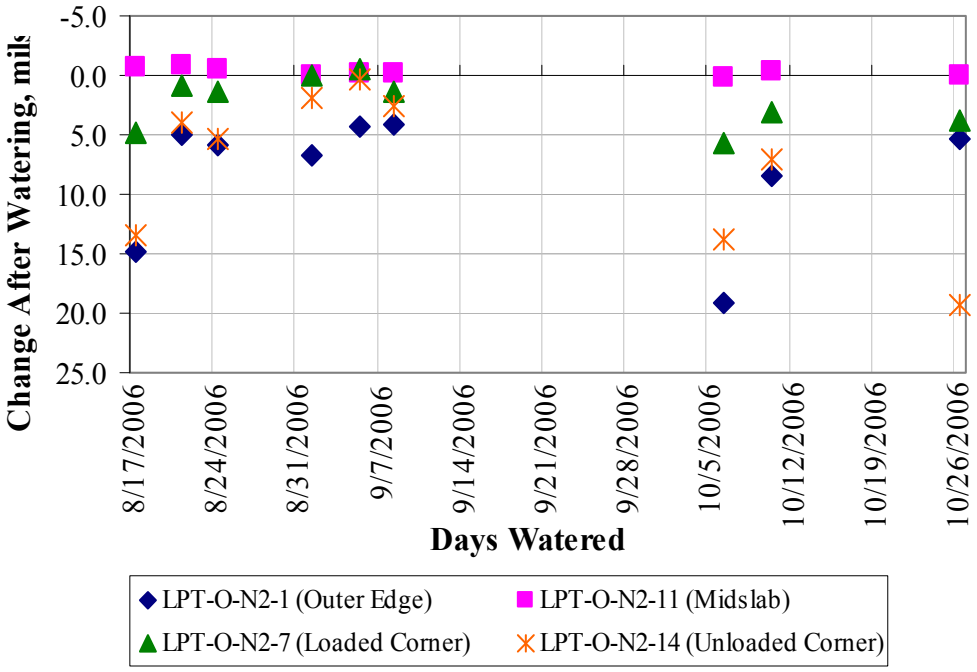

FIGURE 28. CHANGES IN LPT RESPONSES DUE TO WATERING, TEST ITEM N2

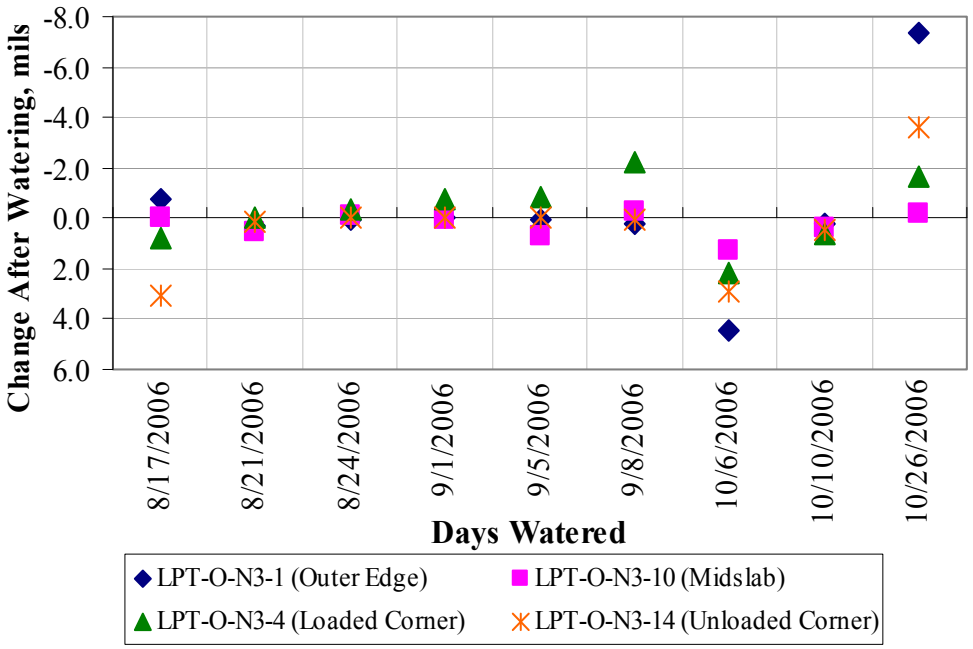

FIGURE 29. CHANGES IN LPT RESPONSES DUE TO WATERING, TEST ITEM N3

The LPTs in the outside edge of the pavement exhibited downward movement with watering. For most days, the LPT-O-N2-1 moved downwards by approximately 5 mils, whereas LPT-O-N1-2 moved downwards only about 2 mils. LPT-O-N3-1 generally did not exhibit a significant change. The LPTs in the unloaded corners of the slabs generally followed the trends of the LPTs in the outside edge. These LPTs showed significant downward movement due to watering in test items N1 and N2 and insignificant movement in test item N3. The LPTs in the loaded corner and midslab locations exhibited little or no change, with variations of about 1 mil in either direction. In general, the LPTs in the outside edge and the unloaded corners had shown significant recovery (downward movement) from watering. These LPTs were outside the wheel track and were not subjected to direct loading. However, the LPTs in the wheel track showed little or no change after watering.

3.3.2.3 Curl During the Progress of the Loading Experiment.

Figure 30, figure 31 and figure 32 show the progress of movement of the selected LPTs from August through October, 2006 in test items N1, N2 and N3, respectively. The figures indicate the relative movement of the LPTs from the baseline reference values. The LPTs in the outside edge and the unloaded corners (except LPT-O-N3-14) had moved upwards whereas the LPTs inside the wheel track had moved downwards since loading had begun. The LPTs outside the wheel track, which had moved upwards since construction, had only exhibited partial recovery from watering. Since the LPTs in the wheel track accumulated downward deflection under loading, the effect of watering on recovery of upward curl is indiscernible.

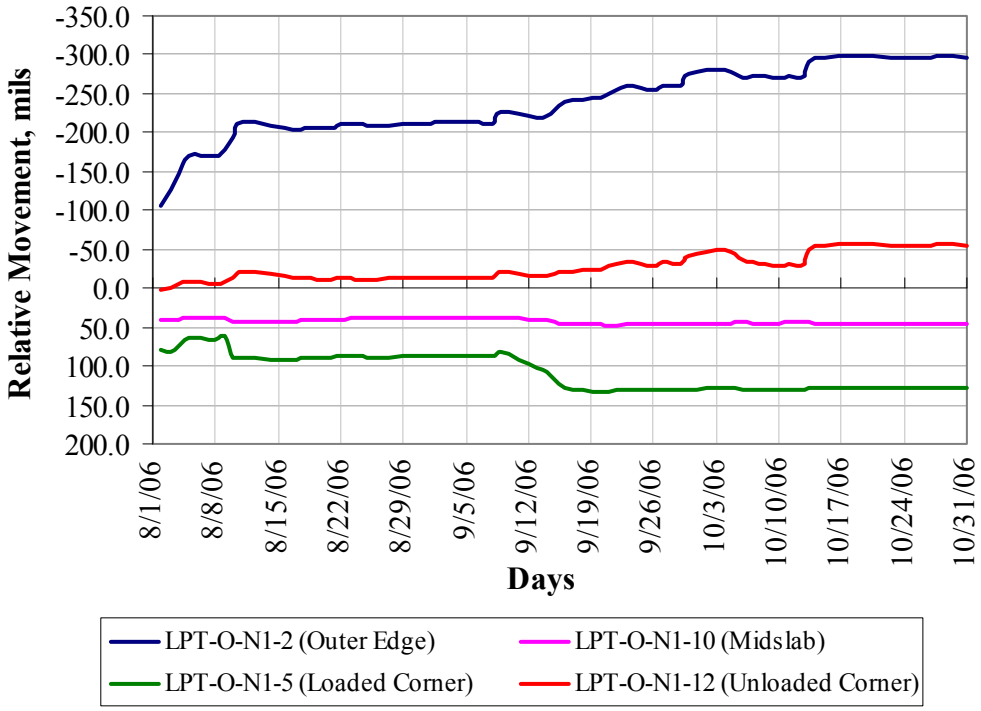

FIGURE 30. RESPONSES OF SELECTED LPTS IN TEST ITEM N1 (AUGUST TO OCTOBER, 2006)

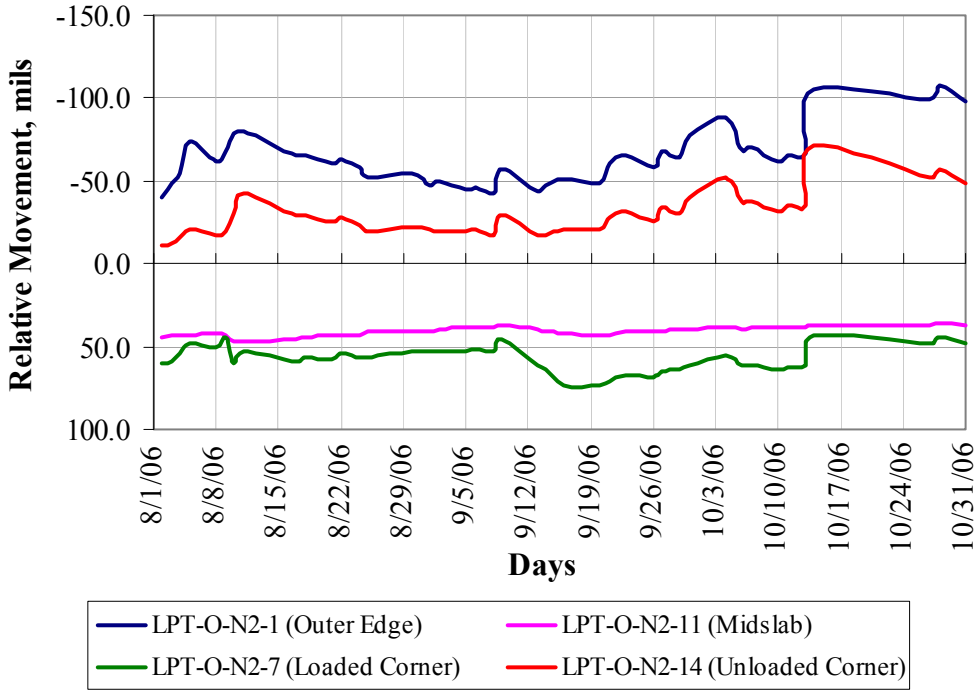

FIGURE 31. RESPONSES OF SELECTED LPTS IN TEST ITEM N2 (AUGUST TO OCTOBER, 2006)

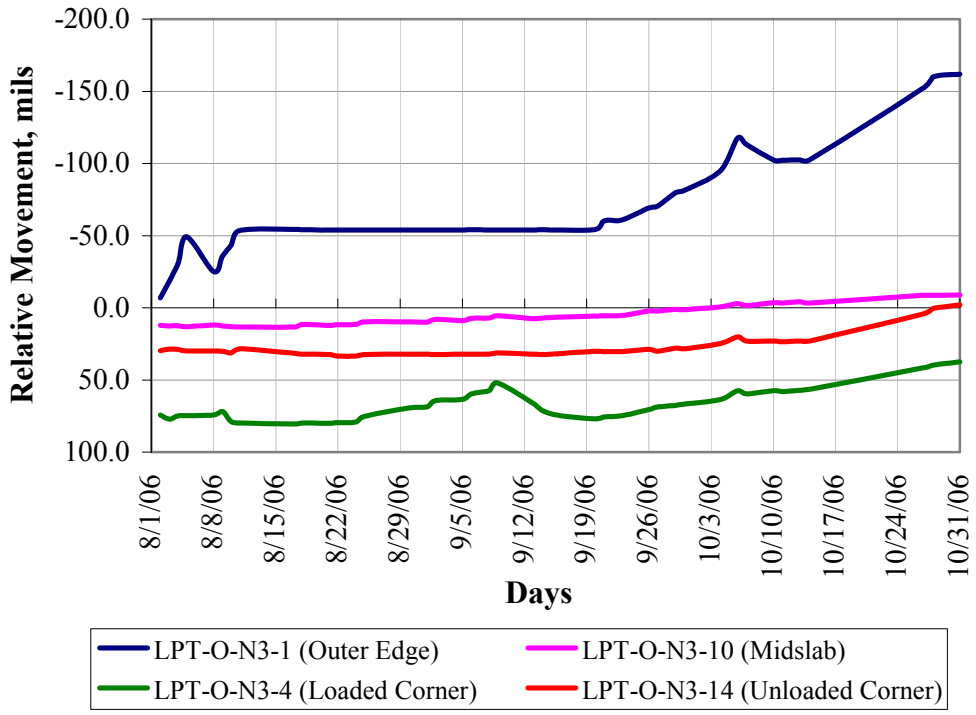

FIGURE 32. RESPONSES OF SELECTED LPTS IN TEST ITEM N3 (AUGUST TO OCTOBER, 2006)

3.4 LOADING.

3.4.1 Load Configurations.

The NAPTF test vehicle has two carriages which can be used for loading simultaneously, or independently. Each carriage also has flexibility in the choice of gear configuration, the selection of wheel load level, and in carriage position. During loading, the FAA personnel at the NAPTF monitored the control of the wheel load level and carriage position. The load control information was made available to the project team. The wheel load levels were within control throughout the experiment, and thus only the target wheel loads are reported here. Tire pressures were also monitored, with an unloaded inflation pressure of 233 psi. The use of a constant inflation pressure means that contact areas vary with load level. The test speed was three miles per hour. Further information on the control of loading is included in appendix F.

The gear configurations used at the NAPTF during this experiment are illustrated in figure 33. For failure loading, the triple dual tandem gear was used on the north test items, and the dual tandem gear was used on the south test items. The remaining gears were used only for preloading and static testing. The dual tandem and triple dual tandem gears, while representative of true aircraft gears, do not have the exact dimensions of in-service aircraft. The gear positions have been established such that the wheel and axle spacings are the same for all configurations. The dual wheels are spaced at 54 inches center-to-center. The spacing between axles is 57 inches.

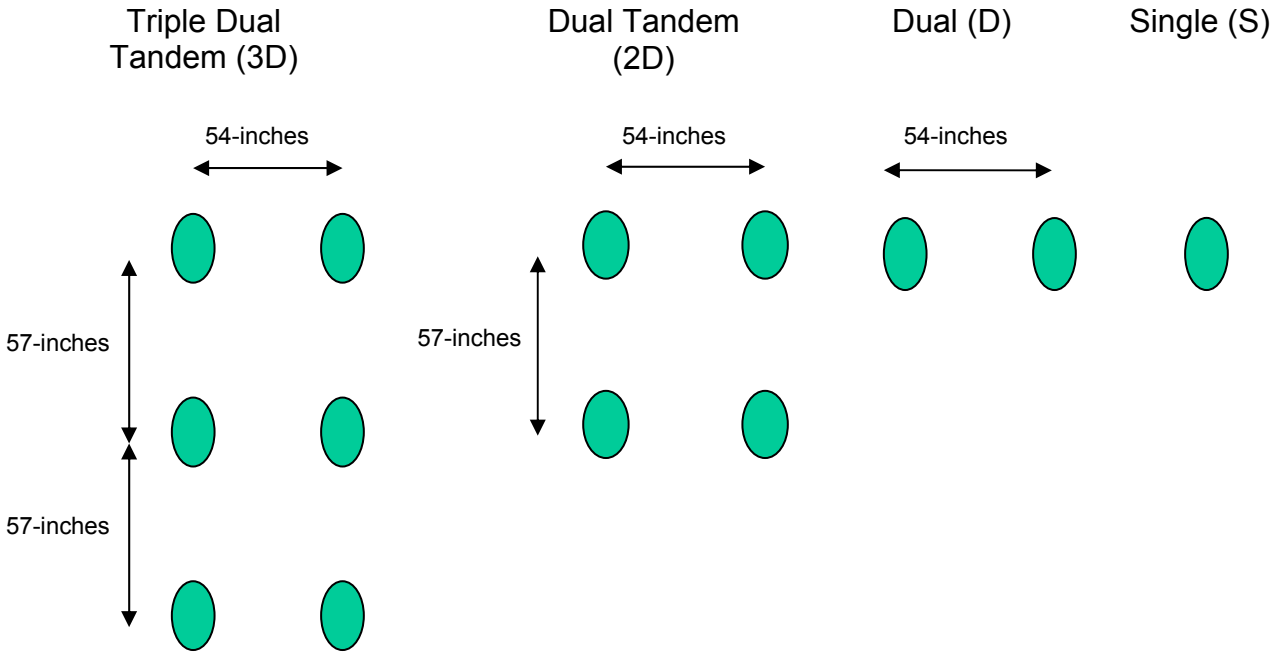

FIGURE 33. GEAR CONFIGURATIONS

The transverse position of the carriages was shifted between passes to simulate vehicle wander. A wander pattern consisted of 66 passes, with each passage of the test vehicle to the east being counted as a pass, and the return to the west counting as a second pass. The carriage completed the two-pass down and back cycle before being shifted. A wander pattern consisting of nine carriage (gear) positions, each shifted by 10.25 inches was used for all dynamic loading with the test vehicle. This wander pattern was previously used by the FAA at the NAPTF, and was determined to be a reasonable estimation of real airfield wander patterns. By using the same pattern, the ability to compare failure data across construction and testing cycles at the NAPTF is also improved. The standard wander pattern and track frequencies are shown in figure 34.

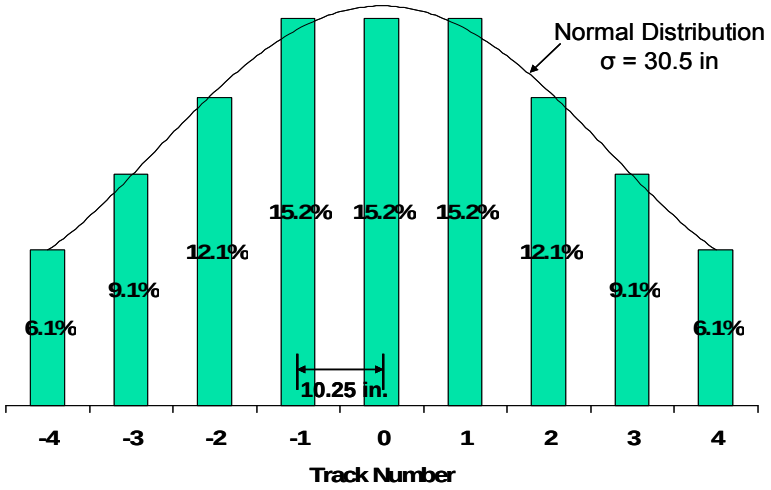

FIGURE 34. WANDER PATTERN AND TRACK FREQUENCIES

The zero track was located such that the outside wheel was immediately adjacent to the overlay longitudinal joint centered within each test item. The target carriage locations from the zero track for each carriage are provided in table 17. As construction was not precisely symmetric about the centerline transition slabs, slight adjustments were required to establish the zeros for the initial loading table. The loading track positions relative to both the overlay and underlay joints are shown in figure 35.

TABLE 17. CARRIAGE LOCATIONS FOR LOADING

Track No.	Carriage Centerline Location (feet)	
	North	South
-4	-18.167	11.333
-3	-17.313	12.188
-2	-16.458	13.042
-1	-15.604	13.896
0	-14.750	14.750
1	-13.896	15.604
2	-13.042	16.458
3	-12.188	17.313
4	-11.333	18.167

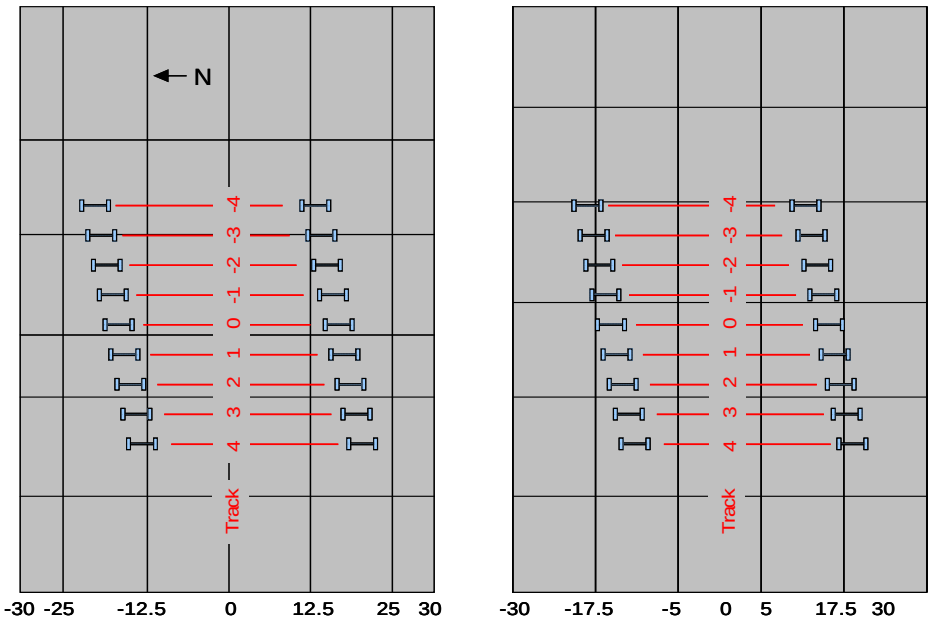

FIGURE 35. LOADING POSITIONS RELATIVE TO UNDERLAY (LEFT) AND OVERLAY (RIGHT) JOINTS

Test vehicle loading of the test items occurred in a number of stages. The dates and wheel loads for each stage of loading are summarized in table 18. The number of wanders and dates for the failure loading varied by test item.

TABLE 18. LOADING SEQUENCES

Dates	Wanders	Wheel Loads (lbs)	Purpose
3/14/2006	44 passes	10000	Seating Load on Underlay
3/14/2006 to 3/15/2006	4	15000	Gear Response Loading on Underlay
3/15/2006	NA	10000	Static Loading on Underlay
5/22/2006 to 5/23/2006	88 passes	10000	Seating Load on Overlay
5/23/2006	NA	15000	Static Loading on Overlay
5/23/2006 to 5/24/2006	4	20000	Gear Response Loading on Overlay
7/6/2006	NA	20000	Interaction Loading
7/6/2006 to 7/12/2006	1 2 3	20000 30000 40000	Ramp-up Loading
7/25/2006 to 10/31/2006	Varied	50000	Failure Loading

3.4.2 Seating and Gear Response Loads.

3.4.2.1 Seating and Gear Response Loading of Underlay Slabs.

The underlay slabs were seated on March 14, 2006 with the load applied at 10-inch transverse carriage intervals across the pavement. The LPT readings measured at 5:00 am on March 14 and 15, 2006, were compared to examine the effects of the seating on vertical position, and to compare the LPT readings after seating with the baseline reference values. Table 19 provides the range of differences in LPT readings for each test item. The seating loads did not affect the LPT positions substantially, as compared to the range of movement from the baseline reference position.

TABLE 19. MAXIMUM RANGE OF DIFFERENCES IN LPT READINGS BEFORE AND AFTER SEATING OF UNDERLAY SLABS

Test Item	Range of Differences in LPT Responses (mils)	
	Before and After Seating	Baseline and After Seating
N1	-3.4 to +3.1	-19.7 to + 33.8
N2	-1.7 to +1.1	-1.3 to -16.5
N3	+0.8 to +1.6	-5.8 to -15.1

Subsequent to the seating, four wander patterns were applied directly to the underlay with a wheel load of 15,000 lbs. These wanders were applied with the different gear configurations, so that response data would later be available for comparison, if needed.

3.4.2.2 Seating and Gear Response Loads of Overlay Slabs.

The overlay slabs were seated on May 22, 2006, with the load applied at 10-inch transverse carriage intervals across the pavement. The LPT readings were measured at 5:00 a.m. on the day of seating and at 6:46 a.m. on May 23, the day after initial seating. Table 20 provides the differences in LPT readings between these two days. The differences in LPT value indicates that the LPTs in the edges and corners had moved upwards, whereas the midslab LPTs had moved downwards. The LPTs at the free edges had moved upward more than the LPTs in the interior corners. This observed movement was more pronounced in thicker slabs.

TABLE 20. DIFFERENCE IN LPT READINGS BEFORE AND AFTER SEATING (POSITIVE INDICATES DOWNWARD MOVEMENT; NEGATIVE INDICATES UPWARD MOVEMENT)

Test Item	Range of Differences in LPT Responses (mils)			
	Edges	**Loaded Corners**	**Midslab**	**Unloaded Corners**
N1	-17.5	-7.9 to -11.2	+2.0 to +4.3	-4.6 to -11.6
N2	-9.0 to -12.1	-1.9 to -4.5	+0.1 to +1.21	-0.6 to - 9.9
N3	-14.26	-10.7 to +0.2	-0.03 to +1.9	-0.1 to -2.0

The readings taken at 6:46 am, May 23, 2006 were also compared with baseline reference positions as shown in table 21. The differences in LPT positions indicate that the slabs exhibited upward movement at the free edges. The magnitude of movement varied between test items, and was again more pronounced in thicker slabs.

TABLE 21. DIFFERENCE IN LPT READINGS BETWEEN BASELINE AND AFTER SEATING (POSITIVE INDICATES DOWNWARD MOVEMENT; NEGATIVE INDICATES UPWARD MOVEMENT)

Test Item	Range of Differences in LPT Responses (mils)			
	Edges	**Loaded Corners**	**Midslab**	**Unloaded Corners**
N1	-34.5	-18.8 to -81.8	-5.5 to + 8.4	-5.5 to -23.5
N2	-22.5 to -26.7	-4.1 to -17.6	-1.6 to +5.4	-2.9 to -22.9
N3	-18.7	-6.2 to +15.1	8.8 to 11.4	-2.5 to 10.5

Subsequently, four wander patterns were applied directly to the underlay with a wheel load of 20,000 lbs. These wanders were applied with the different gear configurations, so that response data would later be available for comparison, if needed.

3.4.3 Static Loading.

Static loading of the underlay slab was performed with an outside wheel load directly over embedded strain gages and selected LPTs, providing a check on responsiveness of the gages. Similarly, static loading of the overlay was conducted. A 10,000-lb wheel load was utilized for the static testing of the underlay, and a 15,000-lb wheel load was utilized for the static testing of the overlay. As a result of the static testing, it was concluded that over 98 percent of the gages were responsive.

3.4.4 Interaction and Ramp-up Loading.

Interaction loading was performed on the overlay on July 6, 2006. The purpose of this loading was to examine the gage responses in adjacent test items during the loading. Loads were applied in the outer position to the north test items, and then to the south test items, independently. Examination of the instrumentation data from the opposing test items showed no significant dynamic responses.

Ramp-up loading was performed on the overlay from July 6 to July 12, 2006. The ramp-up loading was conducted with the full wander pattern. The triple dual tandem gear configuration was used on the north test items and the dual tandem gear configuration was used on the south test items. During and after each wander, the embedded gage responses were examined. The wheel loads were increased in 10,000-lb increments, with some days between each increase to allow for analysis of the data. The 30,000-lb wheel load was applied for two wander patterns, and the 40,000-lb wheel load was applied for three wander patterns. The additional wander was applied at the 40,000-lb wheel load because the dynamic responses were gradually changing with subsequent passes in the same track, indicating that a stable structure had not yet been reached. After three wanders, the responses stabilized.

The strain responses were extracted for each of the embedded strain gages for selected passes. In general, the greatest responses were observed for track 0 loading, which placed an outside wheel load directly over the gages. An example of the extracted strain gage data from ramp-up loading is shown in table 22. The strain values were measured as the amplitude from the unloaded baseline measurement to the peak strain.

3.4.5 Failure Loading.

3.4.5.1 Selection of Wheel Load.

The design cross-sections for the test items had been selected after careful evaluation with a variety of programs and fatigue equations. However, the as-built thicknesses and material characteristics varied slightly from the original assumptions. The experimental plan called for using the same wheel load on both the north test items, which would be tested with the triple dual tandem, and on the south test items, which would be tested with the dual tandem. This meant that there had to be a careful balance in order to reach a reasonable number of passes before failure on both sides, while not having any test item survive to a number of passes beyond

the project time frame. Future increases in load level were to be avoided to prevent confounding of the analysis.

TABLE 22. MICROSTRAINS FOR SELECTED PASSES ON TRACK 0 FOR EMBEDDED STRAIN GAGE POSITION 2 IN TEST ITEM N1 (TENSION IS NEGATIVE)

Date	Wheel Load	Wander	SPU-Card	Gage	Channel	Pass 48	Pass 54	Pass 66
7/6/06	20000	Final	S3-C2	EG-U-N1-2 B	4	-13.8	-15.1	-13.9
				EG-U-N1-2 T	6	11.8	12.5	10.6
				EG-O-N1-2 B	28	-26.1	-28.1	-26.9
				EG-O-N1-2 T	30	31.9	30.9	29.8
7/10/06	30000	Final	S3-C2	EG-U-N1-2 B	4	-19.2	-18.2	-19.7
				EG-U-N1-2 T	6	17.0	16.0	16.4
				EG-O-N1-2 B	28	-35.3	-38.5	-34.8
				EG-O-N1-2 T	30	51.5	49.7	51.1
7/12/06	40000	Final	S3-C2	EG-U-N1-2 B	4	-24.3	-25.6	-24.3
				EG-U-N1-2 T	6	25.5	25.4	24.8
				EG-O-N1-2 B	28	-39.9	-35.4	-37.0
				EG-O-N1-2 T	30	66.7	66.0	71.5

In addition, the instrumentation responses from the ramp-up loading were available to be considered in determination of the final wheel load level for failure loading. Considering the vertical position of each of the gages in the slab, and the strains at the top and bottom gages, the extreme fiber strains in both the underlay and overlay were estimated. These strains were computed at each of the ramp-up loading levels, and then linearly extrapolated to potential wheel load levels for the failure loading. When these numbers were initially calculated, the strains seemed small, and the final decision on failure wheel load depended more heavily on mechanistic analysis. Later, an error in the application of the gage calibration factors was discovered. A corrected example of the projected extreme fiber strains is shown in table 23.

TABLE 23. EXTRAPOLATED EXTREME FIBER STRAINS FOR TRACK 0 LOADING

Gage Location	Wheel Load (lbs)	Microstrain	
		Top (compression)	Bottom (tension)
EG-U-N1-1 (underlay slab in test item N1)	45000	66.0	37.7
	50000	73.5	41.9
	55000	81.0	46.2
	60000	88.5	50.4
	65000	96.0	54.7
EG-O-N1-1 T (overlay slab in test item N1)	45000	125.8	87.3
	50000	138.9	95.7
	55000	152.0	104.0
	60000	165.2	112.4
	65000	178.3	120.7

The original design calculations were repeated with the as-built thicknesses and wheel load levels of 40,000, 50,000 and 60,000 lbs. Selected results are shown in table 24. The calculations completed with the FAA design programs utilized the aircraft closest to the test vehicle gear configurations. The test vehicle gear configurations were used for the EverFE finite element analysis. After careful consideration of all current experimental parameters, as well as previous testing at the NAPTF, a wheel load level of 50,000 lbs was selected for the failure loading.

3.4.5.2 Progress of Loading.

Loading of the pavement test sections proceeded at a 50,000-lb wheel load level from August to November of 2006. As planned, the north test items were loaded with the triple dual tandem, and the south test items with the dual tandem gear configuration. Loading continued until each section developed an approximate structural condition index of 20, which was further deterioration than originally planned. However, the pattern of cracking and predominance of low-severity cracking made it likely that valuable information would be obtained by continuing the loading. The load passes applied to each test item are summarized in table 25.

3.4.5.3 Instrumentation Responses to Loading.

The dynamic responses of the instrumentation to loading were collected with each load pass, and the strain gages were monitored regularly for selected passes. The monitoring of these responses sometimes showed a change in magnitude or pattern of response prior to any observed distress. However, the strain gage responses and dynamic responses of the LPTs were primarily used for analysis after the conclusion of the testing.

3.5 DISTRESS SURVEYS.

3.5.1 Manual Distress Surveys.

Distress surveys were conducted prior to the load testing, and at regular intervals throughout the experiment. The initial post-construction surveys showed small cracks above the dowel bars in N3 and S3. Although some concern was considered about the possibility of these cracks extending during loading, minimal if any propagation occurred. These cracks are indicated on the distress maps, but were not considered in analysis.

Most of the distress surveys were conducted by contracted personnel of the FAA, with periodic verification by the QES project team. The manual distress surveys were very detailed. Prior to the surveys, the pavement was carefully swept. When possible, the surveys were conducted when the pavement surface was still minimally damp from the watering. As needed, the surveys were augmented with wire brushes, chalk markings, flashlights and other tools needed to ascertain the presence and pattern of very fine cracks. Due to the relatively stable indoor environment, most of the cracks remained very tight, increasing the survey difficulty. All distresses were measured and carefully mapped.

TABLE 24. AS-BUILT LIFE PREDICTIONS

Analysis Procedure	Dual Tandem B-767 300ER Wheel Load (lbs)			Triple Dual Tandem B-777 300 Wheel Load (lbs)			Dual Tandem B-767 300ER Wheel Load (lbs)			Triple Dual Tandem B-777 300 Wheel Load (lbs)			Dual Tandem B-767 300ER Wheel Load (lbs)			Triple Dual Tandem B-777 300 Wheel Load (lbs)		
	40,000	50,000	60,000	40,000	50,000	60,000	40,000	50,000	60,000	40,000	50,000	60,000	40,000	50,000	60,000	40,000	50,000	60,000
	N1 and S1 (8.63-in PCC/6.32 in-PCC/5.66-in aggregate base)						N2 and S2 (7.38-in PCC/7.51-in. PCC/5.60-in aggregate base)						N3 and S3 (5.67-in PCC/9.78-in PCC/4.75-aggregate base)					
	Stress (psi)																	
LEDFAA	465	557	639	466	554	642	502	617	734	486	579	709	524	644	774	509	645	745
FEDFAA (OL)	473	555	634	484	562	629	461	548	622	479	551	623	439	522	585	451	529	573
FEDFAA (Slab)	303	361	418	302	357	407	368	412	477	367	434	465	328	367	424	346	387	442
FAArfield (OL)	473	555	634	484	562	629	471	559	649	489	576	652	499	598	705	488	604	690
FAArfield (Slab)	303	361	418	302	357	407	346	385	414	346	382	405	268	289	300	308	316	329
EverFE	586	734	883	525	657	789	554	694	833	498	623	749	393	492	591	349	437	524
EverFE	722	897	1,083	753	940	1,128	636	795	954	644	805	966	531	664	797	500	625	751
Mod Westergaard (OL)	455	568	681	590	737	884	406	506	607	524	655	785	266	332	398	347	434	521
Mod Westergaard (slab)	334	416	499	432	540	647	413	515	617	533	666	799	459	573	686	599	749	898
	Design Passes																	
LEDFAA	4200	700	200	25900	3800	800	7000	1400	500	45900	6700	1900	9300	1600	500	62100	7900	1900
FEDFAA	1900	300	100	1700	300	100	2600	400	100	2000	400	100	10200	1300	300	8300	1300	400
FAArfield	1900	300	100	1700	300	100	2300	300	100	1900	300	100	3700	400	100	3700	500	100

TABLE 25. CUMULATIVE LOAD PASSES FOR TESTING DATES

Date	Test Item					
	North 1	South 1	North 2	South 2	North 3	South 3
7/25	132	132	132	132	132	132
7/26	528	528	528	528	528	528
7/27	924	924	924	924	924	924
7/28	1188	1188	1188	1188	1188	1188
7/31	1782	1782	1782	1782	1782	1782
8/1	2046	2046	2046	2046	2046	2046
8/2	2244	2244	2244	2244	2244	2244
8/3	2574	2706	2574	2706	2574	2706
8/4	2574	3168	2574	3168	2574	3168
8/7	2574	3432	2574	3432	2574	3432
8/9	2574	3894	2574	3894	2574	3894
8/10	2772	4356	2772	4356	2772	4356
8/11	3234	4818	3234	4818	3234	4818
8/24	3234	4950	3234	4950	3234	4950
8/25	3234	5016	3234	5016	3234	5016
9/14	3744	5016	3744	5016	3744	5016
9/15	3744	5526	3744	5526	3744	5526
9/18	4024	5806	4024	5806	4024	5806
9/19	4552	6334	4552	6334	4552	6334
9/20	5146	6928	5146	6928	5146	6928
9/21		7588		7588		7588
9/22		8116		8116		8116
9/25		8776		8776		8776
9/26		9370		9370		9370
9/27		9766		9766		9766
9/28		10426		10426		10426
9/29		11020		11020		11020
10/2		11614		11614		11614
10/3		12142		12142		12142
10/11				12538		
10/12				13132		
10/13				13594		
10/16				14056		
10/17				14270		
10/26				14337		
10/30				15509		
10/31				16567		

Cumulative plots of the manual distress surveys on the overlay test items are provided in figure 36, figure 37 and figure 38. The individual cracks are numbered in the order in which they first appeared. The distresses are also color-coded to twenty separate dates of visual distress survey on which new distresses were observed.

The initial and predominant pattern of observed distress was longitudinal cracking. Although loading was continued, only minimal transverse and diagonal connecting cracks were formed.

3.5.2 Digital Imaging.

Digital imaging was not used as a primary distress collection mechanism. However, the pavement surface was imaged on several occasions at different levels of distress development. These images provide a permanent record of the cracking patterns, in the event of possible future questions or issues.

Figure 39 is an example of several digital images "stitched" together. This image represents imaging with the equipment set up such that a 0.5-mm dimension is the size of a single pixel. Images were also recorded of the pavement with a camera height such that a 0.3-mm dimension is one pixel size.

3.5.3 Structural Condition Index (SCI) Calculations for Overlay.

For each distress survey, a structural condition index was computed for each test item. The structural condition indices decreased in an incremental manner, due to the limited number of slabs in each test item. For calculation of the SCI, the matched and unmatched joints were not considered separately. The distresses considered in the calculation of SCI are longitudinal, transverse and diagonal cracking; corner breaks; intersecting cracks and shattered slabs; and shrinkage cracking. The standard distress definitions in accordance with ASTM D5340 (2004) were used to calculate SCI values.

Since the calculation of SCI is an iterative procedure, and requires the look-up of deduct values, a spreadsheet macro was developed to speed the process and to ensure consistency. All SCI calculations were independently performed by at least two members of the project team. A summary of the SCI values over the course of the experiment is provided in table 26.

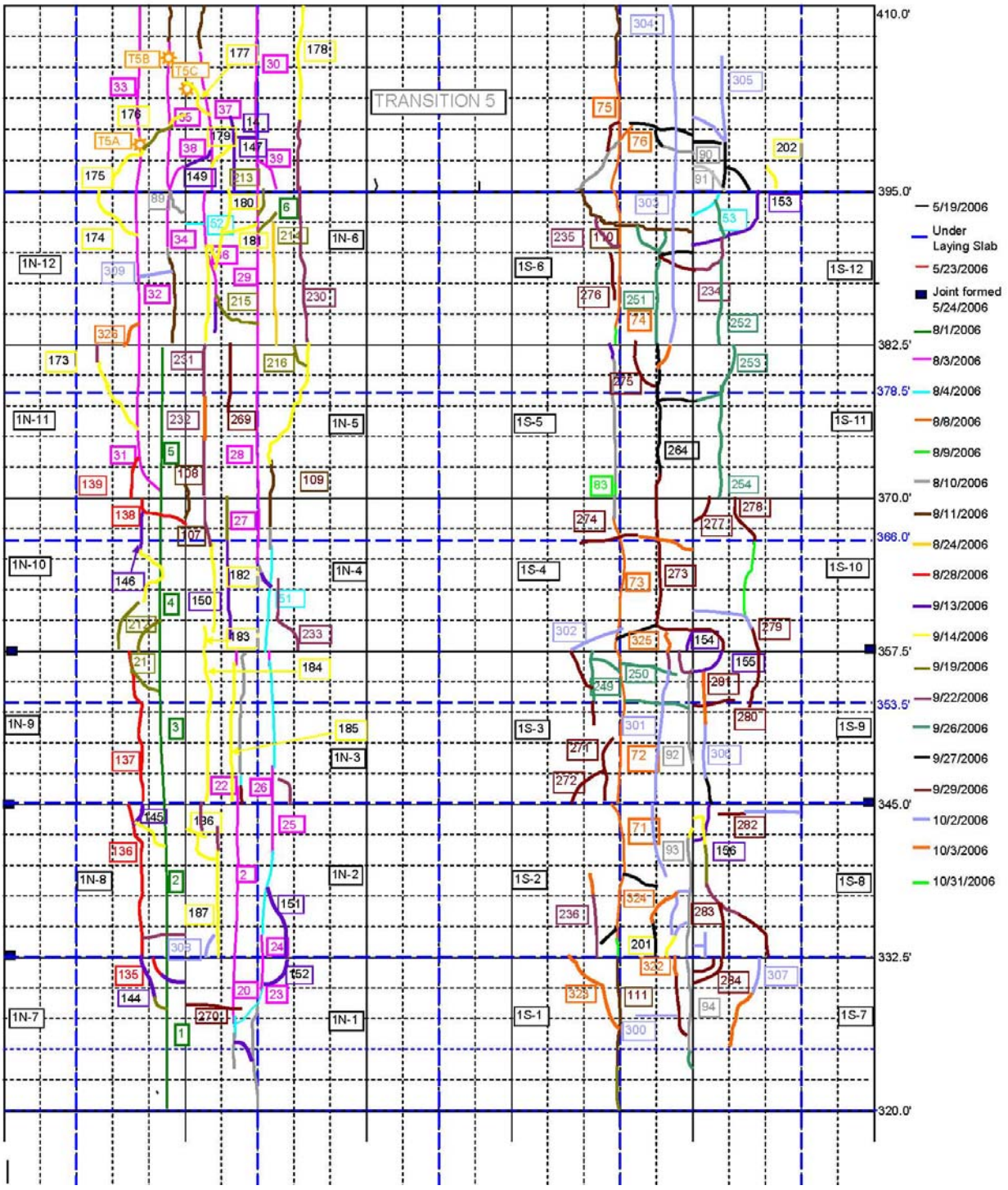

FIGURE 36. DISTRESS SURVEY ON OVERLAY AFTER FINAL LOADING FOR TEST ITEMS N1 AND S1

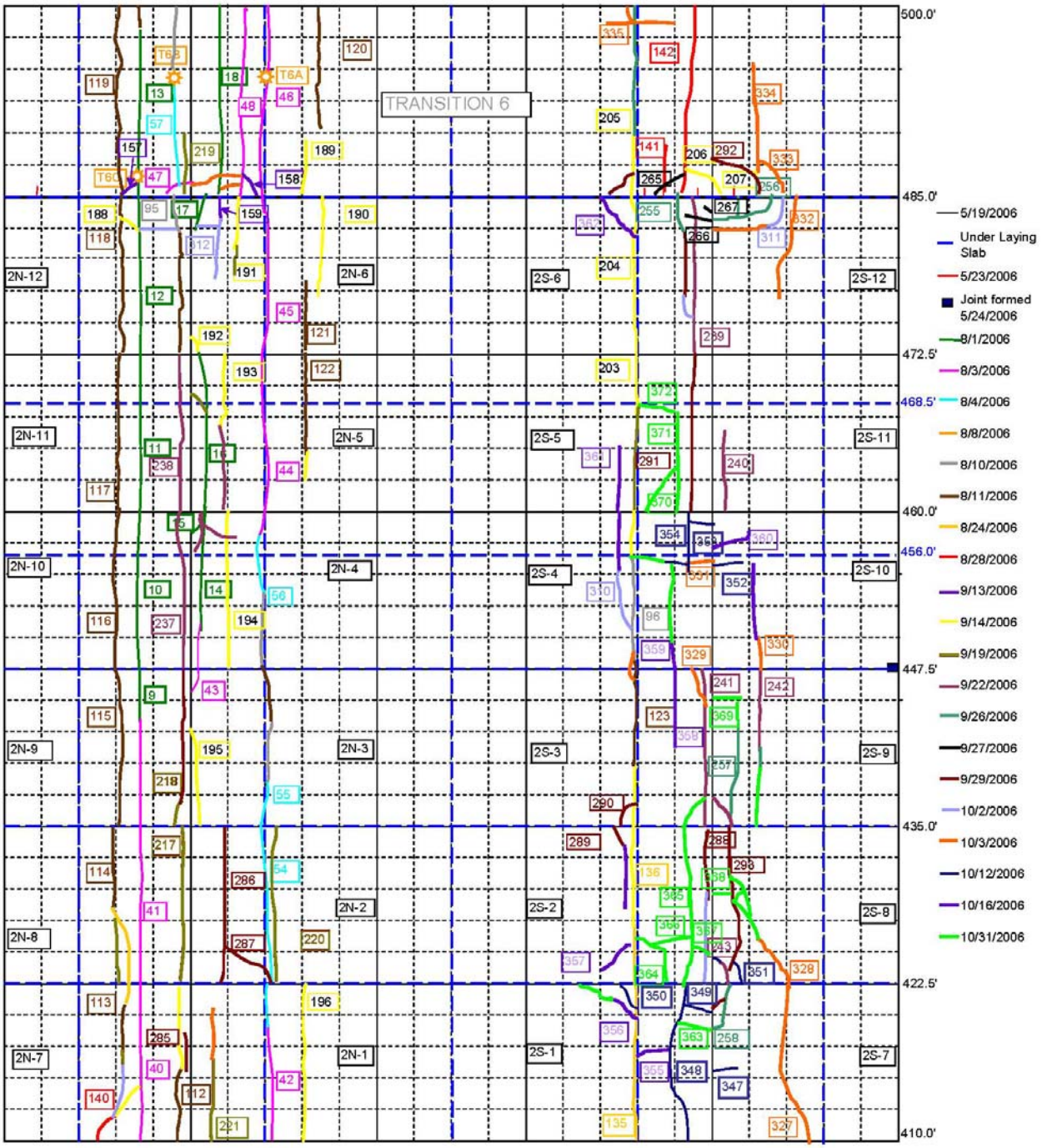

FIGURE 37. DISTRESS SURVEY ON OVERLAY AFTER FINAL LOADING FOR TEST ITEMS N2 AND S2

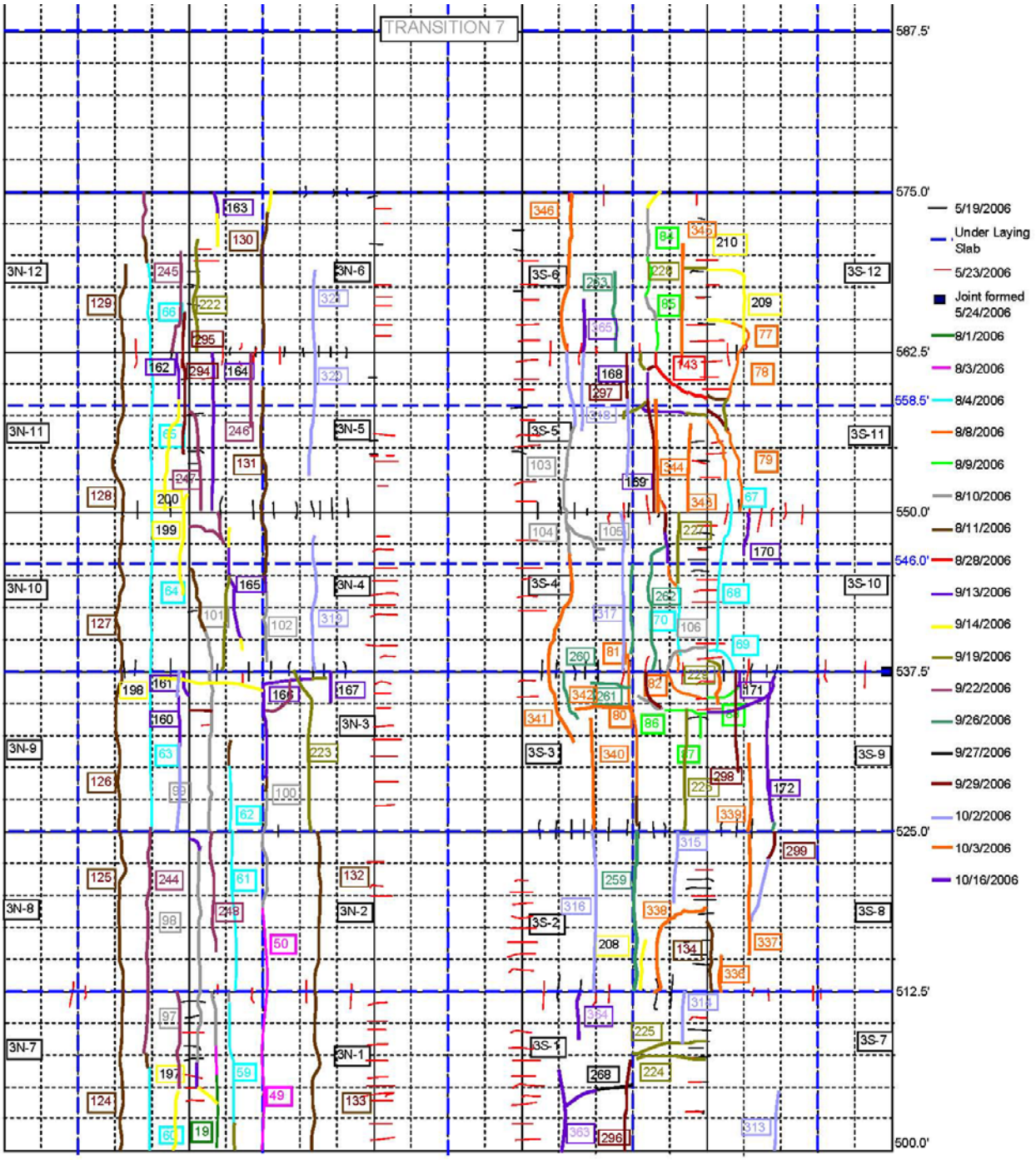

FIGURE 38. DISTRESS SURVEY ON OVERLAY AFTER FINAL LOADING FOR TEST ITEMS N3 AND S3

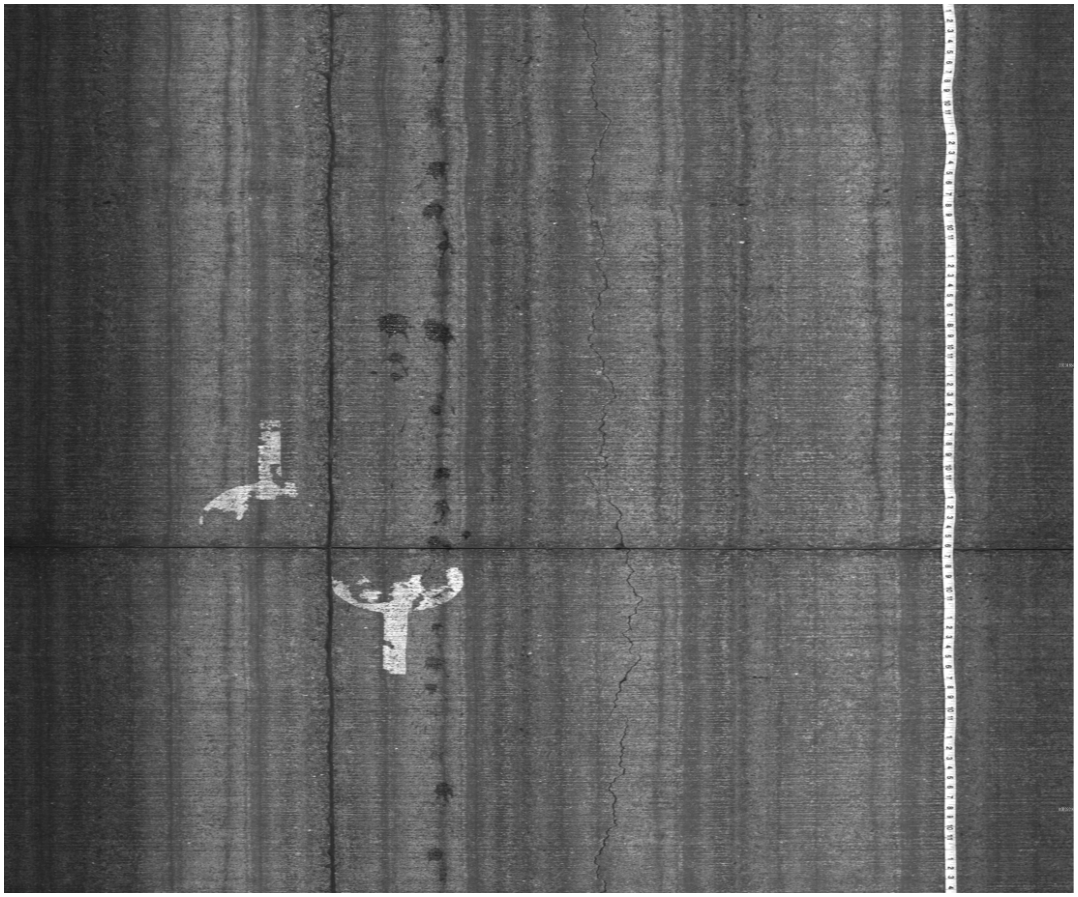

FIGURE 39. DIGITAL IMAGE OF SURFACE AND DISTRESS

TABLE 26. OVERLAY SCI VALUES FOR TEST ITEMS

Date	N1		S1		N2		S2		N3		S3	
	SCI	**Passes**	**SCI**	**Passes**	**SCI**	**Passes**	**SCI**	**Passes**	**SCI**	**Passes**	**SCI**	**Passes**
8/1/2006	100	2046	100	2046	100	2046	100	2046	100	2046	100	2046
8/3/2006	80	2456	100	2456	74	2456	100	2456	99	2456	100	2456
8/4/2006	73	2574	93	3168	67	2574	100	3168	91	2574	86	3168
8/8/2006	73	2574	85	3432	67	2574	100	3432	75	2574	75	3432
8/9/2006	73	2574	78	3762	67	2574	100	3762	75	2574	70	3762
8/10/2006	73	2772	76	4356	67	2772	99	4356	75	2772	64	4356
8/11/2006	68	3234	67	4818	60	3234	98	4818	74	3234	55	4818
8/24/2006	63	3234	67	4818	54	3234	90	4818	57	3234	55	4818
8/28/2006	57	3234	67	5016	54	3234	90	5016	57	3234	52	5016
9/13/2006	46	3234	54	5016	54	3234	90	5016	57	3234	48	5016
9/14/2006	39	3742	51	5524	45	3742	80	5524	51	3742	41	5524
9/19/2006	31	4088	50	5870	38	4088	79	5870	44	4088	35	5870
9/22/2006	24	5146	46	8116	27	5146	76	8116	32	5146	35	8116
9/26/2006	19	5146	32	9370	27	5146	64	9370	29	5146	28	9370
9/29/2006	19	5146	22	11020	24	5146	48	11020	29	5146	28	11020
10/2/2006	16	5146	16	11614	21	5146	48	11614	29	5146	24	11614
10/3/2006	14	5146	7	12142	21	5146	40	12142	29	5146	15	12142
10/12/2006	12	5146	7	12142	21	5146	29	13132	29	5146	15	12142
10/16/2006	12	5146	7	12142	21	5146	20	14056	29	5146	15	12142
10/31/2006	12	5146	7	12142	21	5146	17	16567	29	5146	15	12142

3.6 CORING.

When the initial cracks appeared in test items N1 and N2, it appeared from the location of the cracks that both top-down and bottom-up cracks were forming. To investigate, a limited number of cores were taken in the transition section, as labeled with small stars on the distress surveys. These cores were taken near the end of suspected top-down cracks, and just past the surface end of suspected bottom-up cracks. Cores were obtained that were only partially cracked through for both cases. Thus, the cores verified the apparent mode of cracking for those areas. For example, figure 40 shows a core taken through a bottom-up crack. The core location is marked with a small star and labeled T5C in figure 36.

More extensive coring directly from the test items was performed after the conclusion of loading of the overlay. Cores were taken for further crack investigations, and additional cores for possible supplemental materials testing.

FIGURE 40. CORE FROM TRANSITION 5 SHOWING BOTTOM-UP CRACK THAT HAS NOT PROPAGATED TO THE SURFACE

3.7 OVERLAY SLAB REMOVAL.

The overlay slabs were removed by an independent contractor, under contract to the FAA, and as supervised by FAA personnel. The top slabs were removed from the end of November until mid-December, 2006. The slabs were sawed, and pieces carefully removed to avoid any damage to the underlying slabs.

3.7.1 Observations During Overlay Slab Removal.

Observations of overlay slab removal were made on November 30 and December 14, 2006. On November 30, removal of selected slabs in test items N1, S1, N2 and S2 was undertaken; on December 14, selected slabs were removed from N3 and S3. In all test items, the asphalt interlayer was well bonded to the overlay slab, and almost always was removed intact with the overlay, as shown in figure 41. The bond breaking material used to separate the underlying slab from the asphalt so that the underlay slab cracking could be inspected following removal performed as intended.

FIGURE 41. OVERLAY SLAB REMOVAL WITH ASPHALT INTERLAYER ADHERED AND VISIBLE TOP-DOWN CRACK

3.7.1.1 Test Item North 1.

In test item N1, adjacent overlay slabs 3 and 9 were removed for the purpose of observing the corresponding distresses in the overlay and underlay. As identified in the distress surveys,

longitudinal cracking was the primary distress mode in this test item. The earliest longitudinal crack identified by the distress surveys coincided with the location of the lower support on the bottom of the chair supporting the dowels for the longitudinal joint. The other cracks observed in the top slab were determined to be formed from the top down. In many cases, the cracks were not formed through the full depth of the slab. Additionally, as the slabs were lifted, bending under their own weight clearly showed cracking only at the top of the slab, as seen, for example in the photographs in figure 41 and figure 42.

FIGURE 42. TOP-DOWN CRACK VISIBLE AS OVERLAY SLAB BENDS DURING REMOVAL

Consideration of the location of the cracks developed in the top slab relative to those evident in the bottom slab provides interesting insight into the relationship of the two slabs with respect to how they act together in carrying the load. The sketch in figure 43 shows the relative location of cracks in the two slabs; the slabs are also shown in the photograph in figure 44. Generally, cracks were slightly over two feet on either side of the longitudinal joint in the top slab. A series of five longitudinal cracks in the top slab were offset from the cracks and joints in the bottom slab. One of these occurred 11 inches outside the longitudinal joint, and the others were inside the joint.

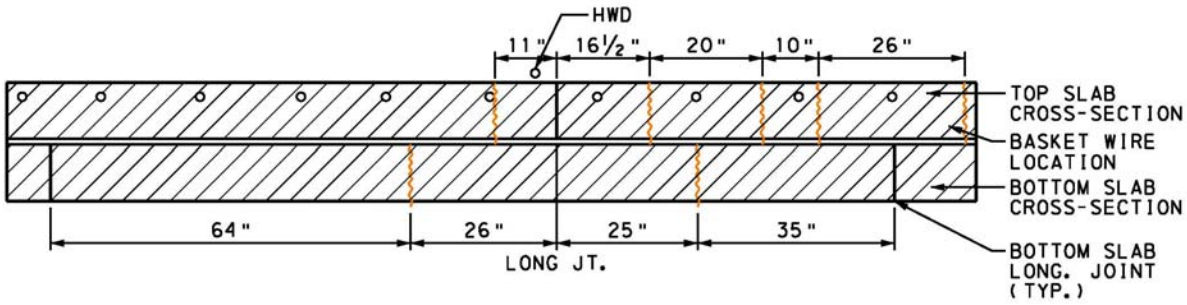

FIGURE 43. CRACK PATTERNS OBSERVED DURING OVERLAY REMOVAL, SLABS 3 AND 9 IN TEST ITEM N1

FIGURE 44. CRACKS OFFSET FROM LONGITUDINAL JOINT IN TEST ITEM N1

3.7.1.2 Test Item North 2.

Portions of slabs 3 and 9 in test item N2 were removed for inspection. A longitudinal crack existed two feet outside the longitudinal joint in the top slab. This relationship from top to bottom slab distress is similar to that identified in test item N1, but considerably less distress had formed. As also observed in test item N1, cracking in the overlay and underlay slabs was offset, as shown in figure 45.

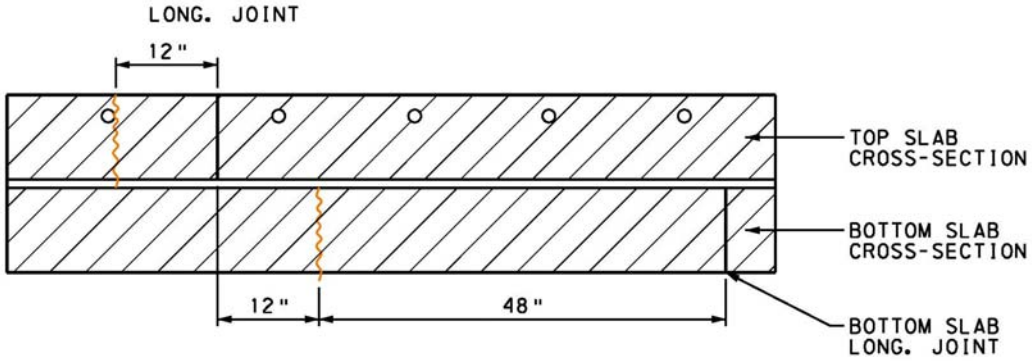

FIGURE 45. CRACK PATTERNS OBSERVED DURING OVERLAY REMOVAL, SLABS 3 AND 9 IN TEST ITEM N2

3.7.1.3 Test Item North 3.

No longitudinal cracking was observed in the underlay in test item N3. Two relatively short diagonal cracks existed in one location (approximately at station 515), perhaps as a result of joint restraint from joints which did not crack through the slab thickness.

3.7.1.4 Test Item South 1.

Portions of slabs 3 and 9 were removed for observation. Three longitudinal cracks were observed in the overlay slab and two in the underlay slab. In addition, a transverse crack was identified in the underlay slab emanating from the longitudinal joint in the underlay slab. The elevation and plan views of these crack locations are provided in figure 46. Again, the longitudinal cracks in the top slab were identified as emanating from the top down. In this case, one of the top slab cracks was 29 inches inside the longitudinal joint. The longitudinal joint in the bottom slab aligned with the top slab crack, and a second crack existed 8 inches inside the longitudinal joint in the top slab.

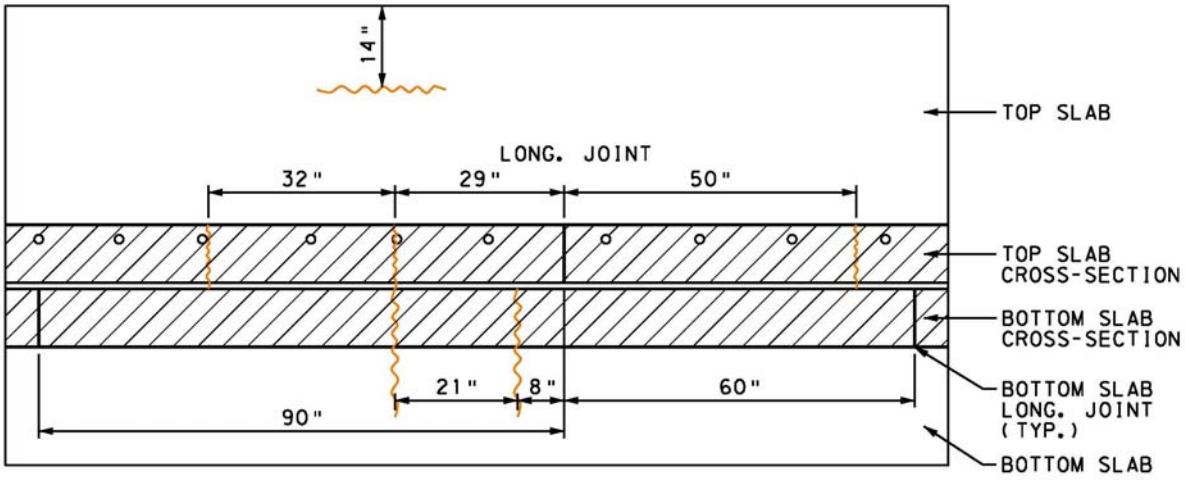

FIGURE 46. CRACK PATTERNS OBSERVED DURING OVERLAY REMOVAL, SLABS 9 AND 3 IN TEST ITEM S1

3.7.1.5 Test Item South 2.

Portions of slabs 3 and 9 were removed for inspection of the bottom slab. This area had four longitudinal cracks in the top slab which were more nearly aligned with those in the underlay slab than was observed in the other test items, as shown in figure 47. Two additional cracks, as shown to the right, also were observed in the top slab. The greatest number of load passes was applied to this test item. The bottom slab also had three diagonal cracks, interconnected with the longitudinal cracks.

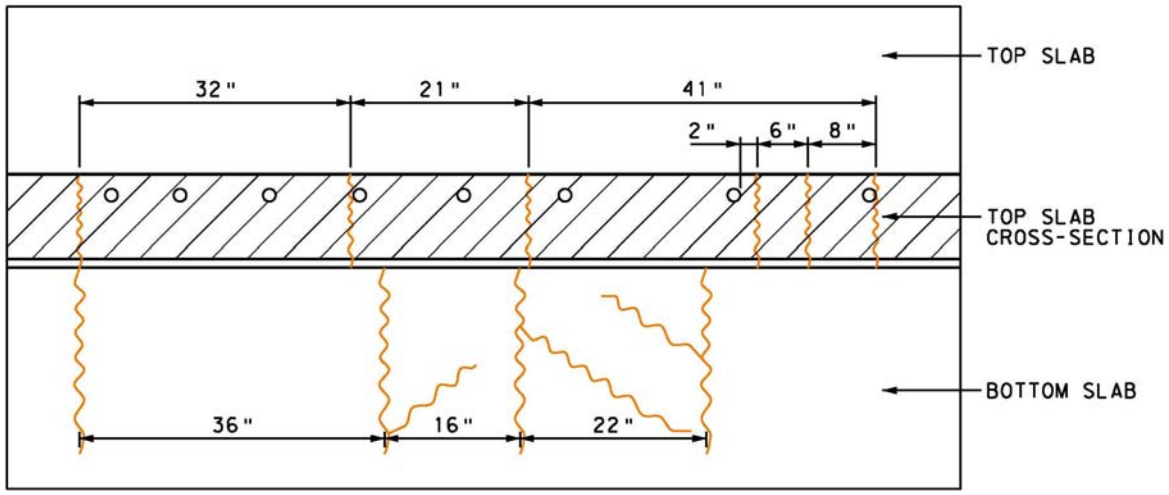

FIGURE 47. CRACK PATTERNS OBSERVED DURING OVERLAY REMOVAL, SLABS 9 AND 3 IN TEST ITEM S2

3.7.1.6 Test Item South 3.

No cracking was observed in the bottom slab within the removal area.

3.7.2 Distress Survey on Underlying Slabs.

After removal of the overlay slabs and interlayer, the underlay was carefully swept. On December 18, 2006, a detailed visual distress survey was completed on the underlay. The resulting distress maps are shown in figure 48, figure 49 and figure 50. The degree of deterioration in the underlay varied significantly between sections, although the final deterioration of the overlay slabs was similar.

The underlying slabs in test items N1 and S1 were observed to have the greatest degree of distress. In both test items, but especially in N1, the distress was concentrated in the slabs to the east end of the test items. This corresponded to the increase in deflections during HWD testing, and to the locations of greatest distress in the overlay. The underlay slabs in test items N1 and S1 were the thin underlay sections at a design thickness of 6 inches.

The underlying slabs in test item N2 were less distressed than those in S2, which had experienced the greatest number of passes on the overlay. The 7.5-inch underlay slabs in N2 and S2 were less distressed than the thinner underlay slabs in test items N1 and S1.

Finally, the 10-inch thick underlying slabs in test items N3 and S3 experienced minimal distress, although the overlay slabs had been significantly cracked. In test item S3, only a single corner break was observed.

3.7.3 SCI Calculations for Underlay.

SCI values were also computed for the underlays for each test item. Only the six larger slabs were considered. The smaller slabs on the outside of each test item were not considered; they were outside of the loaded area and experienced no visible distress. The underlay SCI values at the conclusion of the experiment are included in table 27.

TABLE 27. UNDERLAY SCI VALUES AFTER OVERLAY REMOVAL

Test Item	SCI
N1	32
S1	39
N2	57
S2	33
N3	87
S3	93

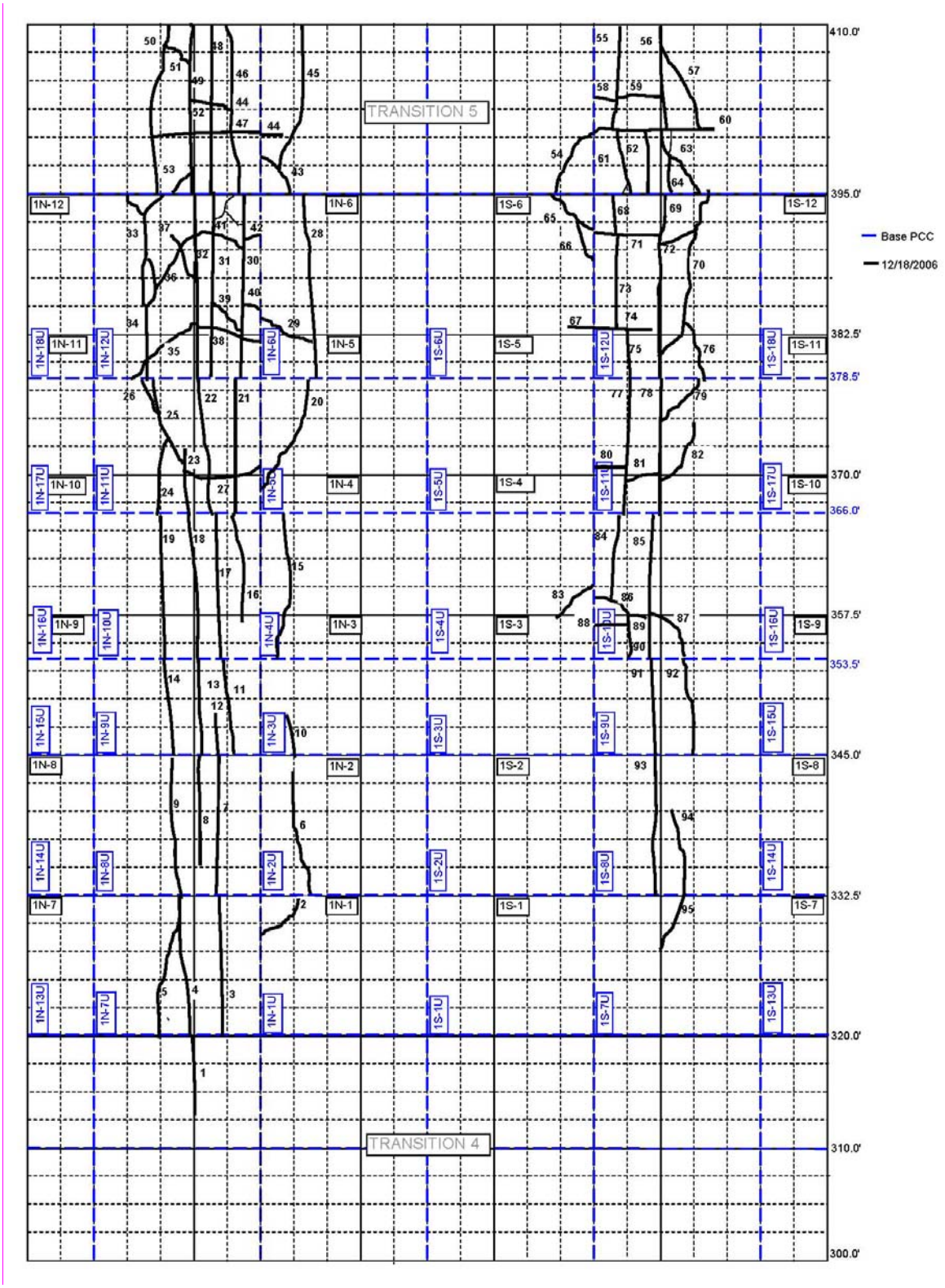

FIGURE 48. DISTRESS SURVEY ON BASE SLAB AFTER REMOVAL OF TOP SLAB FOR TEST ITEMS N1 AND S1

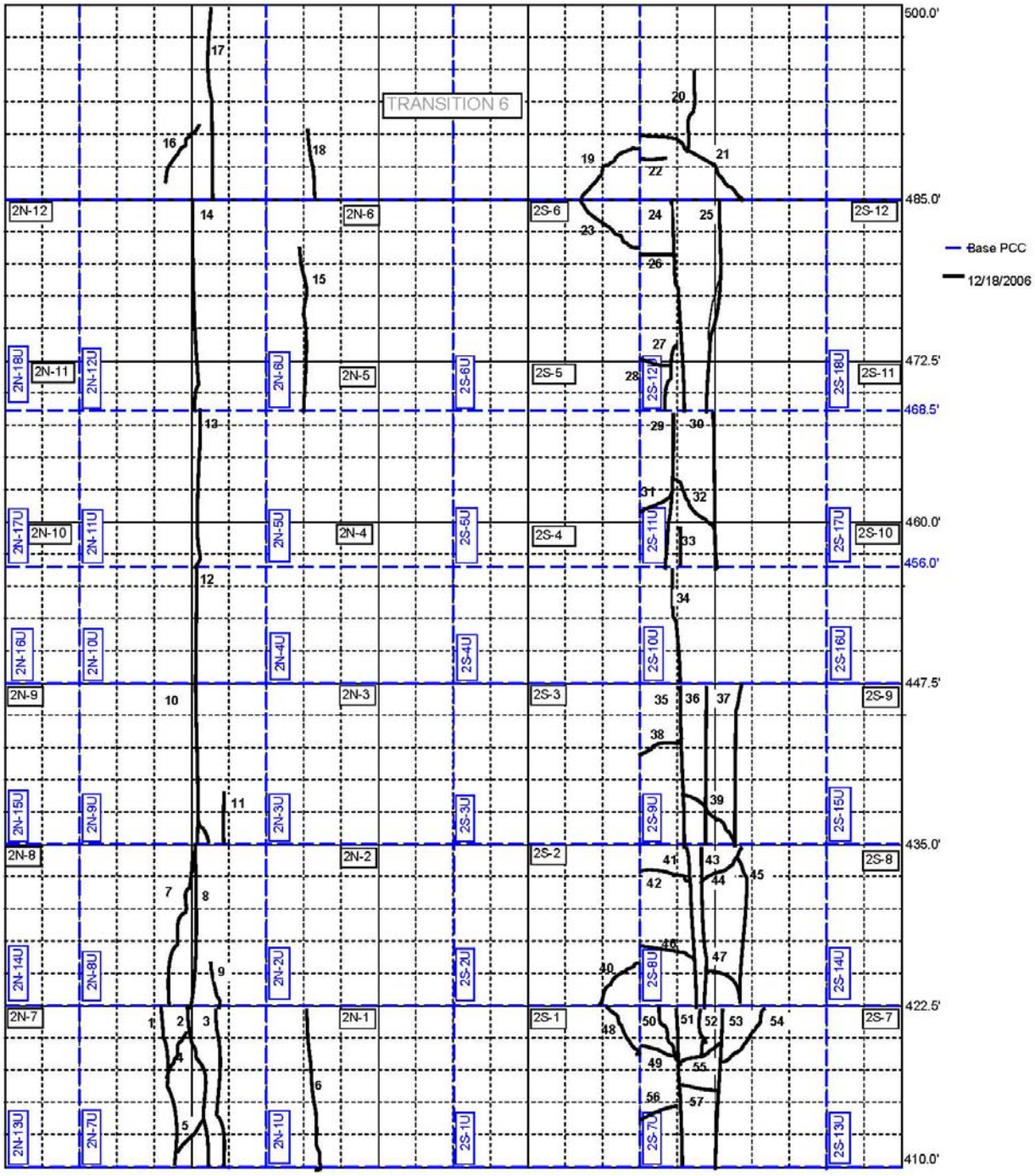

FIGURE 49. DISTRESS SURVEY ON UNDERLYING SLAB AFTER REMOVAL OF TOP SLAB FOR TEST ITEMS N2 AND S2

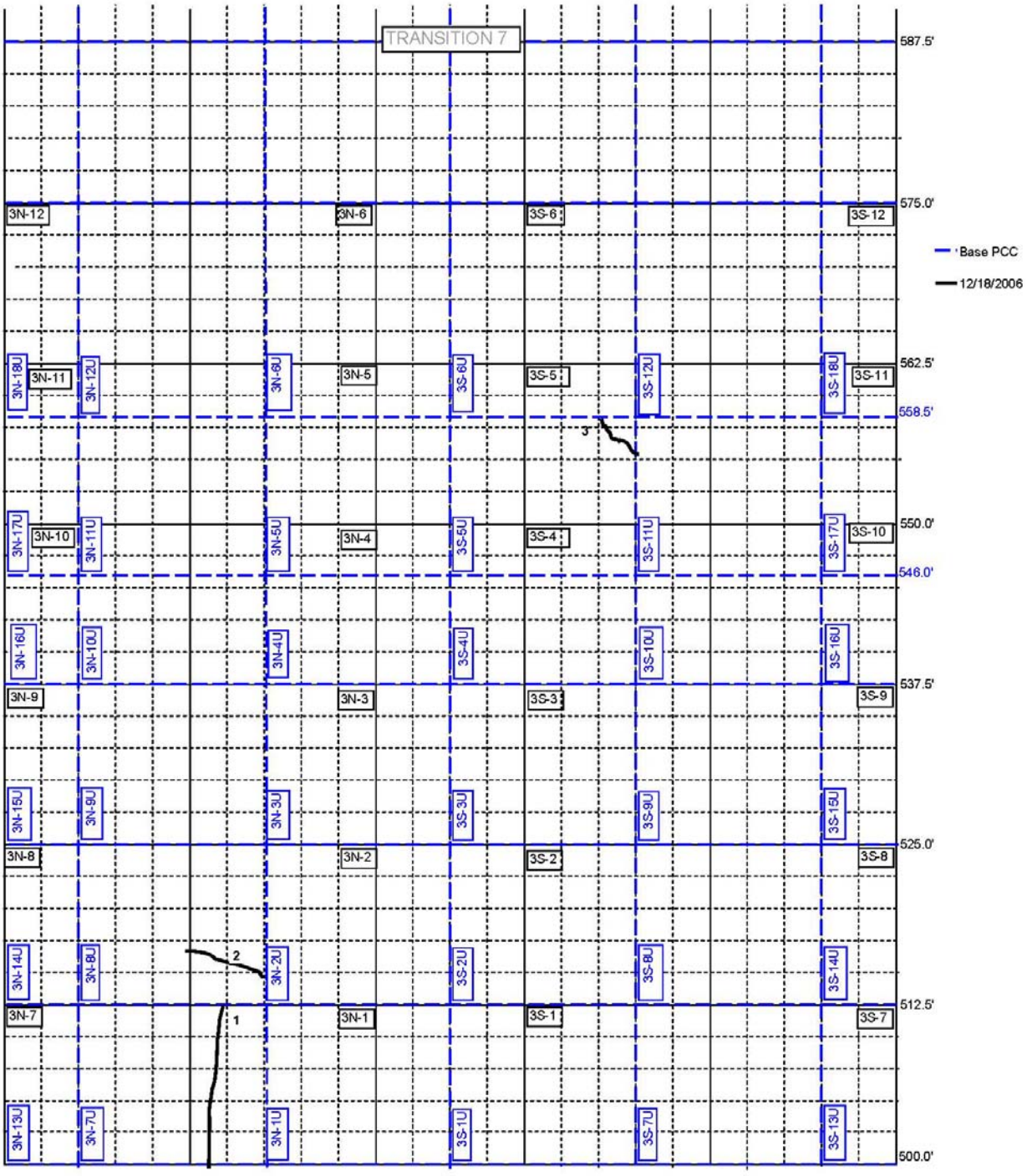

FIGURE 50. DISTRESS SURVEY ON UNDERLYING SLAB AFTER REMOVAL OF TOP SLAB FOR TEST ITEMS N3 AND S3

4. EXAMINATION AND ANALYSIS OF LOAD RESPONSES.

4.1 INSTRUMENTATION RESPONSES TO DYNAMIC LOADING.

4.1.1 Embedded Strain Gages.

4.1.1.1 Visual Examination of Response Plots.

The responses of the embedded strain gages to the applied loading were examined. The purposes of the examination were both to understand the pattern of response, and to identify the peak responses and tracks for quantitative data extraction. All embedded gages were installed in the longitudinal direction, parallel to the loaded longitudinal joint. The pattern of responses was initially examined by looking at the TenView plots for each gage for selected passes and wanders over the range of loading dates. On the TenView plots, downward peaks represent a tensile strain response.

Some typical responses of the embedded gages are shown in figure 51 through figure 62, representing the most common patterns. Figure 51 through figure 54 are for a set of gages in test item N1, loaded with the triple dual tandem gear configuration. These responses are from July 25, 2006 at the start of the failure loading before any distresses were observed. All four gages experienced a reversal of strain prior to and after the passage of the triple dual tandem gear. The strain was partially recovered between each axle. However, the total strain increased with each subsequent axle. This effect was least noted, in most locations, in the gage closest to the surface.

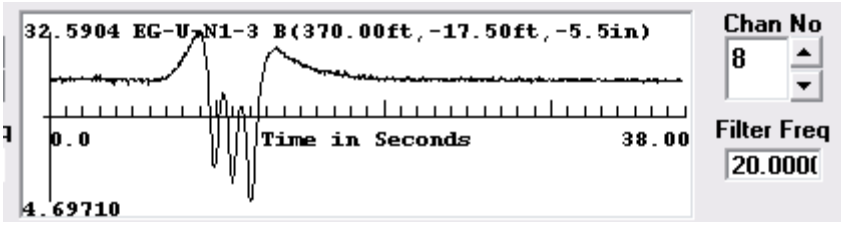

FIGURE 51. TEST ITEM N1, EMBEDDED STRAIN GAGE RESPONSE AT BOTTOM OF UNDERLAY, TRACK 0

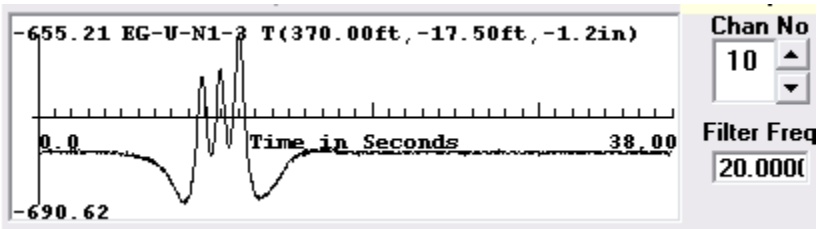

FIGURE 52. TEST ITEM N1, EMBEDDED STRAIN GAGE RESPONSE AT TOP OF UNDERLAY, TRACK 0

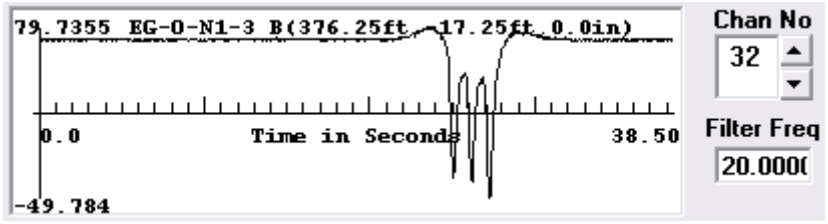

FIGURE 53. TEST ITEM N1, EMBEDDED STRAIN GAGE RESPONSE AT BOTTOM OF OVERLAY, TRACK 0

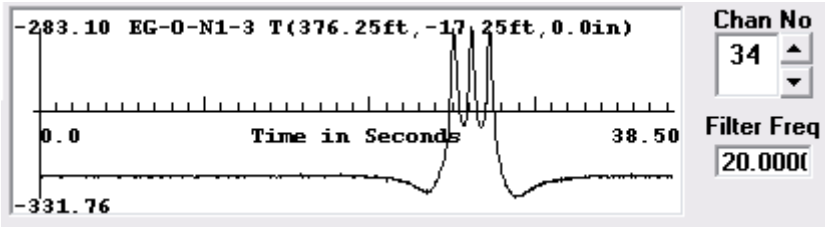

FIGURE 54. TEST ITEM N1, EMBEDDED STRAIN GAGE RESPONSE AT TOP OF OVERLAY, TRACK 0

Figure 55 through figure 58 illustrate responses for a set of gages in test item S1, which was loaded with the dual tandem gear configuration. The responses are also from July 25, 2006, and are similar with respect to the stress reversal prior to and after the passage of the gear and with respect to the increase in strain with the second axle. Again, the least increase in strain between axles is observed for the gage near the surface of the overlay.

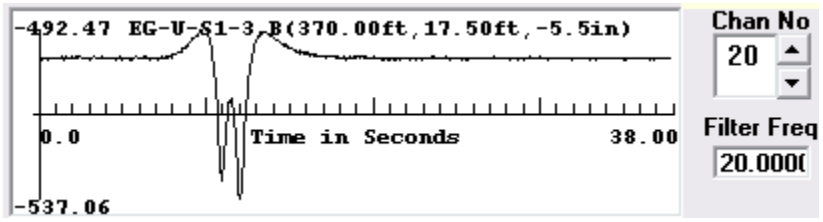

FIGURE 55. TEST ITEM S1, EMBEDDED STRAIN GAGE RESPONSE AT BOTTOM OF UNDERLAY, TRACK 0

FIGURE 56. TEST ITEM S1, EMBEDDED STRAIN GAGE RESPONSE AT TOP OF UNDERLAY, TRACK 0

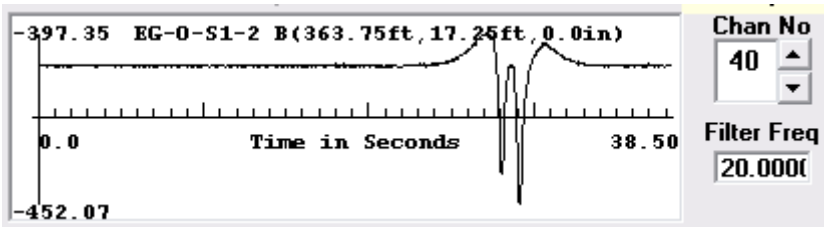

FIGURE 57. TEST ITEM S1, EMBEDDED STRAIN GAGE RESPONSE AT BOTTOM OF OVERLAY, TRACK 0

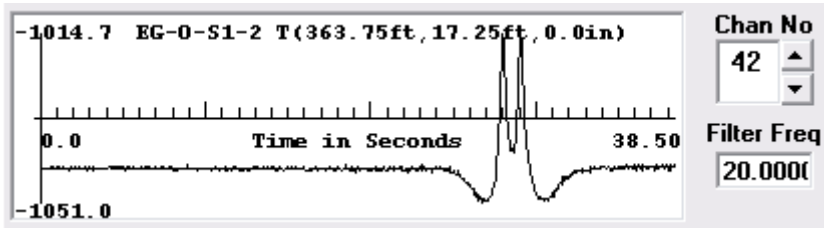

FIGURE 58. TEST ITEM S1, EMBEDDED STRAIN GAGE RESPONSE AT TOP OF OVERLAY, TRACK 0

Figure 59 and figure 60 illustrate the responses from underlay gages in test item N2 from August 3, 2006. On that date, these gages did not follow the pattern of steadily increasing strain with the passage of each axle. While the third axle typically produced the greatest strain, the second peak was less than the first. In figure 60, for the gage at the bottom of the underlay, strain reversal occurred between the peaks from each axle.

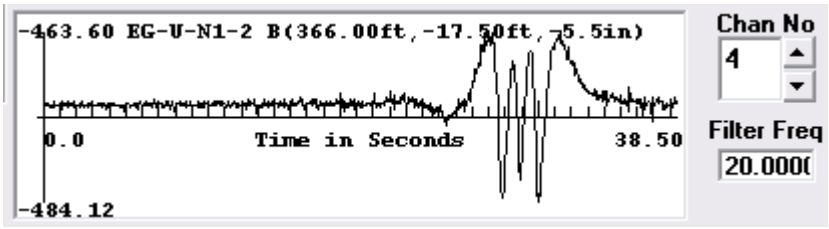

FIGURE 59. TEST ITEM N2, EMBEDDED STRAIN GAGE RESPONSE AT BOTTOM OF UNDERLAY, TRACK 0 (NOTE: GAGE IS MISIDENTIFIED IN TENVIEW; GAGE IS EG-U-N2-2 B)

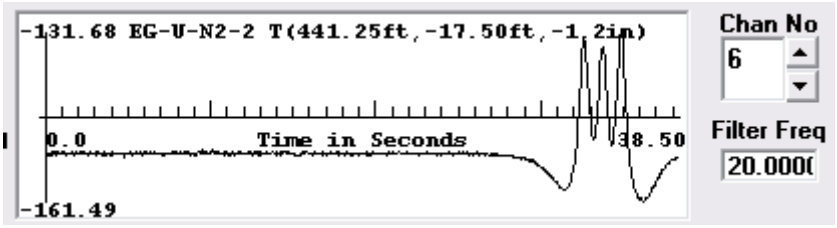

FIGURE 60. TEST ITEM N2, EMBEDDED STRAIN GAGE RESPONSE AT TOP OF UNDERLAY, TRACK 0

Figure 61 and figure 62 illustrate yet another pattern of strain response. These plots are for the 6-inch overlay in test item N3 on August 3, 2006. The lower gage showed almost equal peaks for each axle passage, with full recovery between. The gage near the surface of the overlay responded with slightly decreasing strain peaks with the passage of each subsequent axle.

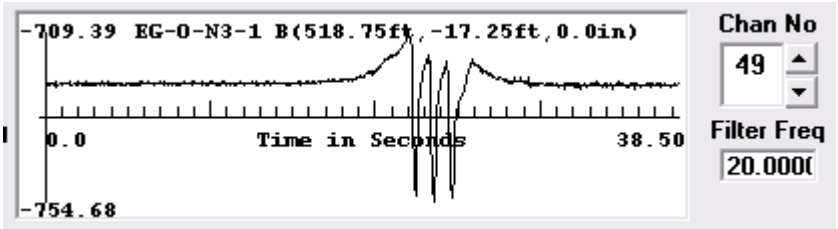

FIGURE 61. TEST ITEM N3, EMBEDDED STRAIN RESPONSE AT BOTTOM OF OVERLAY, TRACK 0

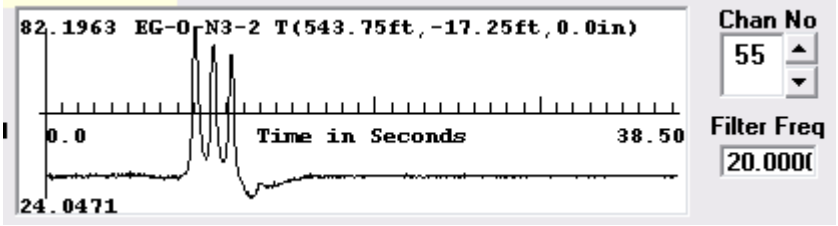

FIGURE 62. TEST ITEM N3, EMBEDDED STRAIN RESPONSE AT TOP OF OVERLAY, TRACK 0

While these plots illustrate the most common strain response patterns, as distresses increased in the pavement sections, the patterns of responses sometimes also changes. In addition, the response for two consecutive passes in a track (one eastbound, one westbound) sometimes differed by a small but consistent amount.

4.1.1.2 Extraction of Peak Responses.

Considering the patterns observed, as illustrated in figure 51 through figure 62, spreadsheet macros were developed for extracting the peak responses. For the purposes of comparing the peak responses over time, the peak strain response was defined as the greatest difference

between the baseline reading prior to the loading and the response during loading. The stress reversals were not considered in the extraction of peak strain responses.

Figure 63 and 64 contain example summary plots of peak strain. These examples are for test item S1, for the overlay and underlay gages, respectively, at gage location 3. These values were plotted for various numbers of prior cumulative passes of the test vehicle, corresponding approximately to the intervals of the visual distress surveys. Each plot contains lines for the gages near the top and the bottom of the slab, and for each loading track. The responses were determined by averaging selected passes in that track in a single wander. Appendix H contains the peak strain responses for all embedded strain gages. Both the magnitude and pattern of variation of response over time was different for gages at different locations within a single test item. The changes over time often corresponded to differences in distress patterns. For example, a decrease in strain response for a given track sometimes corresponded to the occurrence of a crack between that track and the gage location.

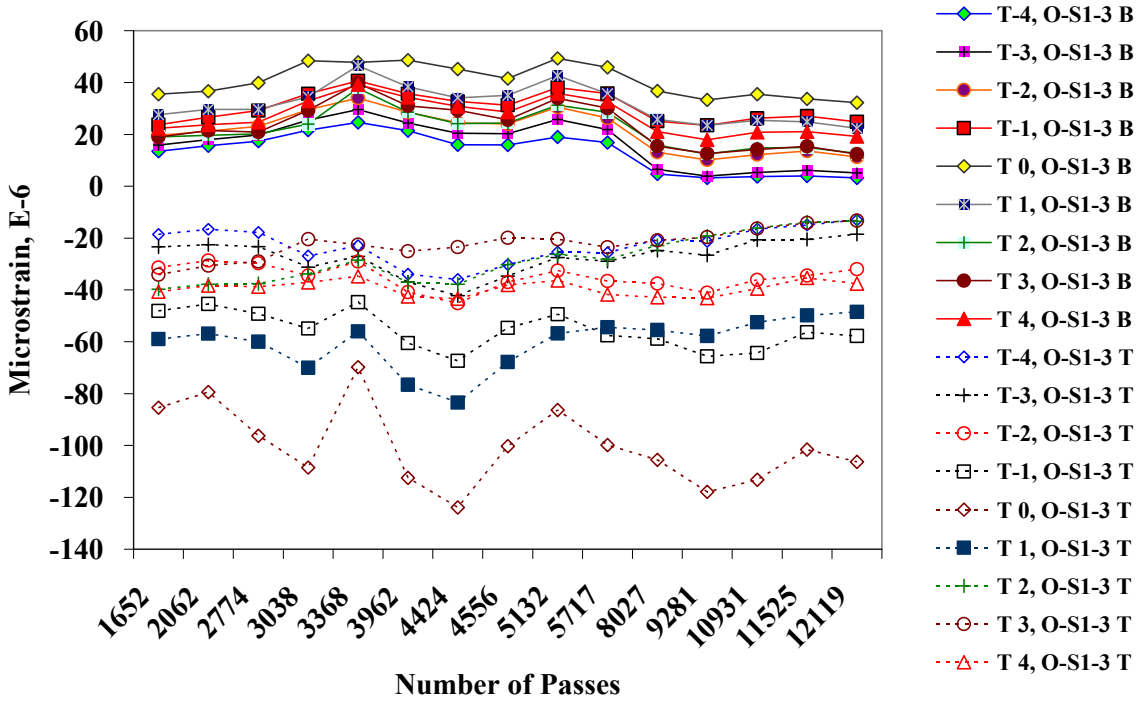

FIGURE 63. PEAK GAGE RESPONSES FOR TEST ITEM S1, OVERLAY STRAIN GAGES, LOCATION 3

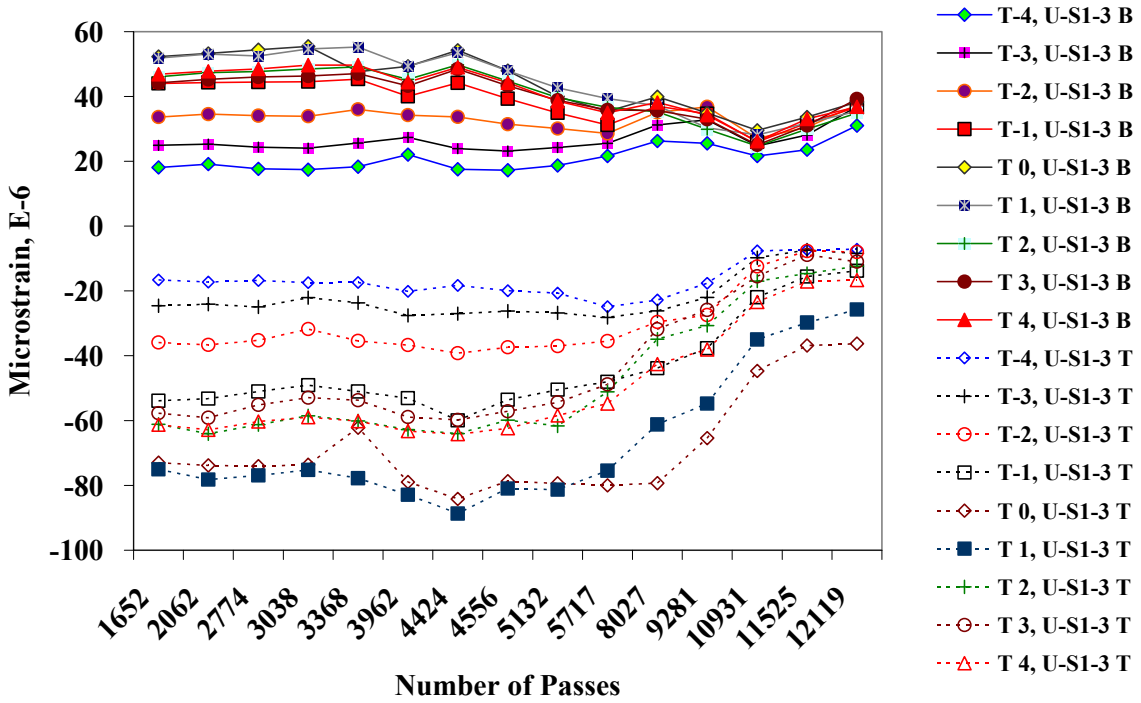

FIGURE 64. PEAK GAGE RESPONSES FOR TEST ITEM S1, UNDERLAY STRAIN GAGES, LOCATION 3

4.1.1.3 Strain History Explorations.

In addition to the systematic extraction of peak strain responses for selected intervals, strain history explorations were conducted. During ramp-up initial loading, a few strain gages (notably those in test items N1 and N2) were observed to have a gradual increase in peak strain values with the number of passes. These gage locations were in the general vicinity of the first observed cracking. Therefore, the date of observed cracking near each strain gage location was noted. Then the peak strain values were tracked back prior to that date at a greater frequency, to see if that type of gradual increase in strain, or other pattern of strain change, was observed that was obscured in the plots with a larger interval between extractions. For most gages, no such response change was found. An example plot from one of the strain history explorations is shown in figure 65.

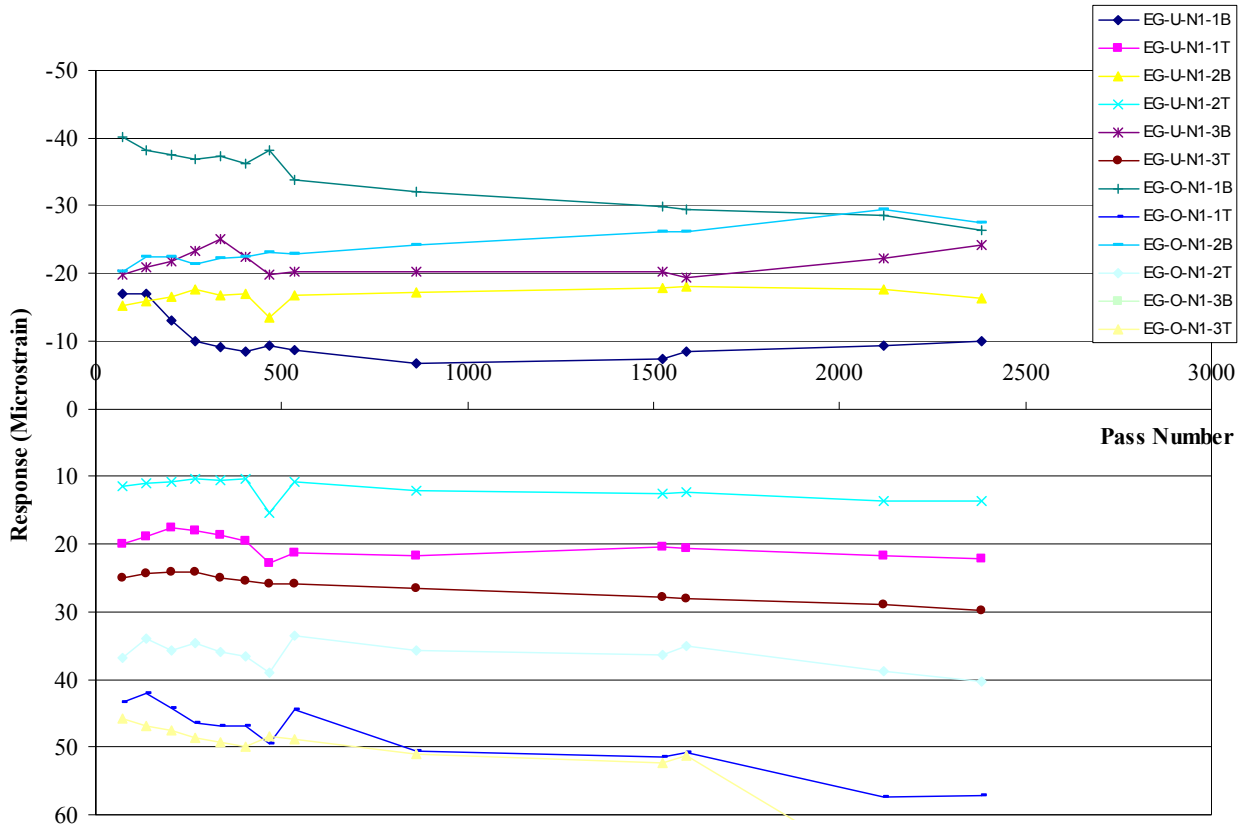

FIGURE 65. EXAMPLE OF STRAIN HISTORY EXPLORATION FOR TEST ITEM N1

4.1.2 Surface Strain Gages.

Although surface strain gages were installed after construction, only limited meaningful data was not obtained from those gages. The gages were not initially wired to the data acquisition boxes, and in some cases, there were not adequate or appropriate channels available. Therefore, data acquisition was planned for limited sampling times using a portable acquisition system. However, during sweeping and other operations, many of the gage wires were broken.

Nevertheless, data were successfully collected from some of the gages. The location and orientation of the gages made that data less valuable. The gages were installed in the longitudinal direction, whereas the major surface tensile stress would be expected in the transverse direction. In addition, since the gages could not be installed in the wheeltrack, it would have been desirable to have gages in a number of transverse positions so that the pattern of distress variation could be observed.

The surface gages were not emphasized in the initial instrumentation plan. The pattern of distress that was observed during the testing, however, has caused reconsideration of these gages for future experiments. Since the primary cracking was longitudinal and some of the cracks initiated at the surface, better installation procedures and locations for the surface gages should be planned.

4.1.3 Pressure Cells

Soil pressure cells were installed at the top of the aggregate base course in test items N1, N3 and S3. While the pressure cell in test item S3 provided reasonable responses on some dates, the readings were out of range for many intervals. For the soil pressure cells in the north test items, responses were extracted for each loading track. In general, the recorded responses were greatest where the gear configuration was approximately centered over the gage, rather than when a single wheel was over the gage. For the north test items, this position corresponded to track -3 for initial loading. Typical maximum pressure cell responses are shown in figure 66 and figure 67. Typical pressure cell responses for loading positions not directly over the gage are shown in figure 68 and figure 69. Figures 66 through figure 69 are from data collected on July 25, 2006. Maximum responses from the pressure cells over the period of loading are shown in figure 70.

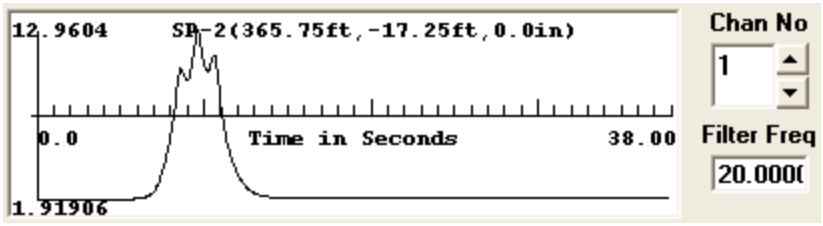

FIGURE 66. TEST ITEM N1, TYPICAL MAXIMUM PRESSURE CELL RESPONSE AT TOP OF AGGREGATE BASE COURSE, TRACK -3

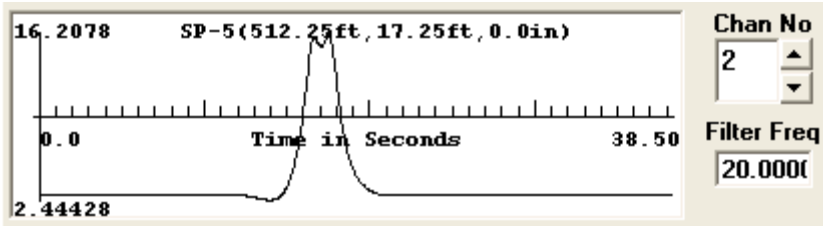

FIGURE 67. TEST ITEM S3, TYPICAL MAXIMUM PRESSURE CELL RESPONSE AT TOP OF AGGREGATE BASE COURSE, TRACK 3

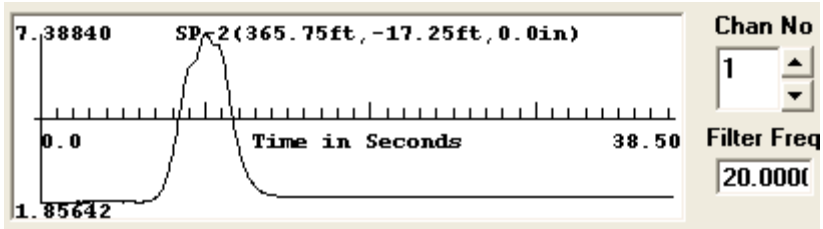

FIGURE 68. TEST ITEM N1, TYPICAL PRESSURE CELL RESPONSE AWAY FROM LOADING POSITION AT TOP OF AGGREGATE BASE COURSE, TRACK 4

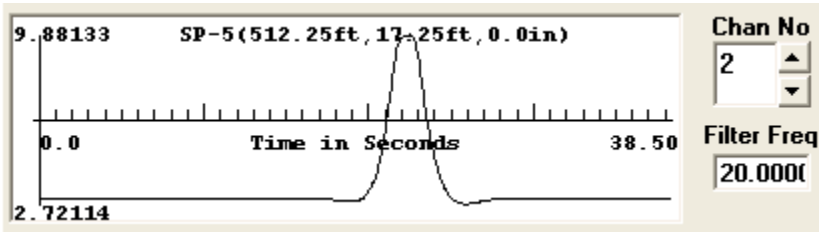

FIGURE 69. TEST ITEM S3, TYPICAL PRESSURE CELL RESPONSE AWAY FROM LOADING POSITION AT TOP OF AGGREGATE BASE COURSE, TRACK -4

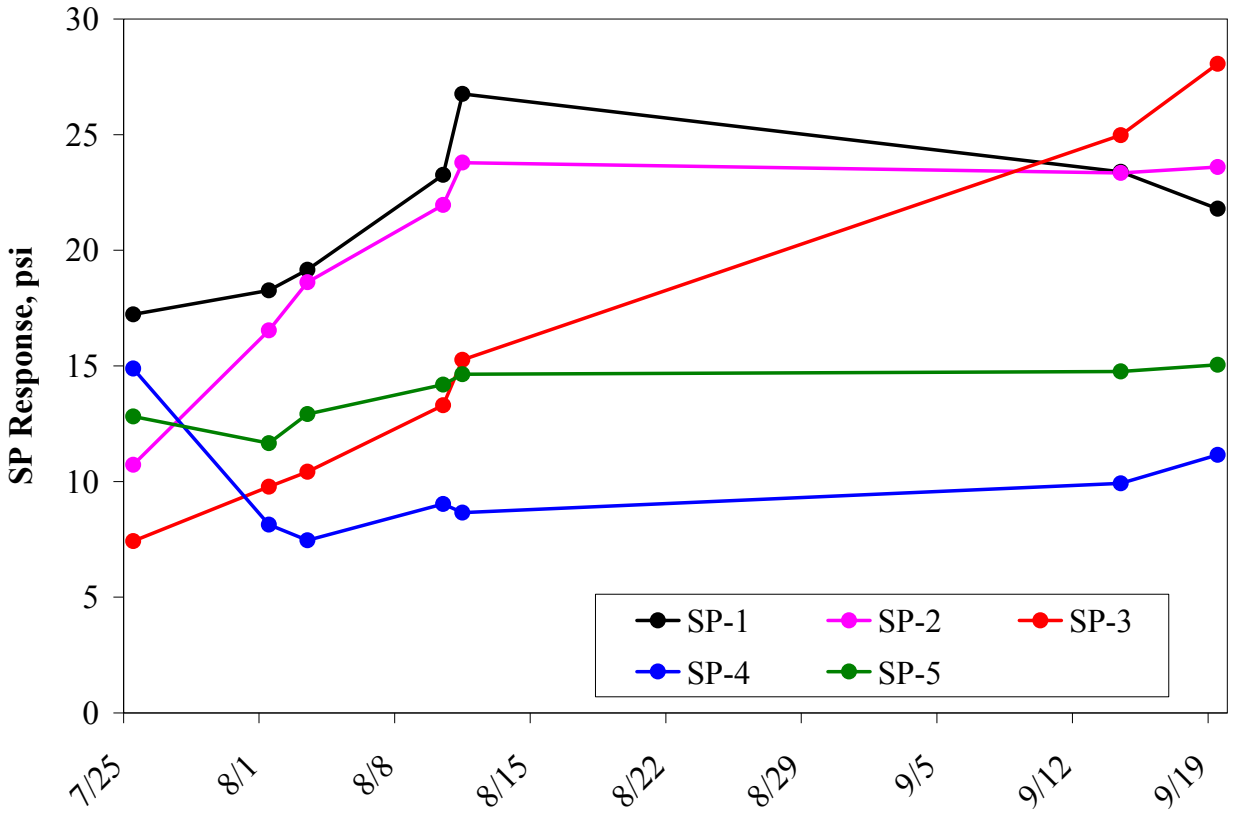

FIGURE 70. MAXIMUM PRESSURE CELL RESPONSE CHANGE WITH DATE DURING PERIOD OF LOADING

The pattern of variation of pressure cell response with loading track became much more variable as distress accumulated in the test items. The decreased distribution of stress to the subgrade could be observed as the thick overlay in test item N1 experienced cracking between the loading track and the pressure cell location.

The responses of the pressure cells in N1 and N3 to the triple dual tandem gear in track -3 are shown in figure 71. These responses are plotted versus test item SCI. The initial decrease in response for SP-4 in test item N3 has not been explained. The soil pressures in test item N3

steadily increased with decreasing SCI, although the responses of the two gages were significantly different. This difference was not logically correlated with matched and mismatched joints or other experimental parameters.

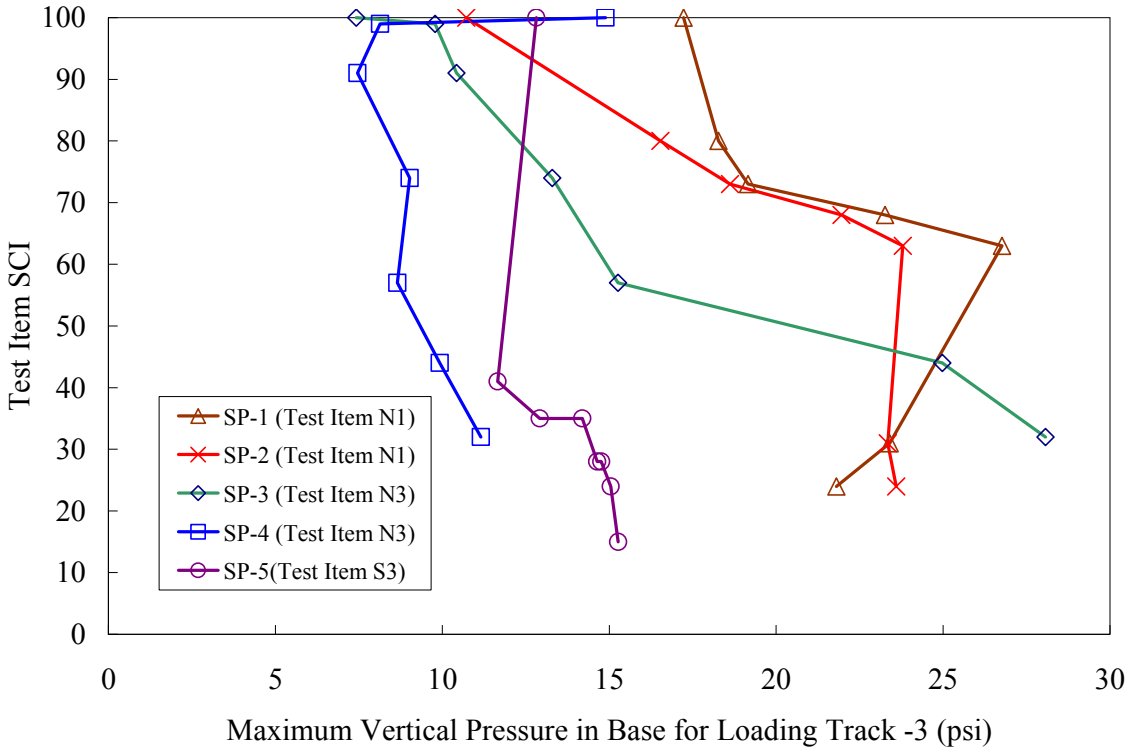

FIGURE 71. INCREASE IN RESPONSES OF BASE PRESSURE CELLS WITH DETERIORATION OF OVERLAY SLABS

The pressure cells in test item N1 were more consistent between the two gages. Both showed an increase in pressure until a SCI of about 60 was reached, and then the pressure declined for this track. The thin underlay slab in test item N1 deteriorated substantially before the conclusion of the loading, unlike the thick underlay slab in test item N3. It is postulated that at an overlay SCI of about 60, the underlay deterioration was significant enough to affect the distribution of the load to the subgrade. In test item N3, soil pressure cell SP-3 is located near a stack of LPTs. The responses of this pressure cell are discussed further in section 4.1.4.

4.1.4 Linear Potentiometers.

4.1.4.1 Stack of LPTs in Test Item 3.

Three LPTs and a soil pressure gage were installed on the north side of test item 3. LPTs O-N3-3 and O-N3-4 were installed in the overlay on either side of the joint in slabs N3-1 and N3-2, respectively. LPT U-N3-1 was installed in the underlay. The soil pressure gage SP-3 is installed at the top of the aggregate base course. This group of LPTs was studied with respect to two types of responses to loading. Both their immediate dynamic responses directly under the load and their longer term changes in position during loading periods were considered.

After the failure loading began on July 25, 2006, the LPTs moved significantly downward under loading and upward in ensuing rest periods. The total downward deflection accumulated during the loading phases is provided in table 28.

TABLE 28. DEFLECTION OF LPTS DURING LOADING

		Downward Deflection of LPTs, mils		
Loading Period	**Wanders**	**LPT-U-N3-1**	**LPT-O-N3-3**	**LPT-O-N3-4**
7/25/06 – 8/3/06	39	7.6	44.7	47.9
8/10/06 - 8/11/06	10	3.1	10.7	12.2
9/13/06 – 9/20/06	28.9	17.6	26.4	28.5

The first visible crack appeared on August 1. The longitudinal cracks which developed on August 3 and 4 divided the slab into three pieces. The longitudinal cracks which developed on August 10 and 11 divided the slab further, with cracks extending into the vicinity of the LPTs. With the progression of cracks and further loading, LPT-U-N3-1 exhibited increased downward deflection as the load was increasingly transferred to the underlay slab. The ratio of underlay LPT deflection to overlay LPT deflection was approximately 1:6 for the first loading phase, 1:4 for the second loading phase and 1:1.7 for the final loading phase. The LPTs exhibited upward movement during the period of no loading. The magnitude of upward movement during rest periods is provided in table 29.

TABLE 29. DEFLECTION OF LPTS BETWEEN LOADING PHASES

		LPT Movement, mils		
Rest Period	**Days**	**LPT-U-N3-1**	**LPT-O-N3-3**	**LPT-O-N3-4**
7/12/06 – 7/25/06	12	+0.3	+0.7	+1.1
8/3/06 -8/10/06	6	-3.0	-8.3	-7.2
8/11/06 - 9/13/06	32	-34.1	-34.0	-32.5
9/20/06-11/1/06	42	-33.4	-49.2	-42.5

As previously discussed, the soil pressure gage, SP-3, was expected to exhibit greater response amplitudes on track -3. The LPTs were expected to exhibit greater amplitudes on track 0, as the outside edge of the outside tire is at the longitudinal joint. The dynamic responses of the soil pressure gage, SP-3, are provided in table 30. The soil pressures from loading on track 0 were approximately 30 to 40 percent lower than the pressure from loading on track 3. The pressure on the gage generally increased as loading proceeded, with a few exceptions. The readings from SP-3 indicated an increase in soil pressure of three to four times from July 25, 2006 through September 20, 2006.

TABLE 30. MAXIMUM RESPONSES OF SOIL PRESSURE GAGE SP-3

	SP-3 Soil Pressure Gage (psi)				
Date	**First Pass of the day**	**First Pass on Track 0**	**First Pass on Track-3**	**Last Pass on Track-3**	**Last Pass on Track 0 of the day**
7/25/06	5.6	5.9	8.3	7.4	4.7
8/1/06	5.1	2.2	9.3	10.0	2.0
8/3/06	5.5	2.0	10.6	11.0	1.5
8/10/06	0.9	0.1	7.8	13.8	2.6
8/11/06	6.5	2.4	13.1	15.7	3.2
9/13/06	19.4	13.9	21.8	21.6	13.7
9/14/06	18.6	15.7	23.4	25.4	15.8
9/20/06	22.2	18.9	28.8	28.3	15.4

The dynamic responses from the underlay LPT are provided in table 31. The amplitude of responses in the underlay LPT increased from 4 mils to 11 mils as the loading on the pavement continued from July 25, 2006 through September 20, 2006. Figure 72 shows the increase in response amplitudes on the underlay LPT from the last loading pass of the day on track 0. This may be because more load transferred from the overlay slab to the underlay slab as the overlay distress increased with continuous loading. The difference in responses from loading on different tracks appeared to be insignificant.

TABLE 31. RESPONSES OF UNDERLYING SLAB LPT

	LPT-U-N3-1 (mils)				
Date	**First Pass of the day**	**First Pass on Track 0**	**First Pass on Track-3**	**Last Pass on Track-3**	**Last Pass on Track 0 of the day**
7/25/06	5.3	4.2	4.8	4.4	4.1
8/1/06	6.1	5.2	6.2	6.2	5.5
8/3/06	6.3	5.4	6.3	6.6	5.4
8/10/06	6.5	7.4	6.8	6.5	5.7
8/11/06	6.0	5.1	6.1	8.4	7.5
9/13/06	9.8	6.8	8.9	9.2	8.2
9/14/06	9.1	8.8	9.6	10.5	9.0
9/20/06	10.5	9.4	10.6	11.2	10.3

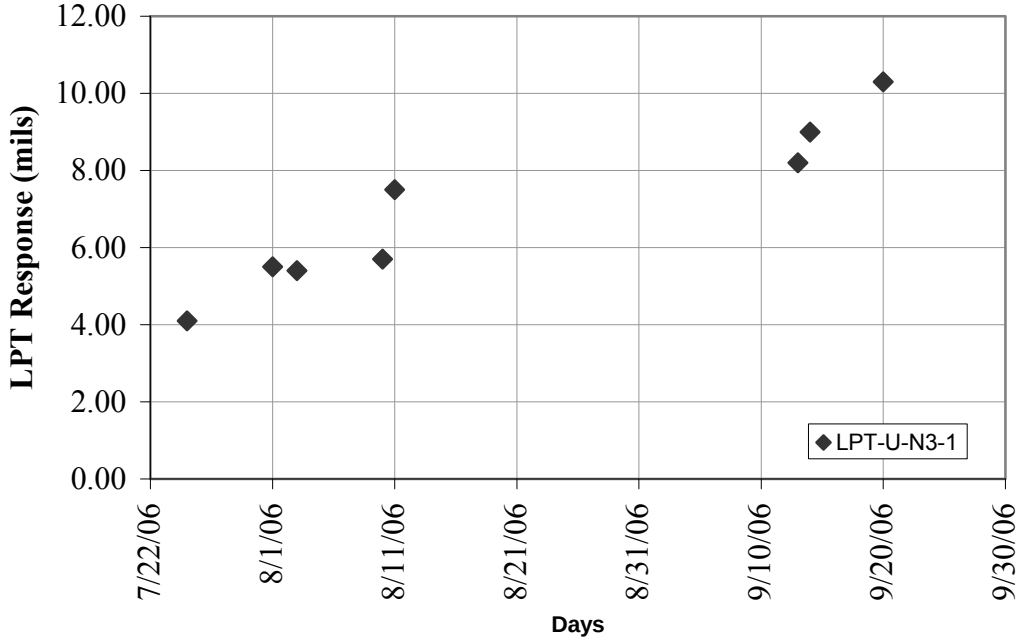

FIGURE 72. RESPONSE AMPLITUDE FROM LPT-U-N3-1 FROM THE LAST LOADING PASS ON EACH DATE

The overlay LPTs exhibited higher response amplitudes on track 0 than on other tracks. The amplitude of downward deflection increased when the loading continued from July 25 and August 3, 2006. When the loading resumed on August 10, 2006 and continued on the next day, there was little or no change in the response of the LPTs. The final period of loading began on September 13 and continued until September 20. There was no loading on the pavement between August 11 and September 13. When the loading resumed on September 13, the amplitude of downward deflection from the first pass on Track 0 had decreased from 23.5 mils to 16.8 mils for LPT-O-N3-3 and from 18.8 to 16.2 for LPT-O-N3-4. When the loading continued from September 13 through September 20, there was an increase in the response amplitudes.

The amplitude of LPT responses with accumulated number of loading passes is illustrated in figure 73. The LPTs in the overlay exhibited a relaxation of downward deflection, whereas the underlay LPT showed no signs of recovery. During the period of loading, the progressive increase in the amplitude of downward deflection may be attributed to the damage accumulation in the asphalt interlayer and fatigue of concrete under repeated loading. During the period of no loading, the downward deflection had exhibited some partial recovery, perhaps due to the viscoelastic properties of the asphalt interlayer.

The LPTs in the overlay showed progressive increase in downward deflection until August and a steep increase thereafter. The underlay LPT also exhibited similar increase until August 10 and a steep increase on August 11. The distress maps indicated that significant cracks occurred in the vicinity of LPTs on August 10. Figure 74, figure 75 and figure 76 show the responses of LPTs U-N3-1, O-N3-3 and O-N3-4, respectively. The LPT responses exhibited disturbances from loading on pass 5 and 6, which may be considered to be indications of crack development.

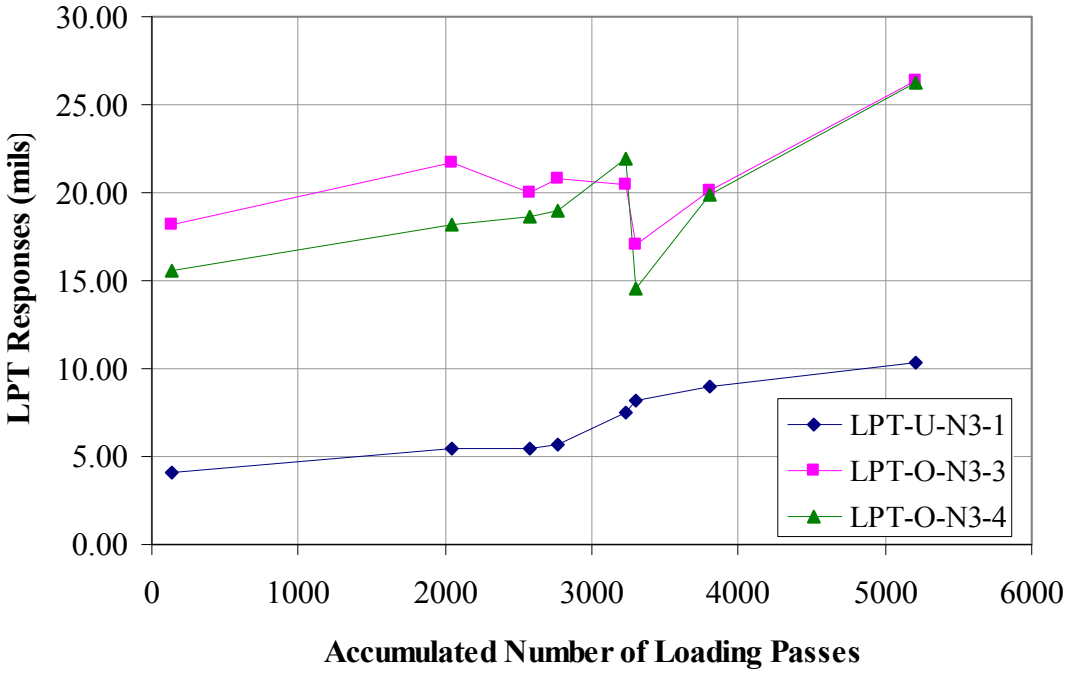

FIGURE 73. LPT RESPONSES VERSUS LOADING PASSES

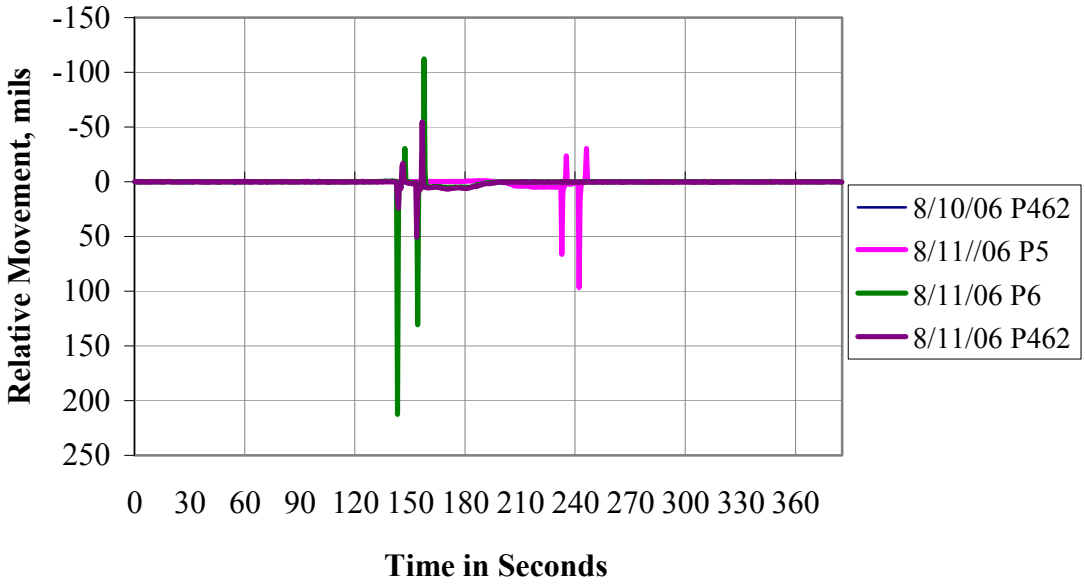

FIGURE 74. RESPONSE OF LPT-U-N3-1 ON AUGUST 10 AND 11, 2006

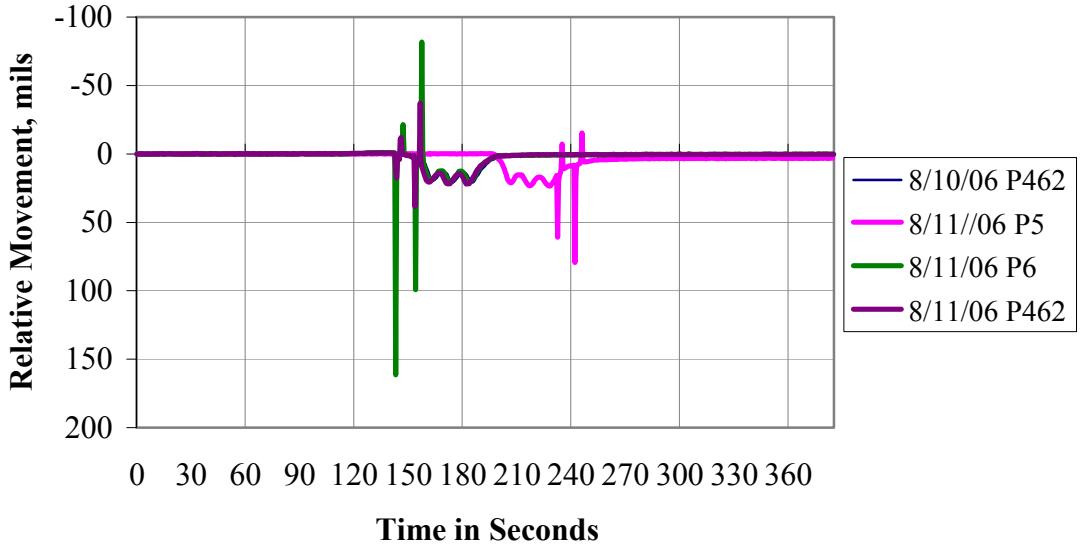

FIGURE 75. RESPONSE OF LPT-O-N3-3 ON AUGUST 10 AND 11, 2006

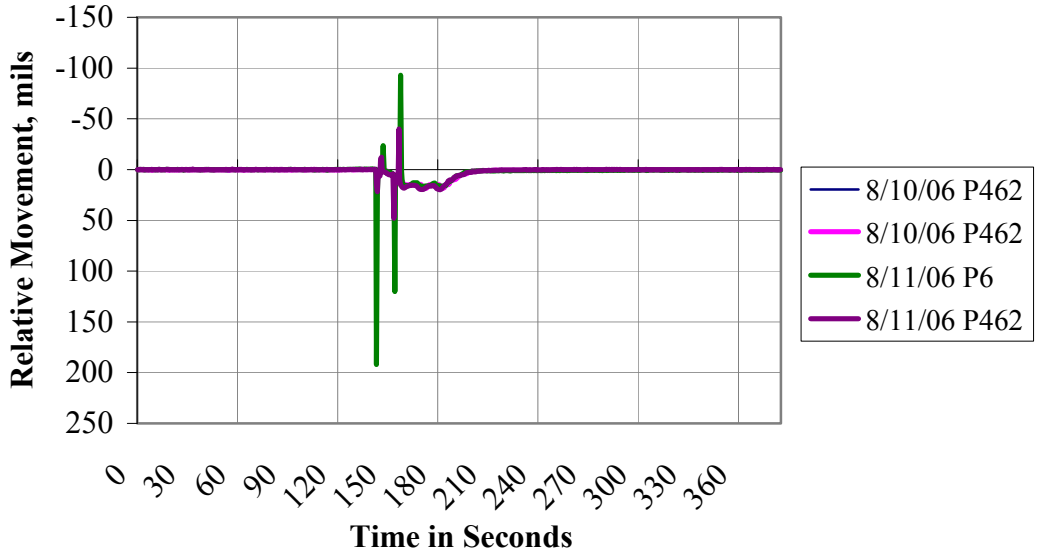

FIGURE 76. RESPONSE OF LPT-O-N3-4 ON AUGUST 10 AND 11, 2006

4.1.4.2 LPT Responses in the Transverse Direction.

The objective of this assessment was to review the responses of LPTs arranged in the transverse rows across the total pavement cross-section. There were seven rows, two each in test items 1 and 3, and three in test item 2 (N2 and S2). LPT readings were extracted for the period from July 25 to August 1, 2006. Measurements were not taken beyond this time period, since the first visible crack appeared on August 1, 2006. The pavement was loaded on July 25, 26, 27, 28 and 31; no loading took place on July 29 and 30.

The LPT readings at the beginning of the first pass were used on loading days, whereas the LPT readings at 5:00 am were considered on days with no loading. The measured deflections, either upward or downward, were normalized from the baseline reference values. The dynamic responses were not considered. Examples of the response plots are included as figure 77 and figure 78.

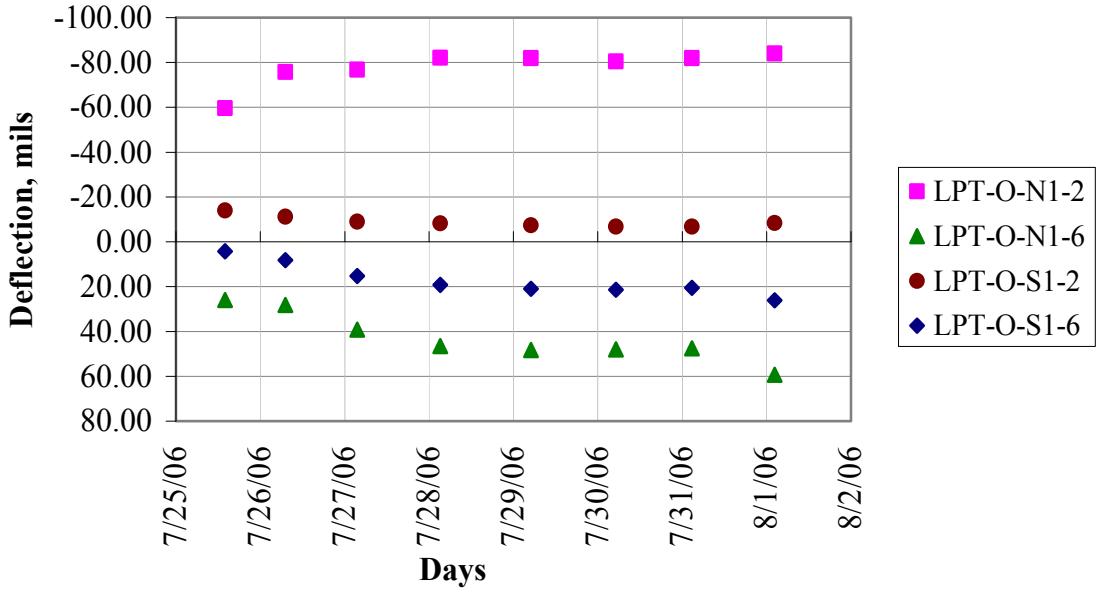

FIGURE 77. ROW OF LPTS IN TEST ITEMS N1 AND S1

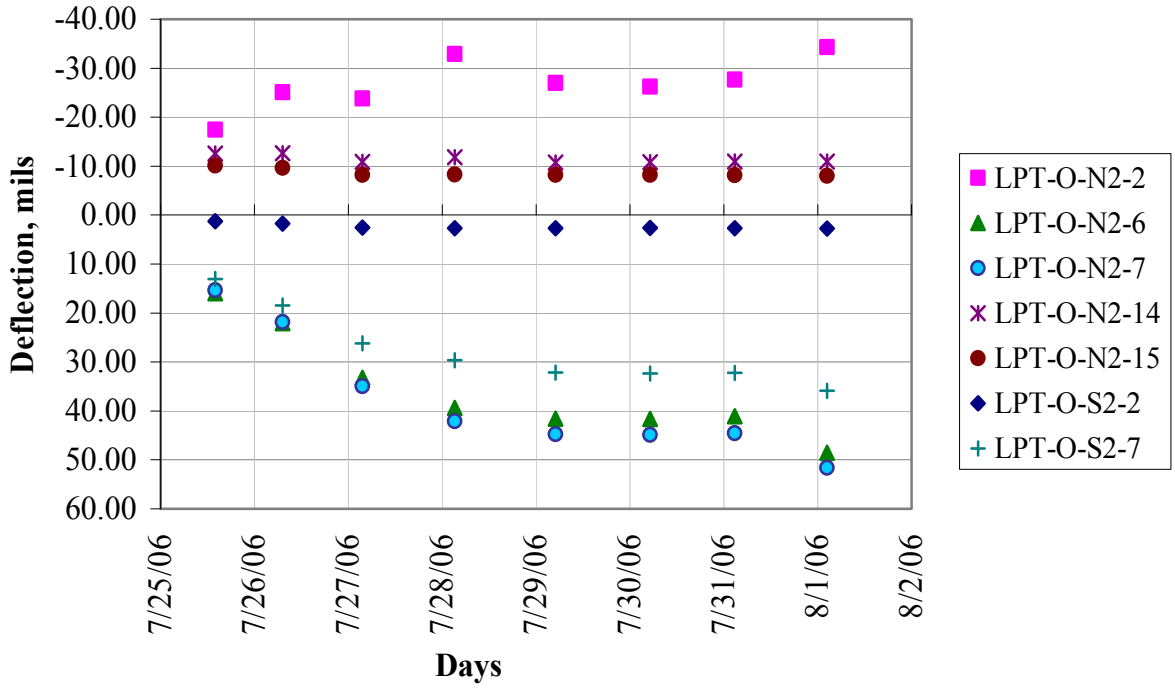

FIGURE 78. ROW OF LPTS IN TEST ITEMS N2 AND S2

4.1.4.3 LPT Responses and Distresses.

The development of cracks affects the responses of the LPTs. The cracks could break the continuity of slab flexure under environmental or vehicular loading. The LPT responses could also provide information about the crack formation in the slab.

The cracks occurring near the LPT locations were summarized based on the distress survey records. Table 32 is an example of such a table, prepared for test items N1 and S1. The tables provide the slab numbers, the crack numbers and the dates of crack occurrence. The dates in parenthesis indicate the extension of the existing crack. This information explains the trends of overall responses of the gages. As a case study, LPT-O-N1-6 is discussed in detail.

TABLE 32. CRACKS ASSOCIATED WITH LPT LOCATIONS IN TEST ITEMS N1 AND S1

LPT	Slab Number	Crack Numbers	Dates
O-N1-1	1N-8	2, 136	8/1, 8/28
O-N1-2	1N-10	4, 212	8/1, 9/19
O-N1-3	1N-1	20, 270	8/3, 9/29
O-N1-4	1N-2	21, 187, 308	8/3, 9/14, 10/2
O-N1-5	1N-2	21, 186	8/3, 9/14
O-N1-6	1N-3	26, 22, 184	8/3, (8/4), 8/10, 9/14
O-N1-7	1N-4	51, 150, 183	8/4, 8/10, 9/14
O-N1-8	1N-4	27,107, 182	8/3, 8/11, 9/14(9/22)
O-N1-9	1N-2	21, 24, 151	8/3, 8/4, 9/13
O-N1-10	1N-4	27, 51, 233	8/3 (8/10, 9/13) 8/4, 9/22
O-S1-3	1S-2	71, 236, 324	8/8, 9/22, 10/5
O-S1-4	1S-4	73, 273, 274	8/10, 9/29
O-S1-5	1S-2	71, 93, 201, 324	8/8(8/9), 8/10, 9/14, 10/5
O-S1-6	1S-4	73, 273, 154, 325	8/8, 9/13, 9/29, 10/5

The overlay LPT-O-N1-6 was installed at the location 357.92, -17.08 in test item N1, in slab 3. The relative movement of the LPT from the baseline reference is shown in figure 79. The peaks observed on 8/10/06, 8/11/06, 8/29/06 and 9/13/06 are marked with red.

The distress map for slab1N-3 associated with LPT-O-N1-6 is shown in figure 80. The pink, blue, gray and yellow lines were the cracks formed on 8/3/06, 8/4/06, 8/10/06 and 9/14/06, respectively. The dashed blue lines are the underlay joints. The days of crack formation matched with the days of peak readings. When the cracks occurred, the LPT apparently exhibited sudden movements.

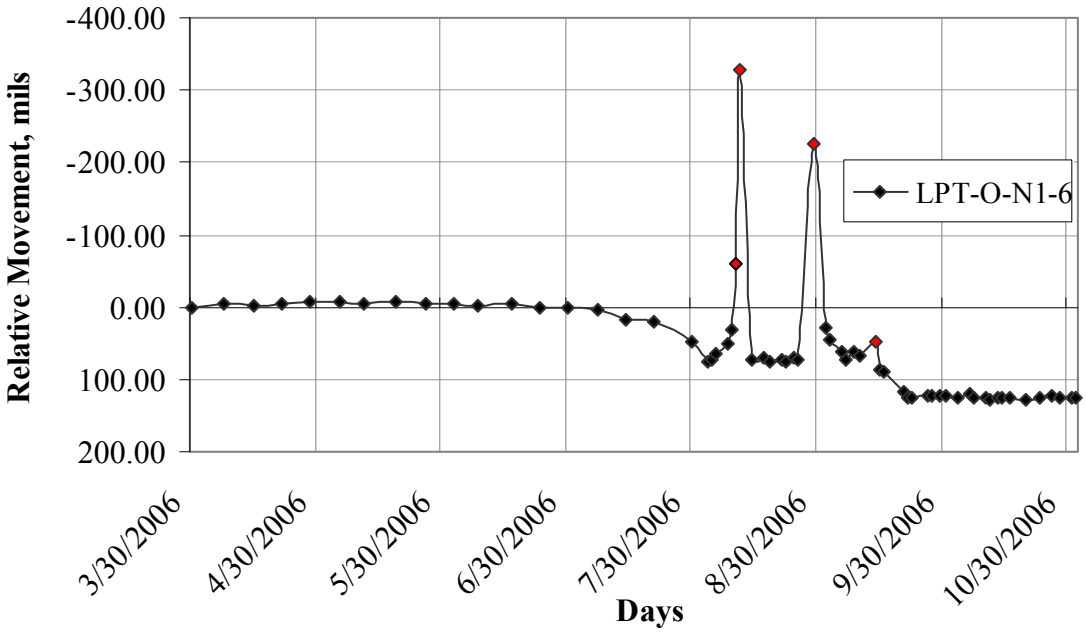

FIGURE 79. RELATIVE MOVEMENT OF LPT-O-N1-6

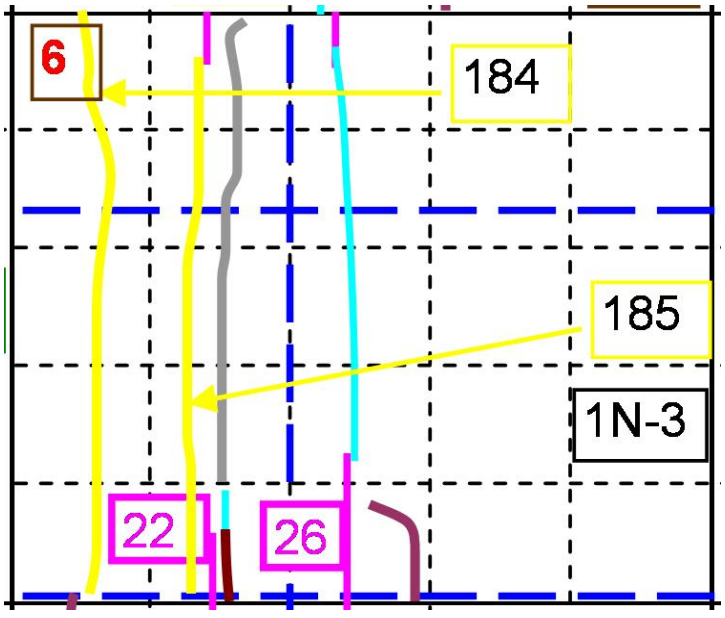

FIGURE 80. DISTRESS MAP FOR SLAB N1-3

4.1.4.4 Fully Monitored Slabs.

The slab geometry resulting from the upward and downward movement of the slabs was monitored by the relative movement of the LPTs. While primarily an environmental response,

this geometry can be critical to understanding and predicting the slab responses. In each north test item, two slabs were instrumented with five LPTs, four at the corners and one in the middle of the slab. Two LPTs were instrumented in loaded corners and two others were instrumented in unloaded corners of the slab. The fully monitored slabs included one with matched overlay-underlay joints and the other with mismatched joints. Table 33 provides the information about the slab numbers and the corresponding LPTs installed in these slabs.

TABLE 33. LPTS IN FULLY MONITORED SLABS

Test Item	Slab Number	Joint Type	Loaded Corners	Unloaded Corners	Midslab
N1	2	Matched	LPT-O-N1-4	LPT-O-N1-11	LPT-O-N1-9
			LPT-O-N1-5	LPT-O-N1-12	
N1	4	Mismatched	LPT-O-N1-6	LPT-O-N1-13	LPT-O-N1-10
			LPT-O-N1-7	LPT-O-N1-14	
N2	2	Matched	LPT-O-N2-5	LPT-O-N2-13	LPT-O-N2-11
			LPT-O-N2-6	LPT-O-N2-14	
N2	4	Mismatched	LPT-O-N2-9	LPT-O-N2-16	LPT-O-N2-12
			LPT-O-N2-10	LPT-O-N2-17	
N3	2	Matched	LPT-O-N3-4	LPT-O-N3-11	LPT-O-N3-9
			LPT-O-N3-5	LPT-O-N3-12	
N3	4	Mismatched	LPT-O-N3-6	LPT-O-N3-13	LPT-O-N3-10
			LPT-O-N3-7	LPT-O-N3-14	

Data from six different days were selected to study the diurnal responses, two dates before loading (before and after seating), two dates during initial loading, and two dates after significant cracking was observed. Plots for slab 2 in test item N2 are included in figure 81 through figure 84.

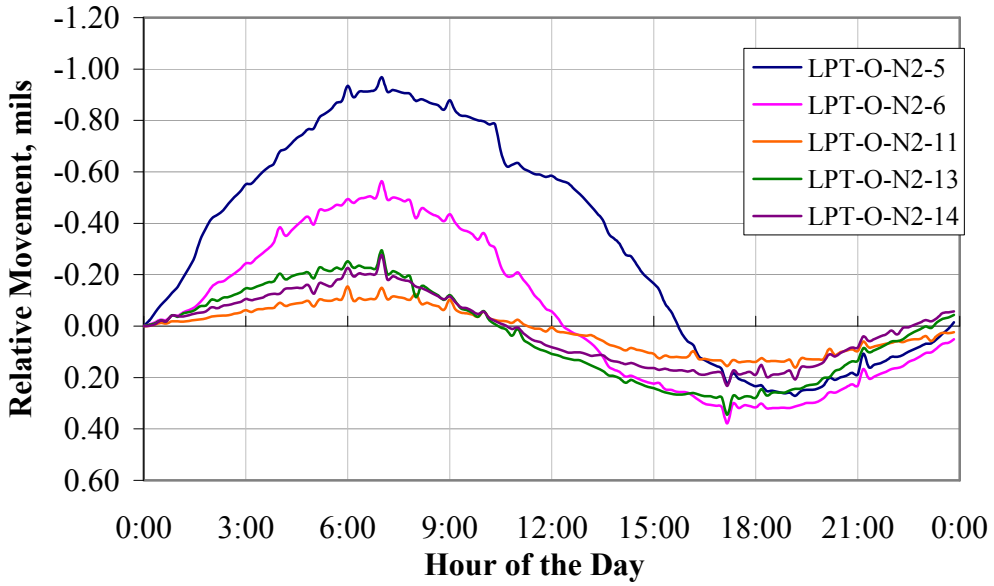

FIGURE 81. MOVEMENT OF SLAB N2-2 BEFORE SEATING LOAD (MAY 1, 2006)

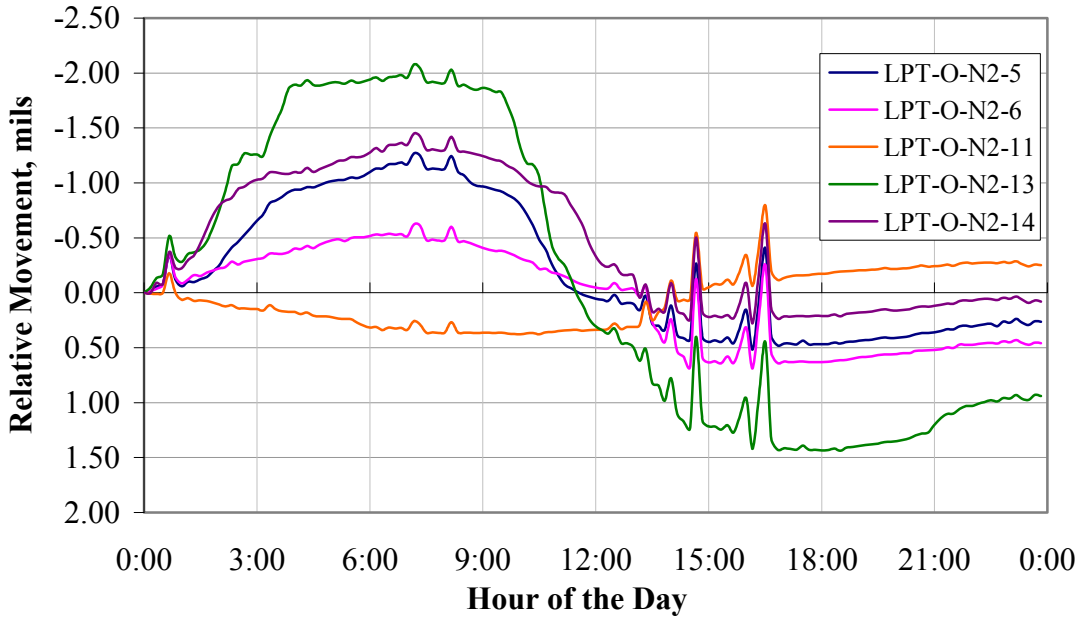

FIGURE 82. MOVEMENT OF SLAB N2-2 AFTER SEATING LOAD (JUNE 2, 2006)

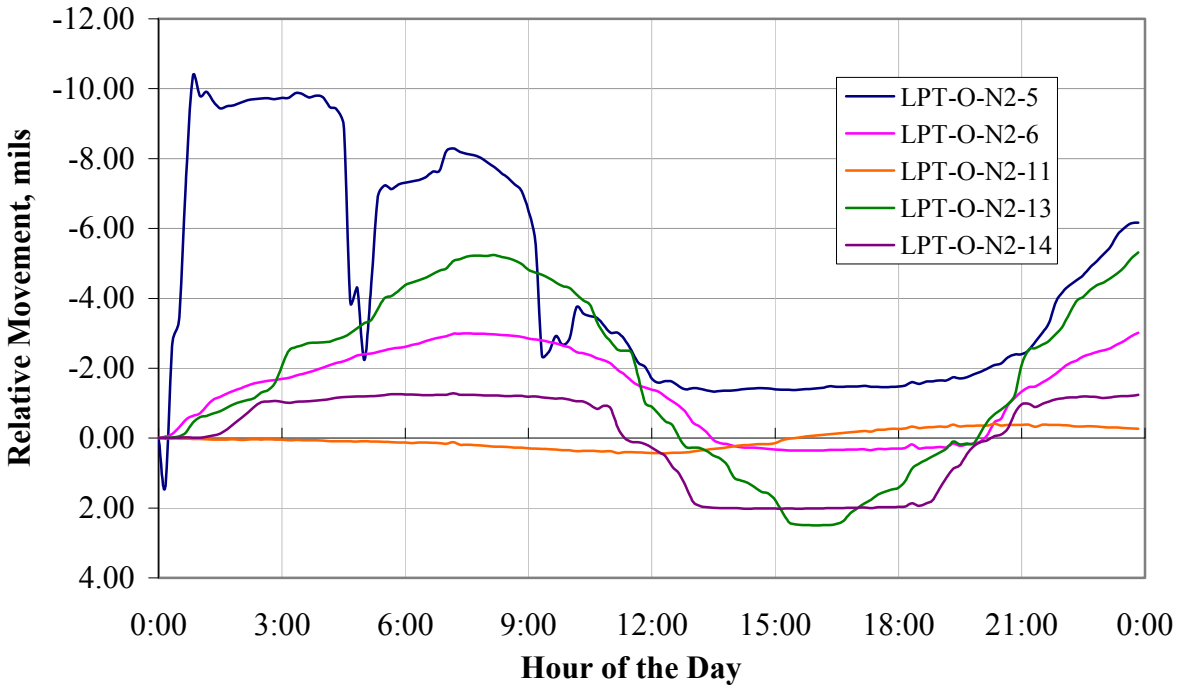

FIGURE 83. MOVEMENT OF SLAB N2-2 AFTER OBSERVED CRACKING (AUGUST 5, 2006)

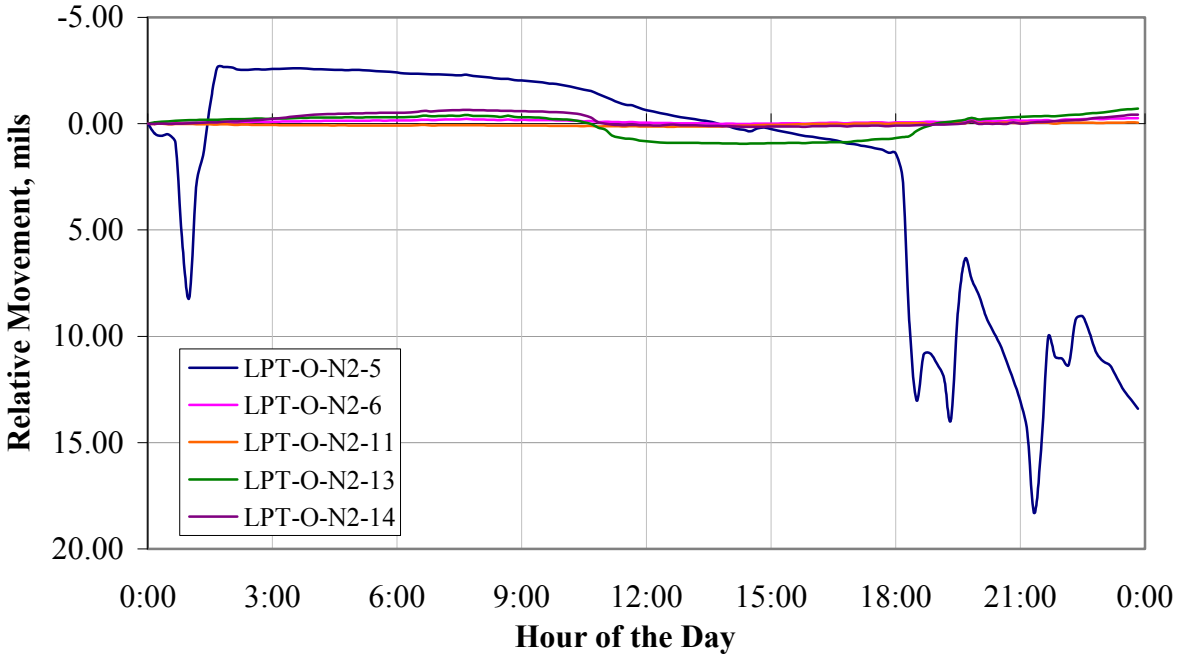

FIGURE 84. MOVEMENT OF SLAB N2-2 BEFORE FINAL LOADING PHASE (AUGUST 26, 2006)

The LPTs installed in the slabs with matched joints exhibited typical trends of upward movement in the early morning hours and downward movement in the late afternoon hours. The LPT at the midslab exhibited either an opposite movement trend to the corners, as in the case of 3N-2, or smaller variations, as in the case of 1N-2 and 2N-2. Only a few LPTs installed in the slabs at mismatched joints exhibited typical trends. The other LPTs at mismatched joints exhibited unstable movement; the presence of an underlying joint beneath these slabs appears to have affected the typical LPT responses. In general, the LPTs in the slabs of test items N1 and N2 exhibited downward movement relative to the baseline reference values, while the LPTs in the slabs of test item N3 exhibited upward movement. It is speculated that this is a consequence of a different thermal response due to the thinner overlay slab.

4.2 HEAVY WEIGHT DEFLECTOMETER ANALYSIS.

4.2.1 Backcalculation of Moduli.

As discussed in chapter 3, all midslab deflection basins for each test item were normalized and plotted for each date. Consolidated graphs of those basins for the 36,000-lb load level are included in appendix D. Backcalculations were also performed for each date.

BAKFAA and ILBK are the two backcalculation programs that were used to obtain the modulus of the concrete slab and the subgrade. In BAKFAA, the pavement structure consists of the concrete overlay, asphalt interlayer, concrete underlay, aggregate base and subgrade. The as-built thicknesses of the overlay, interlayer, underlay and subbase were used. To convert the elastic modulus of subgrade to a k-value, $E_{sub} = 26k^{1.264}$ as suggested in FEDFAA was used.

Table 34 displays the seed material properties for each layer in BAKFAA. The asphalt interlayer was modeled as bonded to the overlay; all other interfaces were modeled as unbonded.

TABLE 34. SEED VALUES USED IN BAKFAA

Layer	E (ksi)	ν	Interface Parameter	Layer Changeable?
PCC Overlay	4000	0.15	1	Yes
Asphalt Interlayer	200	0.4	0	Yes
Concrete Underlay	4000	0.15	0	Yes
Subbase	40	0.45	0	Yes
Subgrade	39.41	0.45	0	Yes

For ILBK, the pavement structure was simplified as a two-layered slab-on-subgrade system. First, the effective modulus (E_e) was backcalculated with ILBK. Then the modulus of the overlay (E_{OL}) and the modulus of the underlay (E_{UL}) was obtained on the basis of a methodology proposed by Ioannides and Khazanovich as shown in Eq. 1, where $\beta = \frac{E_{UL}}{E_{OL}}$ was obtained from BAKFAA.

$$E_{OL} = \frac{h_{OL}^{\ 3}}{h_{OL}^{\ 3} + \beta h_{UL}^{\ 3}} E_e \quad , \quad E_{UL} = \frac{\beta h_{OL}^{\ 3}}{h_{OL}^{\ 3} + \beta h_{UL}^{\ 3}} E_e \qquad \text{[Eq. 1]}$$

All deflection data at midslab was used for backcalculation. However, surface cracking affected the convergence and results of some basins, and those values were not included in calculation of the average properties. Table 35, table 36 and table 37 contain summaries of the backcalculation results for each test period. The strength of each layer apparently decreases with the time due to the accumulation of the passes. The k-value deterioration may be, at least partially, a backcalculation artifact as the deflection basins became distorted due to distress. For the concrete layers, backcalculations indicated that test items N3 and S3 have the lowest E_{OL} and E_{UL}.

The values in tables 35 through 37 are for all midslab HWD locations on each date. The slabs tested on each date are also included. The inner slabs (slabs 1 to 6) received more passes of load and experienced more deterioration than the outer slabs (slabs 7 to 12) in each test item. Figure 85 through figure 90 were plotted for the average backcalculated values of only slabs 1 to 6, to eliminate that additional source of variability. Figure 85 through figure 90 demonstrate the variation of the subgrade, overlay and underlay during the loading period from both BAKFAA and ILBK.

TABLE 35. BACKCALCULATION RESULTS FOR TEST ITEMS N1 AND S1 FROM BAKFAA AND ILBK

Date (2006)	Slabs Tested	N1							S1						
		E_{OL} (psi)	E_{AC} (psi)	E_{UL} (psi)	E_{Base} (psi)	E_{sub} (psi)	k (pci)	Load Passes	E_{OL} (psi)	E_{AC} (psi)	E_{UL} (psi)	E_{Base} (psi)	E_{sub} (psi)	k (pci)	Load Passes
BAKFAA															
6/22	Slab 8 ~ 11	7.26E+06	4.65E+05	1.15E+07	65223	47313	346	0	8.10E+06	3.72E+05	1.10E+07	82212	48085	350	0
7/24	Slab 8 ~ 11	5.71E+06	2.96E+05	9.13E+06	50339	43268	323	0	6.52E+06	3.54E+05	7.69E+06	52154	43864	326	0
7/25	Slab 2 ~ 5	5.81E+06	2.96E+05	5.54E+06	44521	42227	317	0	6.35E+06	3.64E+05	7.37E+06	57781	41171	310	0
7/28	Slab 1 ~ 6	3.49E+06	1.69E+05	3.06E+06	31351	30272	244	1122	4.70E+06	2.24E+05	4.48E+06	40269	35105	274	1122
8/1	Slab 1 ~ 6	2.81E+06	1.47E+05	2.57E+06	28024	26437	220	2046	4.29E+06	2.11E+05	4.05E+06	37689	33678	265	2046
8/9	Slab 1 ~ 12	4.33E+06	2.42E+05	4.63E+06	44160	32155	256	2574	4.80E+06	2.35E+05	4.53E+06	41098	34334	269	3762
8/15	Slab 1 ~ 12	3.85E+06	1.86E+05	3.56E+06	28758	29396	239	3234	5.07E+06	2.21E+05	4.52E+06	37821	34859	273	4818
10/10	Slab 1 ~ 12	4.20E+06	2.07E+05	3.57E+06	26714	29577	240	5214	4.41E+06	2.18E+05	4.68E+06	39072	32288	257	12210
11/7	Slab 1 ~ 12	4.03E+06	2.03E+05	3.42E+06	30079	23898	203	5214	4.71E+06	2.37E+05	5.44E+06	39538	28806	235	12210
11/20	Slab 7 ~ 12	6.22E+06	2.92E+05	4.61E+06	37720	33707	266	5214	7.07E+06	3.96E+05	7.77E+06	59256	37919	291	12210
6/22	Slab 8 ~ 11	4.38E+06	N/A	9.79E+06	N/A	53025	378	0	5.20E+06	N/A	7.08E+06	N/A	53193	379	0
7/24	Slab 8 ~ 11	4.36E+06	N/A	7.13E+06	N/A	44496	330	0	5.62E+06	N/A	4.55E+06	N/A	46025	339	0
7/25	Slab 2 ~ 5	4.60E+06	N/A	4.39E+06	N/A	42192	316	0	4.82E+06	N/A	5.61E+06	N/A	42361	317	0
7/28	Slab 1 ~ 6	3.05E+06	N/A	2.66E+06	N/A	29294	238	1122	3.58E+06	N/A	3.41E+06	N/A	35623	277	1122
8/1	Slab 1 ~ 6	1.96E+06	N/A	1.79E+06	N/A	27125	224	2046	3.45E+06	N/A	3.26E+06	N/A	33554	265	2046
8/9	Slab 1 ~ 12	4.19E+06	N/A	4.52E+06	N/A	31797	254	2574	3.91E+06	N/A	3.68E+06	N/A	34303	269	3762
8/15	Slab 1 ~ 12	3.54E+06	N/A	3.26E+06	N/A	27595	227	3234	4.03E+06	N/A	3.60E+06	N/A	35060	274	4818
10/10	Slab 1 ~ 12	4.24E+06	N/A	3.61E+06	N/A	26304	219	5214	3.76E+06	N/A	4.00E+06	N/A	31782	254	12210
11/7	Slab 1 ~ 12	4.31E+06	N/A	3.65E+06	N/A	21873	190	5214	4.05E+06	N/A	4.58E+06	N/A	28474	233	12210
11/20	Slab 7 ~ 12	5.56E+06	N/A	4.31E+06	N/A	26685	221	5214	5.62E+06	N/A	6.38E+06	N/A	38842	297	12210

TABLE 36. BACKCALCULATION RESULTS FOR TEST ITEMS N2 AND S2 FROM BAKFAA AND ILBK

Date (2006)	Slab Tested	N2							S2						
		E_{OL} (psi)	E_{AC} (psi)	E_{UL} (psi)	E_{Base} (psi)	E_{sub} (psi)	k (pci)	Load Passes	E_{OL} (psi)	E_{AC} (psi)	E_{UL} (psi)	E_{Base} (psi)	E_{sub} (psi)	k (pci)	Load Passes
BAKFAA															
6/22	Slab 8 ~ 11	6.78E+06	4.18E+05	9.06E+06	69651	50635	365	0	6.76E+06	4.00E+05	1.17E+07	79378	50316	363	0
7/24	Slab 8 ~ 11	5.69E+06	3.17E+05	7.82E+06	70024	44832	332	0	5.57E+06	3.16E+05	1.00E+07	61244	46736	343	0
7/25	Slab 2 ~ 5	7.39E+06	4.42E+05	9.50E+06	53099	45226	334	0	7.16E+06	4.14E+05	7.04E+06	48492	47874	349	0
7/28	Slab 1 ~ 6	3.13E+06	1.85E+05	3.70E+06	36801	35922	279	1122	4.89E+06	2.30E+05	4.80E+06	44496	38455	294	1122
8/1	Slab 1 ~ 6	3.56E+06	1.68E+05	3.26E+06	33658	33229	263	2046	4.29E+06	2.07E+05	4.03E+06	38874	36950	285	2046
8/9	Slab 1 ~ 12	4.39E+06	2.22E+05	4.68E+06	42755	37569	289	2574	5.29E+06	2.62E+05	6.05E+06	48259	38939	297	3762
8/15	Slab 1 ~ 12	3.97E+06	2.00E+05	3.79E+06	33494	34739	272	3234	5.48E+06	2.83E+05	6.10E+06	49947	38856	297	4818
10/10	Slab 1 ~ 12	4.12E+06	2.09E+05	4.04E+06	39061	33723	266	5214	4.99E+06	2.75E+05	4.57E+06	42452	35638	277	12606
11/7	Slab 1 ~ 12	4.33E+06	2.19E+05	3.94E+06	35130	27108	224	5214	4.57E+06	1.90E+05	3.96E+06	35829	26424	220	17557
11/20	Slab 7 ~ 12	5.57E+06	2.71E+05	5.69E+06	41773	32311	257	5214	6.88E+06	3.95E+05	7.58E+06	61169	36145	280	17557
6/22	Slab 8 ~ 11	4.51E+06	N/A	5.40E+06	N/A	53077	378	0	3.68E+06	N/A	6.88E+06	N/A	60866	421	0
7/24	Slab 8 ~ 11	4.61E+06	N/A	5.05E+06	N/A	42615	319	0	3.57E+06	N/A	6.35E+06	N/A	50815	366	0
7/25	Slab 2 ~ 5	5.20E+06	N/A	6.11E+06	N/A	48711	354	0	4.94E+06	N/A	4.72E+06	N/A	50099	362	0
7/28	Slab 1 ~ 6	2.08E+06	N/A	2.47E+06	N/A	37205	287	1122	3.32E+06	N/A	3.38E+06	N/A	40349	306	1122
8/1	Slab 1 ~ 6	2.45E+06	N/A	2.22E+06	N/A	34706	272	2046	3.08E+06	N/A	2.89E+06	N/A	39910	303	2046
8/9	Slab 1 ~ 12	3.22E+06	N/A	3.31E+06	N/A	38998	298	2574	3.74E+06	N/A	4.24E+06	N/A	40708	308	3762
8/15	Slab 1 ~ 12	2.93E+06	N/A	2.75E+06	N/A	35440	276	3234	3.81E+06	N/A	4.19E+06	N/A	41055	310	4818
10/10	Slab 1 ~ 12	3.27E+06	N/A	3.11E+06	N/A	32052	255	5214	3.87E+06	N/A	3.39E+06	N/A	35529	277	12606
11/7	Slab 1 ~ 12	3.04E+06	N/A	2.72E+06	N/A	27776	228	5214	3.53E+06	N/A	3.06E+06	N/A	25270	212	17557
11/20	Slab 7 ~ 12	4.42E+06	N/A	4.57E+06	N/A	29599	240	5214	5.60E+06	N/A	6.16E+06	N/A	36992	286	17557

TABLE 37. BACKCALCULATION RESULTS FOR TEST ITEMS N3 AND S3 FROM BAKFAA AND ILBK

Date (2006)	Slab Tested	N3							S3						
		E_{OL} (psi)	E_{AC} (psi)	E_{UL} (psi)	E_{Base} (psi)	E_{sub} (psi)	k (pci)	Load Passes	E_{OL} (psi)	E_{AC} (psi)	E_{UL} (psi)	E_{Base} (psi)	E_{sub} (psi)	k (pci)	Load Passes
BAKFAA															
6/22	Slab 8 ~ 11	5.19E+06	3.61E+05	1.07E+07	72146	48142	351	0	5.88E+06	3.65E+05	8.62E+06	68649	44991	333	0
7/24	Slab 8 ~ 11	7.58E+06	3.89E+05	9.03E+06	60974	44643	331	0	5.65E+06	2.78E+05	7.66E+06	62985	42800	320	0
7/25	Slab 2 ~ 5	4.75E+06	2.81E+05	6.95E+06	51761	44377	329	0	4.40E+06	2.29E+05	6.58E+06	46053	43841	326	0
7/28	Slab 1 ~ 6	3.55E+06	1.62E+05	3.08E+06	29232	34160	268	1122	4.36E+06	2.06E+05	3.93E+06	41406	38156	293	1122
8/1	Slab 1 ~ 6	2.96E+06	1.68E+05	2.84E+06	30406	35446	276	2046	3.13E+06	1.64E+05	2.86E+06	30917	33264	263	2046
8/9	Slab 1 ~ 12	3.98E+06	2.10E+05	4.17E+06	45078	38172	293	2574	4.79E+06	2.44E+05	5.40E+06	46359	36571	283	3762
8/15	Slab 1 ~ 12	3.03E+06	1.83E+05	3.98E+06	37548	34250	269	3234	4.73E+06	2.70E+05	5.40E+06	47700	39215	299	4818
10/10	Slab 1 ~ 12	3.65E+06	2.08E+05	3.77E+06	37944	37891	291	5214	3.86E+06	2.45E+05	5.43E+06	45819	38150	293	12210
11/7	Slab 1 ~ 12	4.21E+06	2.38E+05	4.66E+06	37232	29933	242	5214	5.28E+06	2.62E+05	6.27E+06	44072	29800	241	12210
11/20	Slab 7 ~ 12	7.23E+06	3.41E+05	6.78E+06	44328	40000	303	5214	7.48E+06	3.92E+05	8.69E+06	47851	37868	291	12210
6/22	Slab 8 ~ 11	3.22E+06	N/A	3.22E+06	N/A	51451	369	0	4.05E+06	N/A	5.24E+06	N/A	61997	427	0
7/24	Slab 8 ~ 11	4.83E+06	N/A	2.86E+06	N/A	48584	353	0	2.58E+06	N/A	5.16E+06	N/A	57845	405	0
7/25	Slab 2 ~ 5	2.36E+06	N/A	3.35E+06	N/A	51776	371	0	2.10E+06	N/A	3.11E+06	N/A	51007	367	0
7/28	Slab 1 ~ 6	2.26E+06	N/A	1.87E+06	N/A	36263	281	1122	4.38E+06	N/A	1.35E+06	N/A	38860	297	1122
8/1	Slab 1 ~ 6	1.82E+06	N/A	1.73E+06	N/A	34143	268	2046	1.79E+06	N/A	1.78E+06	N/A	38204	293	2046
8/9	Slab 1 ~ 12	2.29E+06	N/A	2.65E+06	N/A	42582	319	2574	3.11E+06	N/A	3.20E+06	N/A	40477	306	3762
8/15	Slab 1 ~ 12	1.80E+06	N/A	2.34E+06	N/A	36345	282	3234	3.74E+06	N/A	3.18E+06	N/A	43134	322	4818
10/10	Slab 1 ~ 12	2.19E+06	N/A	2.20E+06	N/A	41639	313	5214	2.62E+06	N/A	3.46E+06	N/A	37767	290	12210
11/7	Slab 1 ~ 12	2.71E+06	N/A	2.76E+06	N/A	32475	258	5214	3.25E+06	N/A	3.50E+06	N/A	37309	287	12210
11/20	Slab 7 ~ 12	4.70E+06	N/A	4.20E+06	N/A	44289	329	5214	5.19E+06	N/A	6.06E+06	N/A	40741	308	12210

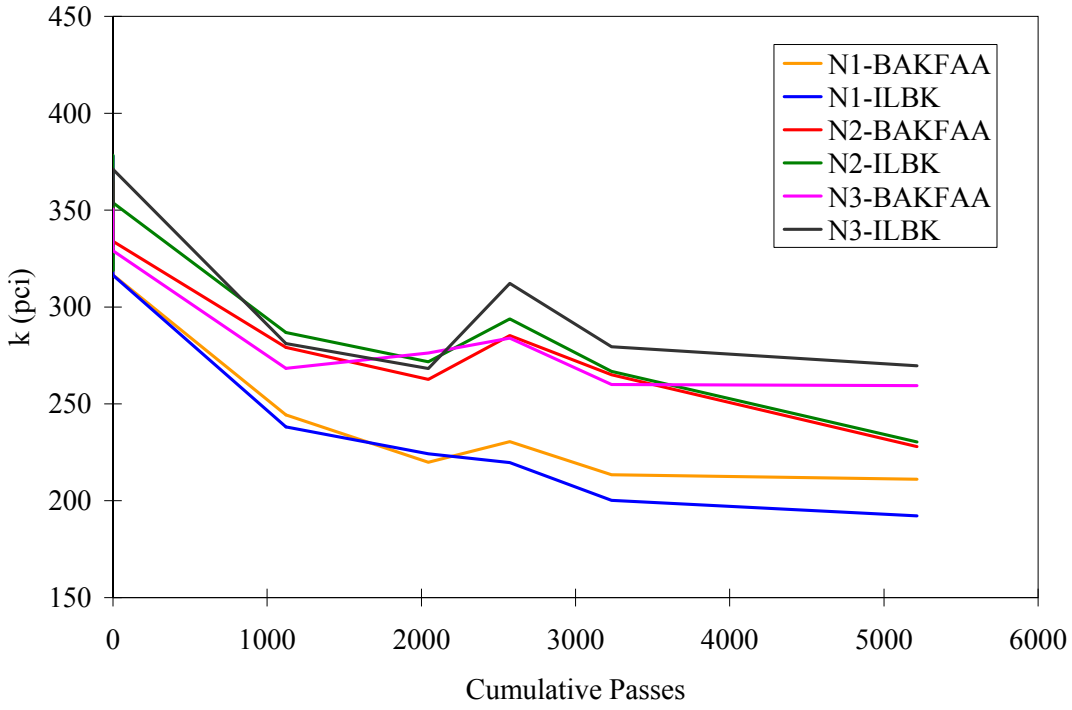

FIGURE 85. BACKCALCULATED MODULUS OF SUBGRADE REACTION FOR NORTH TEST ITEMS, SLABS 1 TO 6

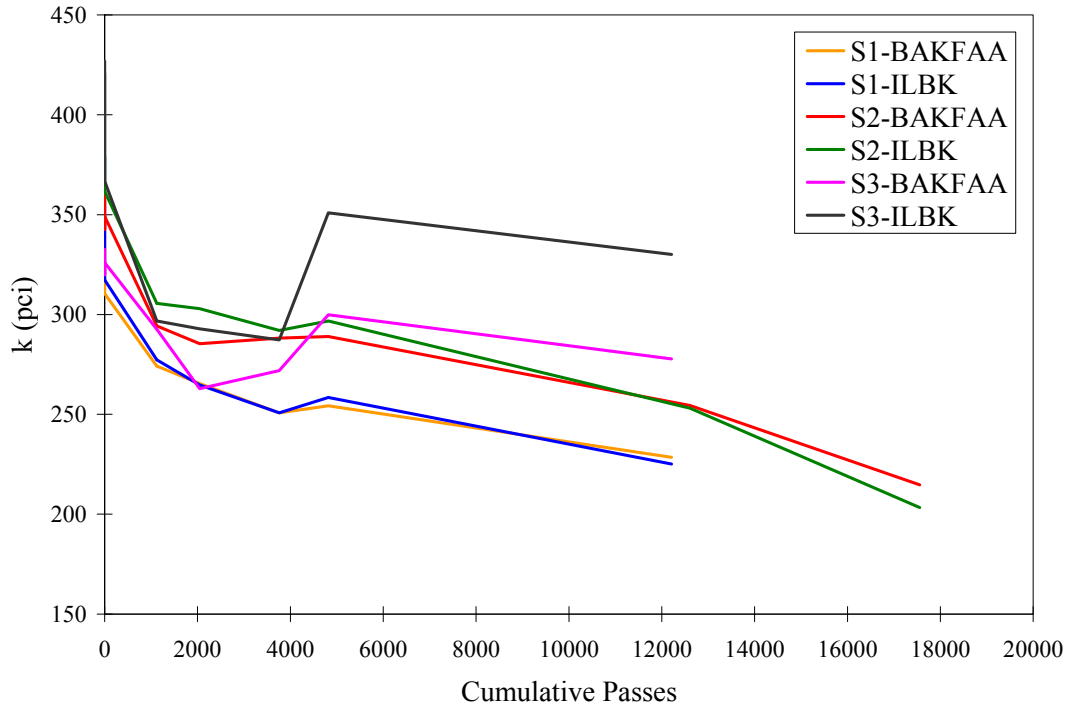

FIGURE 86. BACKCALCULATED MODULUS OF SUBGRADE REACTION FOR SOUTH TEST ITEMS, SLABS 1 TO 6

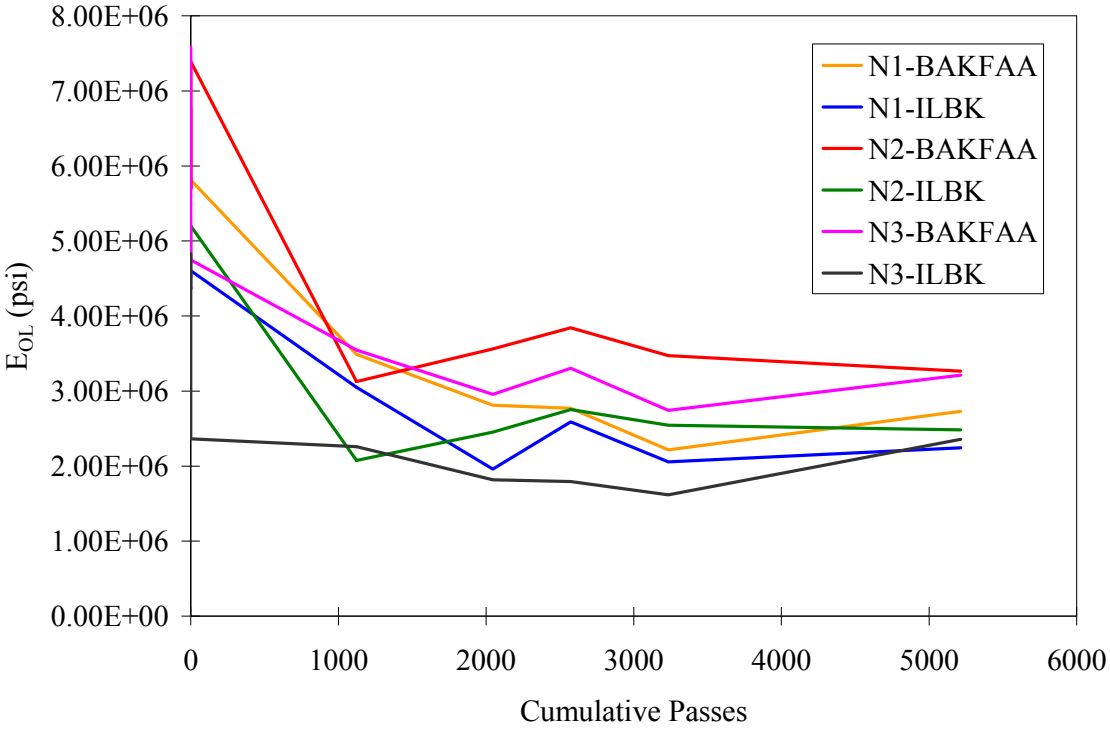

FIGURE 87. BACKCALCULATED OVERLAY MODULUS FOR NORTH TEST ITEMS, SLABS 1 TO 6

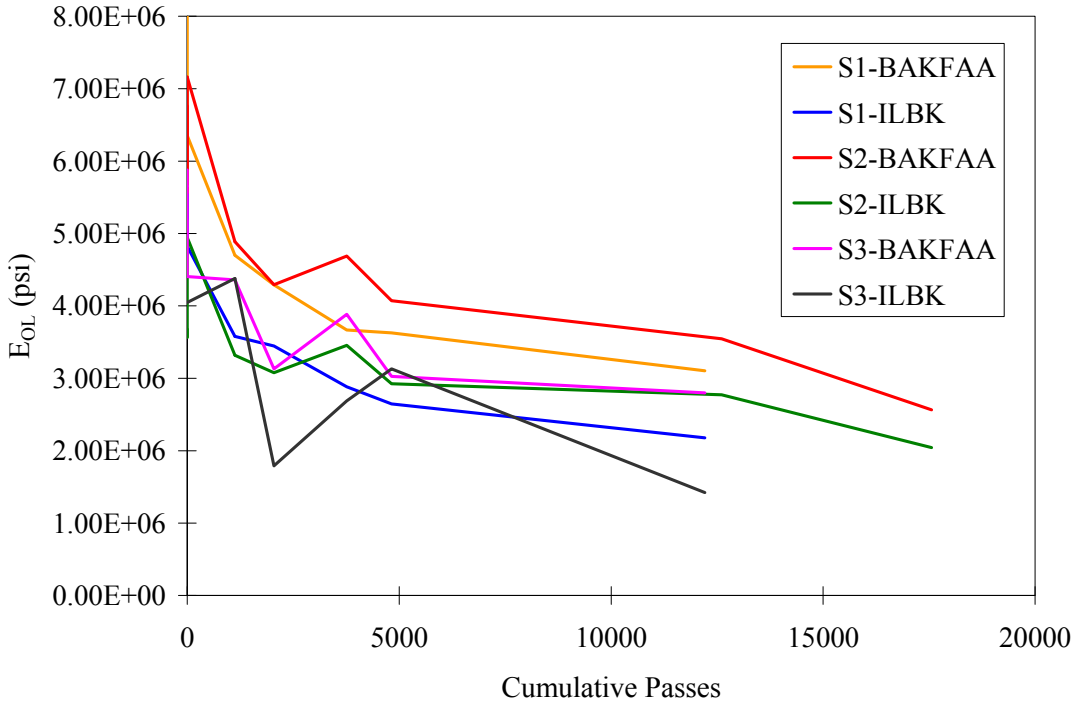

FIGURE 88. BACKCALCULATED OVERLAY MODULUS FOR SOUTH TEST ITEMS, SLABS 1 TO 6

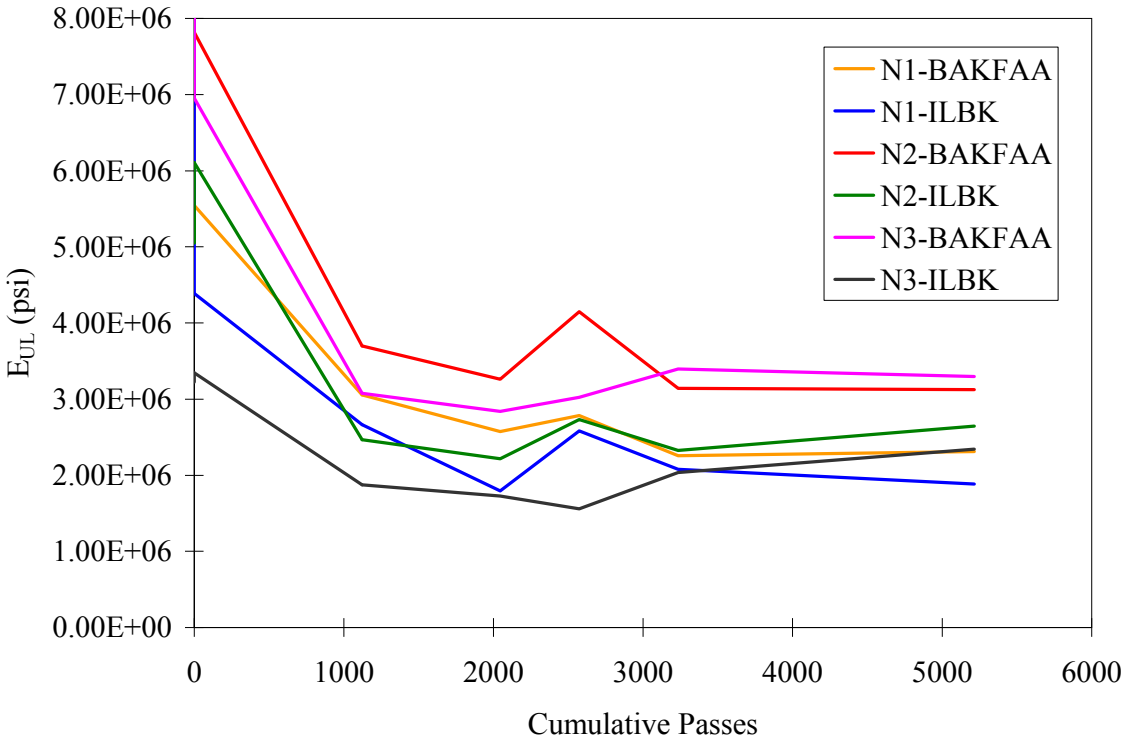

FIGURE 89. BACKCALCULATED UNDERLAY MODULUS FOR NORTH TEST ITEMS, SLABS 1 TO 6

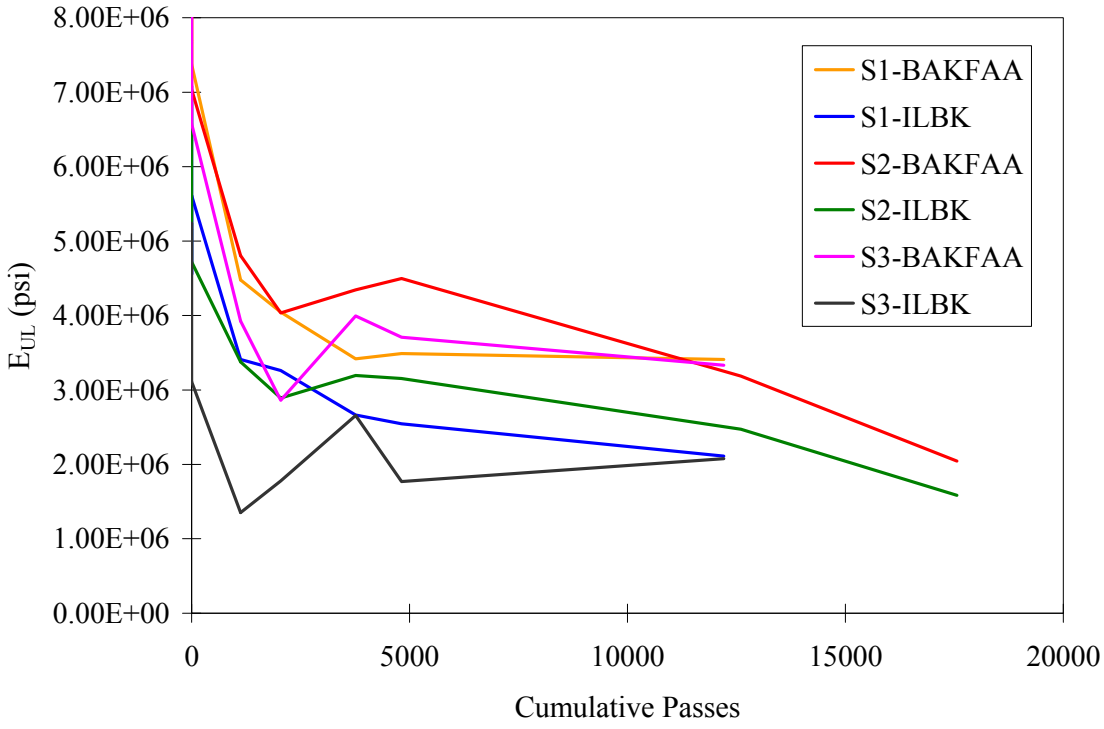

FIGURE 90. BACKCALCULATED UNDERLAY MODULUS FOR SOUTH TEST ITEMS, SLABS 1 TO 6

4.2.2 Backcalculation and SCI Relationships.

This experiment began with intact underlay slabs, but those slabs deteriorated during the testing. The condition of the underlay slabs could not be directly monitored during testing; the instrumentation and the HWD testing provided indications of cracking. As shown in the previous section, backcalculations from the HWD data did indicate that the effective modulus of the underlay slabs decreased as passes accumulated. The equation used for reducing effective E to account for deterioration of the underlay is (Rollings, 1998):

$$E_{SL} = E_O[0.02+0.0064*SCI+(0.00584*SCI)^2]$$

However, direct comparisons could only be made for the final underlay SCI values as observed after demolition, as shown in Figure 91. Figure 91 includes backcalculated values only for slabs 1 to 6; however, the SCI values are those computed for the complete test items. Most of the points in figure 91 are at or near the line of unity, indicating that Rolling's equation is conservative, predicting moduli lower than those from backcalculation. For backcalculations using BAKFAA, and with the E_O value also from the BAKFAA backcalculations, all SCI-modified moduli are less than the corresponding backcalculated moduli.

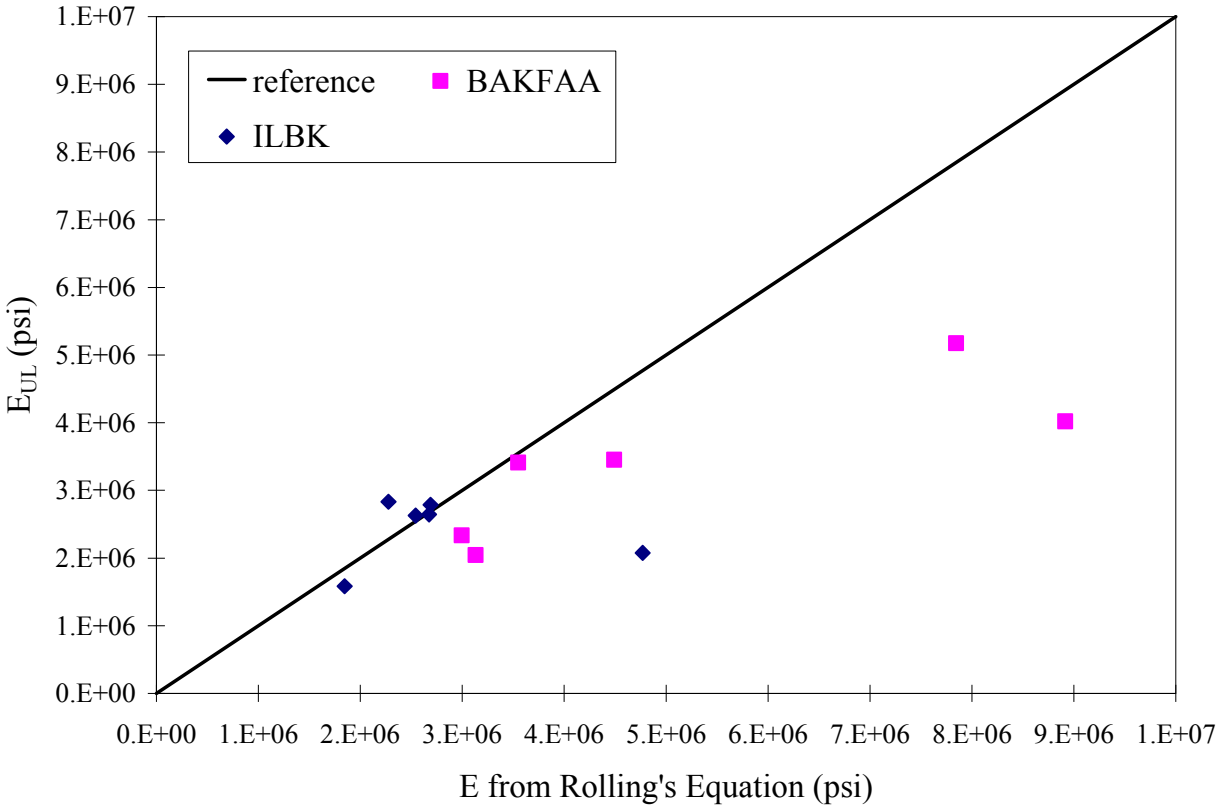

FIGURE 91. COMPARISON OF BACKCALCULATED UNDERLAY MODULUS TO SCI-MODIFIED MODULUS, SLABS 1 TO 6

For the overlay, however, SCI was computed for each distress survey. Therefore, the change in backcalculated modulus with change in SCI could be examined for many more conditions during the deterioration of the slabs. However, the relationship may be different for an overlay than for an underlay, as the underlay is more confined and the deflection relationship may be smoothed over underlay discontinuities. Figure 92 and figure 93 show the change in backcalculated overlay modulus, using BAKFAA and ILBK, respectively, with decrease in SCI for the six test items. These graphs do not indicate monotonic decreases in surface modulus. In figure 94, the backcalculated overlay modulus values are plotted versus the effective modulus computed from SCI. Figure 92, figure 93 and figure 94 include backcalculated values only for slabs 1 to 6; however, the SCI values are those computed for the complete test items. For each backcalculation method, the initial modulus as calculated with that same program was utilized. The moduli are scattered on both sides of the line of unity, with less variation in the backcalculated modulus values than in the SCI-modified values.

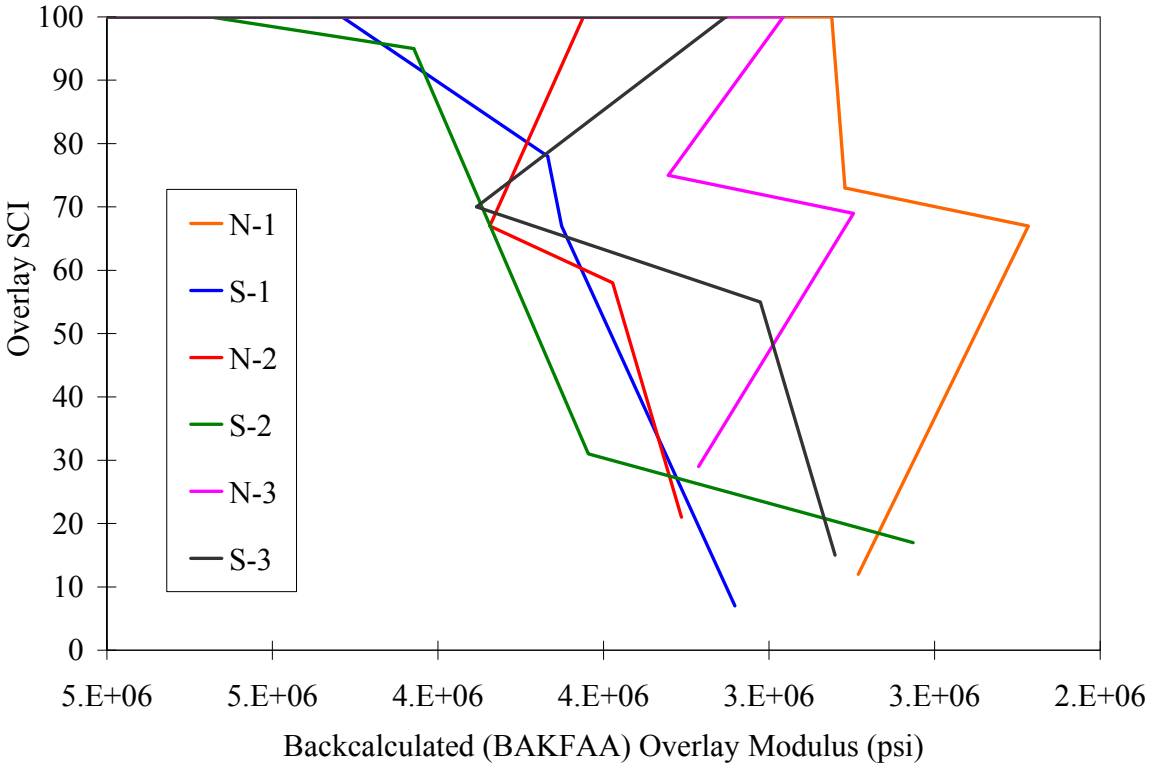

FIGURE 92. CHANGE IN BAKFAA-CALCULATED OVERLAY MODULUS WITH DECREASE IN OVERLAY SCI

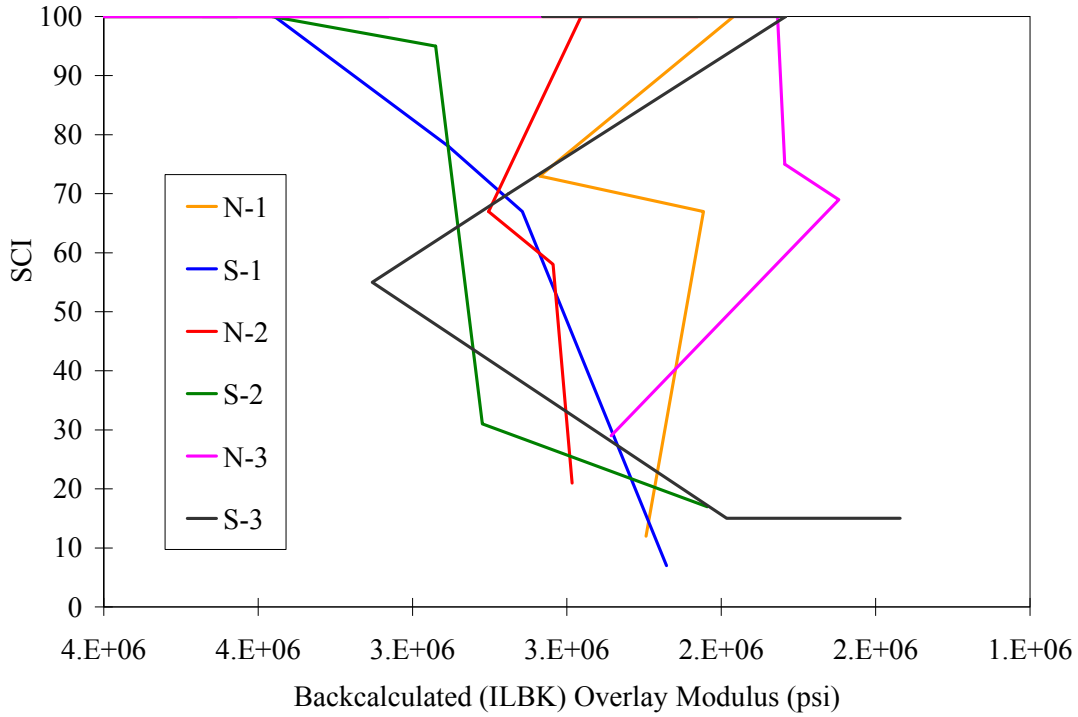

FIGURE 93. CHANGE IN ILBK-CALCULATED OVERLAY MODULUS WITH DECREASE IN OVERLAY SCI

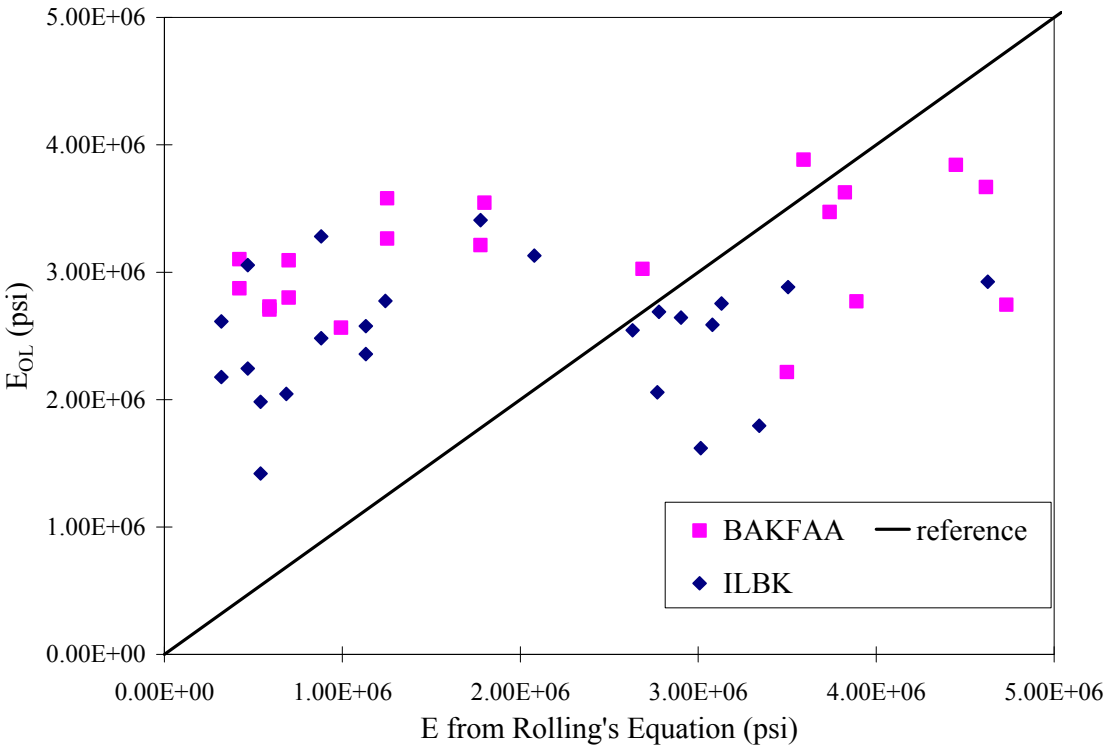

FIGURE 94. COMPARISON OF BACKCALCULATED OVERLAY MODULUS TO SCI-MODIFIED MODULUS

4.2.3 Load Transfer Efficiencies.

Extensive load transfer testing was performed at three time periods. Both regular and corrected load transfer efficiencies were calculated according to the following equations:

$$LTE_{reg} = D1/D0 * 100\%$$

$$LTE_{corr} = D1/D2 * 100\%$$

where D0 is the sensor directly under the load, D1 is the sensor 11.81 in. in front of the load, and D2 is the sensor 11.81 in. behind the load.

The computed load transfer efficiencies increased slightly with load level for some test items and dates, as seen in table 38, for example, and were constant for others. The apparent increases with load level occurred at lower load transfer efficiencies, and are often observed as underlying support provides a greater portion of the load transfer.

TABLE 38. LONGITUDINAL LOAD TRANSFER EFFICIENCIES ON 8/17/2006 FOR TEST ITEM S2

Slab Numbers	Load (lbf)	D0 (mils)	D1 (mils)	Regular LTE (%)
8, 2	12226	6.7	3.88	57.7
	24833	12.2	7.9	64.6
	37234	17.0	11.6	68.2
2, 8	12033	5.1	3.75	74.3
	24702	10.1	7.65	75.8
	36903	14.7	11.24	76.5
11, 5	12189	5.21	4.24	81.4
	24677	10.48	8.62	82.3
	36927	15.25	12.62	82.8
5, 11	12004	5.1	4.05	79.4
	24620	10.75	8.56	79.6
	36915	15.74	12.54	79.7

A summary of the average load transfer efficiencies for all test items for the tests at approximately the 36,000-lb load level is provided in table 39. The corrected load transfer efficiencies are all very high.

TABLE 39. LOAD TRANSFER EFFICIENCIES FOR APPROXIMATE 36,000-LB LOAD LEVEL TESTING

Joint Type	Date	S1		S2		S3		N1		N2		N3	
		LTE_{reg}	LTE_{corr}	LTE_{reg}	LTE_{corr}	LTE_{reg}	LTE_{corr}	LTE_{reg}	LTE_{corr}	LTE_{reg}	LTE_{corr}	LTE_{reg}	LTE_{corr}
Matched Transverse Joints	6/20/2006	90	102	87	99	82	99	89	103	86	99	80	98
	7/24/2006					76	96	89	103	87	98	83	99
	8/16/2006	85	105	81	105	76	99	86	104	84	100	75	100
Longitudinal Joints	6/23/2006	87	98	87	97								
	8/17/2006	77	97	77	94	78	93	78	96	80	103	83	101
Mismatched Transverse Joints	6/20/2006	90	103	87	99	85	99	90	102	87	99	84	98
	7/25/2006							89	99	87	100	81	97
	8/16/2006	85	102	84	106	84	107	87	102	87	105	85	109

The load transfer efficiencies were compared to the performance of the test items, and to the performance of matched and mismatched joints. Observations included:

- For test item S2, there was more cracking in the area which initially had higher load transfer.
- For regular load transfer efficiency, the load transfer efficiency dropped over time as loading increased. The corrected values did not change significantly, however. This may indicate increased bending at the joint, with decreased support.
- For longitudinal joints, the load transfer efficiency dropped with increased cumulative loading, for test items S1 and S2 only. These test items received the greatest number of passes.
- For mismatched transverse joints, as for the longitudinal joints, there was either a slight reduction or no change in load transfer efficiency over time.

The variation in load transfer efficiency was not found to have any quantifiable or strongly observable effect on performance, for either matched or mismatched joints.

4.3 MECHANISTIC MODELING.

4.3.1 2-D Finite Element Modeling.

In order to examine the expected effects of different ratios of the products of thickness and modulus in the overlay and underlay, a series of 2-D finite element runs were performed. For 2-D finite element modeling, the software used was *ILLI-SLAB* (version *ILSL2*, March 1994). Sixty runs were performed, in which the various pavement parameters were varied, as given in table 40.

TABLE 40. INPUT PARAMETERS FOR ILLI-SLAB MODELING

Parameter	**Values**
Subgrade Support, k	100 or 200 pci
Deflection Load Transfer in x-direction, LTE_x	50, 55, 60, 65, 70, 75, 80, 85, 90, 95 %
Deflection Load Transfer in y-direction, LTE_y	75 or 85%
Modulus of Overlay, E1	2E6 or 4E6 psi
Thickness of Overlay, h1	6, 7.5, 9 in.
Poisson's Ratio	0.15
Temperature Differential	-5, -10, -15, -20, -25, +10, +15, +20, +25 °F
Bonding Condition	Bonded w/o temperature differentials; Unbonded w/ and w/o temperature differentials
Geometry	3 panels x 3 panels; each 150 in x 150 in

A single-wheel load was applied, simulating a HWD contact print (area = 109.6 $in.^2$), under 25,000 lbs (pressure = 227.8 psi), and modeled as a square footprint, 10.5 in. on each side. The load was applied at the first interior transverse edge (outer row of panels), in the middle column of panels. This also dictated the location of the maximum responses.

Results obtained are tabulated in table 41, table 42 and table 43, using the following symbols:

D: maximum transverse edge deflection, positive downward
S1: maximum transverse edge bending stress at bottom of overlay, compression positive
S2: maximum transverse edge bending stress at bottom of underlay, compression positive

It is apparent that the bonding condition exerts enormous influence on the responses. On the basis of the design of the test items, as well as the response and performance, it is evident that the unbonded finite element results are more pertinent in most cases. Similarly, the effect of a positive or negative temperature differential can be severe.

TABLE 41. ILLI-SLAB UNBONDED OVERLAY RESULTS

k (psi/in)	LTE_x (%)	LTE_y (%)	E1 (psi)	h1 (in)	E2 (psi)	h2 (in)	D (mils)	S1 (psi)	S2 (psi)
100	50	75	4E+06	6.0	1E+06	10.0	48.2	-743.065	-309.611
200	55	75	2E+06	7.5	2E+06	7.5	33.6	-454.467	-454.467
100	60	75	4E+06	9.0	3E+06	6.0	35.8	-632.546	-316.273
200	65	75	2E+06	6.0	4E+06	10.0	23.2	-165.559	-551.862
100	70	75	4E+06	7.5	1E+06	7.5	44.4	-831.639	-207.91
200	75	75	2E+06	9.0	2E+06	6.0	31.4	-492.516	-328.344
100	80	75	4E+06	6.0	3E+06	10.0	35.0	-405.727	-507.159
200	85	75	2E+06	7.5	4E+06	7.5	28.1	-327.482	-654.964
100	90	75	4E+06	9.0	1E+06	6.0	36.4	-713.546	-118.924
200	95	75	2E+06	6.0	2E+06	10.0	29.0	-275.036	-458.393
100	50	85	4E+06	7.5	3E+06	7.5	37.3	-584.158	-438.119
200	55	85	2E+06	9.0	4E+06	6.0	27.5	-387.21	-516.28
100	60	85	4E+06	6.0	1E+06	10.0	45.0	-698.518	-291.049
200	65	85	2E+06	7.5	2E+06	7.5	31.5	-423.673	-423.673
100	70	85	4E+06	9.0	3E+06	6.0	33.3	-597.384	-298.692
200	75	85	2E+06	6.0	4E+06	10.0	21.4	-156.32	-521.068
100	80	85	4E+06	7.5	1E+06	7.5	41.5	-782.178	-195.544
200	85	85	2E+06	9.0	2E+06	6.0	29.5	-459.43	-306.287
100	90	85	4E+06	6.0	3E+06	10.0	32.1	-384.247	-480.309
200	95	85	2E+06	7.5	4E+06	7.5	26.2	-307.109	-614.218

TABLE 42. ILLI-SLAB BONDED OVERLAY RESULTS

k (psi/in)	LTE_x (%)	LTE_y (%)	E1 (psi)	h1 (in)	E2 (psi)	h2 (in)	D (mils)	S1 (psi)	S2 (psi)
100	50	75	4E+06	6.0	1E+06	10.0	29.4	-49.516	-203.69
200	55	75	2E+06	7.5	2E+06	7.5	19.5	0	-284.806
100	60	75	4E+06	9.0	3E+06	6.0	23.5	-99.815	-299.444
200	65	75	2E+06	6.0	4E+06	10.0	16.3	-11.371	-331.945
100	70	75	4E+06	7.5	1E+06	7.5	29.0	-200.352	-217.048
200	75	75	2E+06	9.0	2E+06	6.0	18.7	-56.95	-284.752
100	80	75	4E+06	6.0	3E+06	10.0	21.7	-9.041	-278.907
200	85	75	2E+06	7.5	4E+06	7.5	16.5	-5.058	-366.725
100	90	75	4E+06	9.0	1E+06	6.0	26.6	-287.991	-197.993
200	95	75	2E+06	6.0	2E+06	10.0	17.4	-8.913	-265.722
100	50	85	4E+06	7.5	3E+06	7.5	23.4	-25.361	-285.31
200	55	85	2E+06	9.0	4E+06	6.0	15.9	-5.785	-335.509
100	60	85	4E+06	6.0	1E+06	10.0	26.8	-47.178	-194.073
200	65	85	2E+06	7.5	2E+06	7.5	18.0	0	-269.578
100	70	85	4E+06	9.0	3E+06	6.0	21.3	-95.3	-285.9
200	75	85	2E+06	6.0	4E+06	10.0	14.7	-10.151	-316.586
100	80	85	4E+06	7.5	1E+06	7.5	26.6	-190.223	-206.075
200	85	85	2E+06	9.0	2E+06	6.0	17.2	-53.883	-269.416
100	90	85	4E+06	6.0	3E+06	10.0	19.3	-8.065	-267.806
200	95	85	2E+06	7.5	4E+06	7.5	14.9	-4.41	-348.375

TABLE 43. ILLI-SLAB UNBONDED OVERLAY WITH TEMPERATURE DIFFERENTIAL (CURLING) RESULTS

k (psi/in)	LTE_x (%)	LTE_y (%)	E1 (psi)	h1 (in)	E2 (psi)	h2 (in)	D (mils)	S1 (psi)	S2 (psi)
100	50	75	4E+06	6.0	1E+06	10.0	62.8	-789.457	-301.98
200	55	75	2E+06	7.5	2E+06	7.5	41.3	-506.736	-442.03
100	60	75	4E+06	9.0	3E+06	6.0	54.0	-712.555	-259.219
200	65	75	2E+06	6.0	4E+06	10.0	31.1	-287.062	-525.502
100	70	75	4E+06	7.5	1E+06	7.5	66.8	-1001.54	-169.501
200	75	75	2E+06	9.0	2E+06	6.00	35.9	-467.453	-333.204
100	80	75	4E+06	6.0	3E+06	10.0	47.0	-296.849	-532.826
200	85	75	2E+06	7.5	4E+06	7.5	31.9	-243.81	-681.737
100	90	75	4E+06	9.0	1E+06	6.0	42.4	-623.351	-147.029
200	95	75	2E+06	6.0	2E+06	10.0	33.0	-124.857	-477.704
100	50	85	4E+06	7.5	3E+06	7.5	51.3	-623.099	-418.794
200	55	85	2E+06	9.0	4E+06	6.0	35.7	-433.576	-491.826
100	60	85	4E+06	6.0	1E+06	10.0	62.4	-841.189	-269.613
200	65	85	2E+06	7.5	2E+06	7.5	41.2	-529.924	-400.512
100	70	85	4E+06	9.0	3E+06	6.0	60.5	-731.545	-204.008
200	75	85	2E+06	6.0	4E+06	10.0	27.7	-125.515	-526.227
100	80	85	4E+06	7.5	1E+06	7.5	49.9	-711.653	-210.266
200	85	85	2E+06	9.0	2E+06	6.0	31.4	-389.233	-324.194
100	90	85	4E+06	6.0	3E+06	10.0	42.6	-167.115	-532.423
200	95	85	2E+06	7.5	4E+06	7.5	28.5	-169.047	-661.624

Comparison of results between the bonded and unbonded overlay cases clearly shows that bonding of the slabs results in reduced tensile stress at the bottom of the underlay slab. At the same time, the tensile stresses at the bottom of the overlay slab are also much greater for the unbonded cases. In most cases, the stresses in both top and bottom slabs are lower for the bonded case. Exceptions are for 7.5-inch and 6-inch bottom slab thicknesses with concrete modulus of the bottom slab of one million.

The effect of temperature curl indicates that the deflection magnitude increases by 7 to 45 percent over those for the unbonded case without temperature differential. Resulting tensile stresses in the bottom of the top slab may be higher or lower than those where temperature differentials are considered, usually plus or minus 20 percent. Changes in tensile stress from top to bottom slab are inverse in most cases. That is, when the stress in the top slab decreased, it was accompanied by a similar increase in bottom slab stress, and visa versa. This appears to hold for the thickness combinations in the experiment, except for two cases of 7.5-inch over 7.5-inch for which the stresses in both top and bottom slabs increase. The relative stress in top or bottom slab is affected not only by thickness, by change in E as well. For example, when E is lower for the top slab, relatively more stress is exerted on the bottom slab, as would be expected.

4.3.2 Dimensional Analysis.

Several of the unbonded cases, with no temperature differential, were then investigated using the principles of dimensional analysis incorporated in the method of transformed sections presented by Ioannides, Khazanovich and Becque (1992). Agreement within 10 to 15 percent was observed when accommodation was made for the factors entering the analysis. Consider, for example, Case 1. The dimensional analysis responses are: D = 74 mils; S1 = 824 psi; S2 = 343 psi. The finite element results indicate that the load transfer efficiency (in terms of stresses) is in this case 23 percent. The corrected S1 value is, therefore, (824/1.23) = 669 psi, which is within 10 percent of the calculated value of 743 psi. Similarly, the load transfer efficiency (in terms of deflections) as calculated by the finite element method is in this case 70 percent. The corrected D value is, therefore, (74/1.70) = 44 mils, which is again within 10 percent of the calculated value of 48 mils.

This example illustrates the potential for utilizing dimensional analysis as a tool in future refinement of unbonded overlay design methodology. It does not preclude the use of other possible approaches, but only provides a sense of the reliability level which dimensional analysis can provide. Additional consideration of the included analysis factors should be undertaken, as a verification of the utility of this approach.

4.3.3 3-D Finite Element Modeling.

Various 3-D finite element programs were considered for modeling the pavement structure, and their capabilities evaluated. For this stage of the analysis, modeling was limited to EverFE. The major limitation of EverFE with regard to the unbonded overlays is the inability to model both jointed layers of the pavement; the underlying pavement is modeled as a continuous layer. EverFE version 2.24 (February 2003) is a 3D finite-element analysis tool for simulating the response of jointed plain concrete pavement systems to axle loads and environmental effects.

4.3.3.1 Modeling of Test Items.

The model used for the primary analysis effort is 3 slabs wide and 3 slabs long with dowels of 1 inch in diameter and 12-inch spacing for both directions. The first and third rows of slabs are 25 feet long and the middle slab is 12.5 feet long. The two end slabs were extended to 25 feet in length, in order to simulate the effect of a larger number of slabs (i.e., 5 slabs long) with a high degree of load transfer (150 ksi for dowel-slab support modulus), thus providing appropriate restraint and support to the inner slab of most interest. The system was modeled as consisting of two layers – a concrete overlay and a concrete underlying slab ($E = 4\times10^6$ psi, $\nu = 0.15$) placed on a supporting subgrade (k = 175 pci). Because of the limitations of EverFE, there are no joints in the underlying slab. Analysis was performed for the thickness of all test items with the appropriate gear (dual tandem or triple dual tandem) and wheel load, and for all nine track positions in the standard wander pattern. Each lateral position of load was modeled at two longitudinal positions from a pass, one when the load is centered longitudinally on the slab, and one when the first wheels of the gear are at the transverse joint. Load positions with the gear straddling the transverse joint were also explored, but not included in the full set of analyses. To clarify the loading geometry and terms, example layouts are illustrated in figure 95 and figure 96.

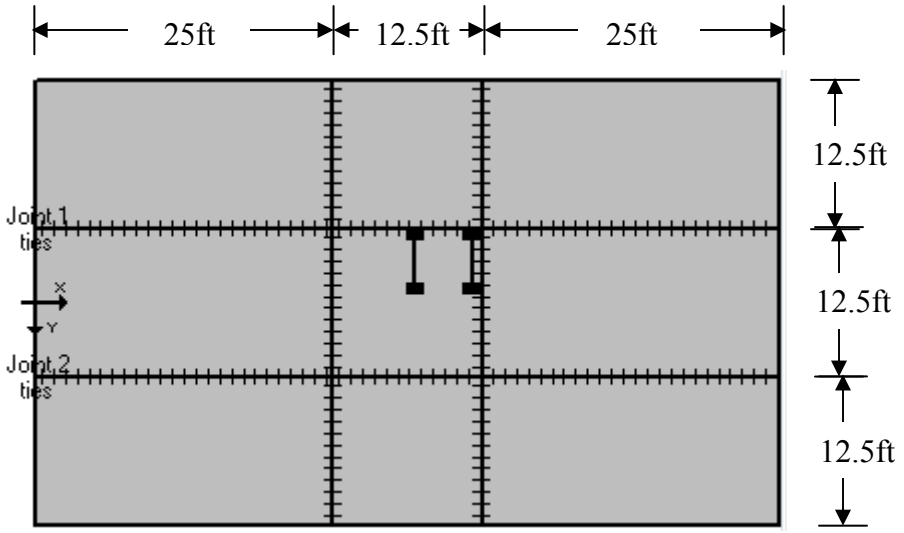

FIGURE 95. DUAL TANDEM JOINT LOADING CASE (TRACK 0)

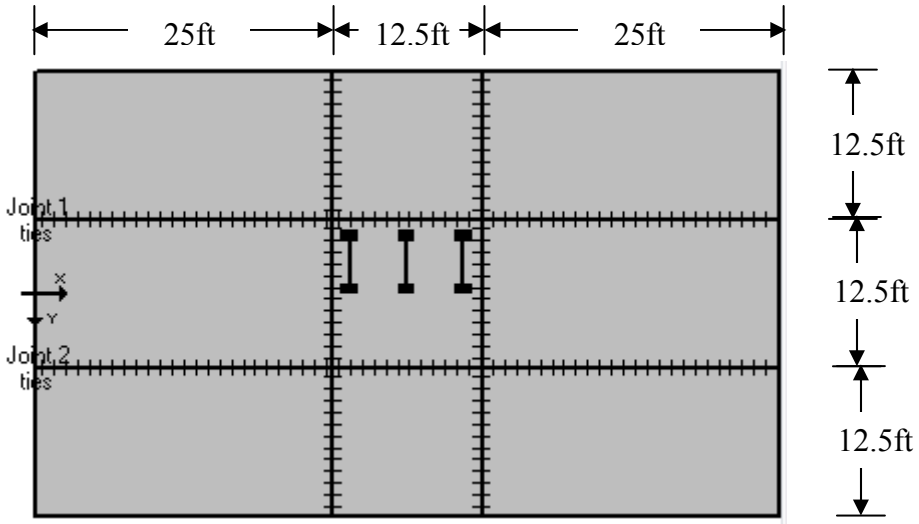

FIGURE 96. TRIPLE DUAL TANDEM CENTER LOADING CASE (TRACK 1)

4.3.3.2 Parametric Studies.

Running a 3-D finite element model such as EverFE is computationally intensive. Determination of appropriate input parameters, mesh size, and assumptions is an important balance between achieving adequately precise output results and the computational and time constraints of computing. The available literature on EverFE was reviewed, and then selected studies performed to determine the input parameters for use for the remainder of the analyses. The

conclusions reached are specific to the material properties and geometry of this project's test items, and are not intended for broader application.

The impact of including an aggregate base layer on the output responses was evaluated. A nine-slab model was evaluated with and without a 5.66-in aggregate base. The resulting principal stresses differed by less than 0.1 percent. Therefore, the aggregate base was excluded from the remaining analysis to simplify the process and reduce computational requirements.

Analyses were conducted with various mesh refinements and aspect ratios. But smaller meshes substantially increase the run time, and at some point do not significantly increase the quality of the results. In addition to affecting the precision of the magnitude of the responses, using a finer mesh also enables researchers to better identify the critical stress location within the slab. EverFE models were run with aspect ratios of 2.0, 2.5, and 3.0. While these aspect ratios produced only a minimal difference in principal stress response, the predicted locations of maximum stress differed by as much as 4 inches. Therefore, it was determined that it was valuable to spend the additional computer run time, and an aspect ratio of 2 was used for subsequent analyses.

Because extensive pre-construction design analysis had been performed with 180-in by 180-in slabs, a comparison was performed to the as-constructed size of 150-in by 150-in slabs. The comparison indicated that the slab size did significantly affect the results, but only in some cases, as demonstrated in figure 97. The differences were considered significant, and, therefore, the relevant runs were repeated with the as-constructed slab size. Both sets of results have been retained for future study on the relationship between gear configuration dimensions, slab thickness ratios and slab size.

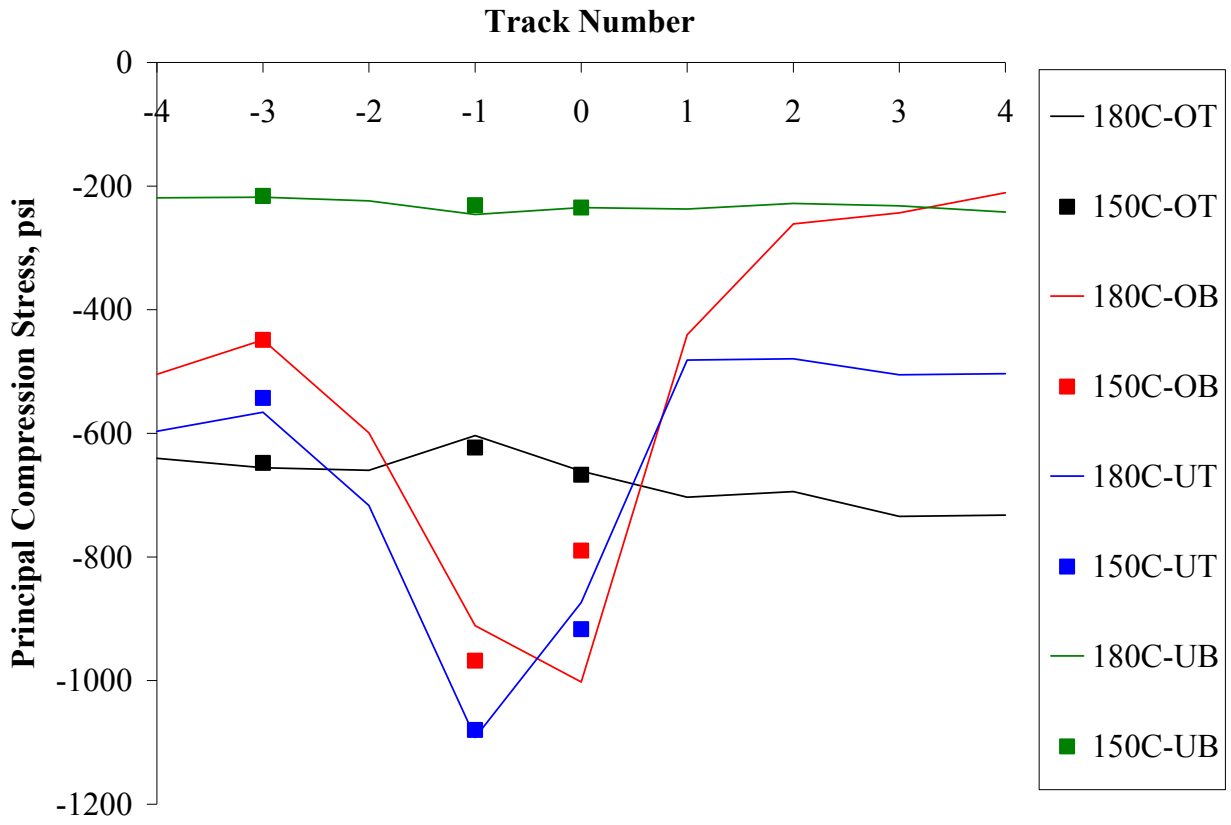

FIGURE 97. COMPARISON OF PRINCIPAL COMPRESSIVE STRESSES (PSI) VERSUS LOADING TRACK FOR 150-IN (12.5-FT) AND 180-IN (15-FT) SQUARE SLABS

In EverFE, two parameters can be used to simulate the bonding condition between an overlay slab and underlay slab: initial stiffness (ksi/in) and slip displacement (in). To model an unbonded overlay in EverFE, values of both parameters were set to 0, 0.02 and 0.025, and the effects on stresses evaluated, using the test item N1 structure subjected to corner loading. After evaluating the effects, both values were conservatively set to zero for future analysis, indicating a completely unbonded condition.

Finally, an evaluation of the results of the load transfer modeling in EverFE was conducted to assess whether the resulting effective load transfers were representative of the test items. The load transfer was initially evaluated to simulate the HWD, for purposes of comparison. The results are shown in table 44. The load transfers modeled in EverFE were very high, when inputs corresponding to the test item dowel bar configuration were chosen. Analysis proceeded with the dowel bar configuration, but effective load transfer under the gear configurations was also evaluated from the EverFE outputs. At the higher total load levels, the deflection load transfer values were slightly lower.

TABLE 44. EverFE MODEL OF HWD LOAD ON TEST ITEM N2

Load (lbf)	D0 (mils)	D1(mils)	Regular LTE (%)
37000	30	29	96
25000	23	22	95
12000	15	14	93

4.3.3.3 Results.

The full results of this analysis have been recorded and saved for comparison with both the instrumentation responses, and analysis methods that may be used in subsequent unbonded overlay experiments. An extensive summary of the results is provided graphically in appendix I. For example, figure 98 contains the maximum principal stresses for the overlay and underlay slabs in test item S1 for the center loading case for five wander tracks. Figure 99 illustrates the maximum horizontal stresses in the transverse direction for the same test item and load positions. Similar figures are provided in appendix I for all test items and loading configurations.

Examination of the output files in terms of stress distributions was also of interest, especially given the longitudinal top-down cracking observed during the full-scale loading of the test items. Therefore, the contour plots showing those stress distributions are also included in appendix I. An example is included here as figure 100 and figure 101, showing the predicted principal stress and transverse stress distributions, respectively.

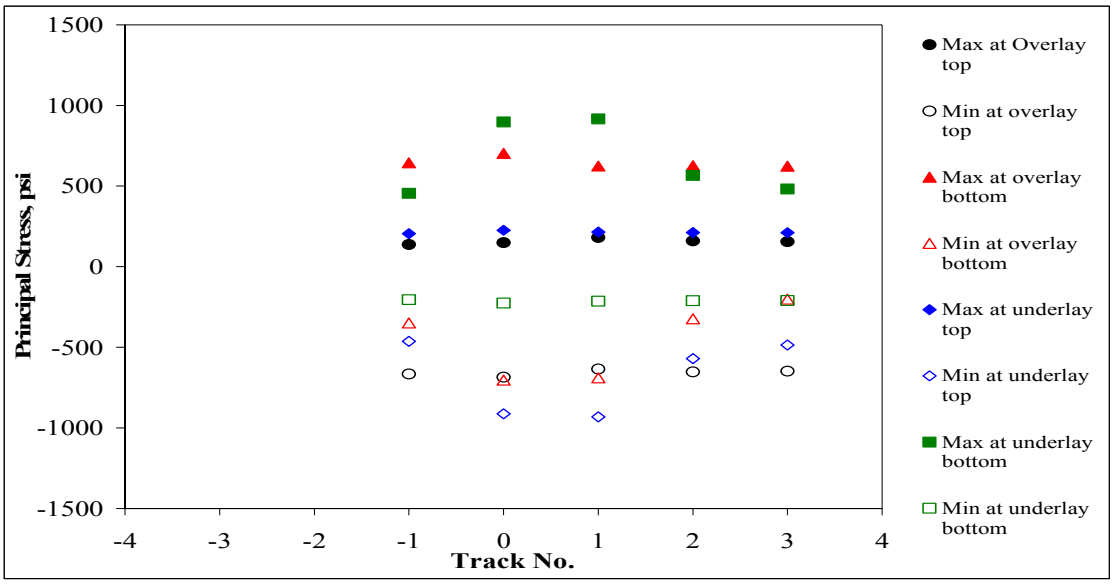

FIGURE 98. PREDICTED PRINCIPAL STRESSES IN TEST ITEM S1 FROM EverFE (CENTER CASE)

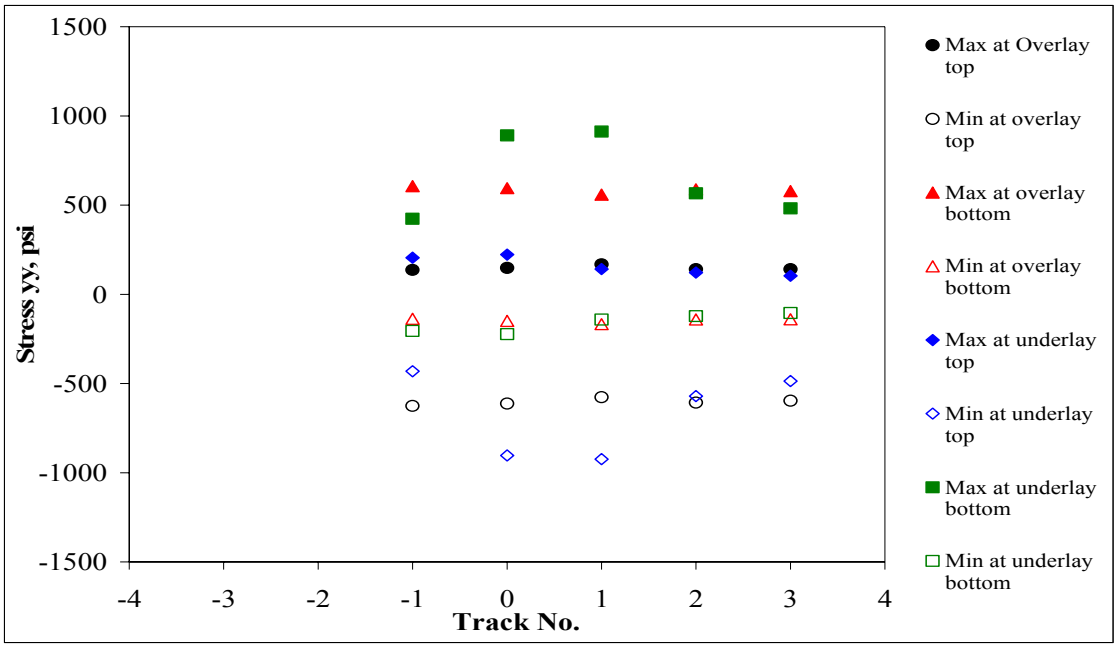

FIGURE 99. PREDICTED TRANSVERSE HORIZONTAL STRESSES IN TEST ITEM S1 FROM EverFE (CENTER CASE)

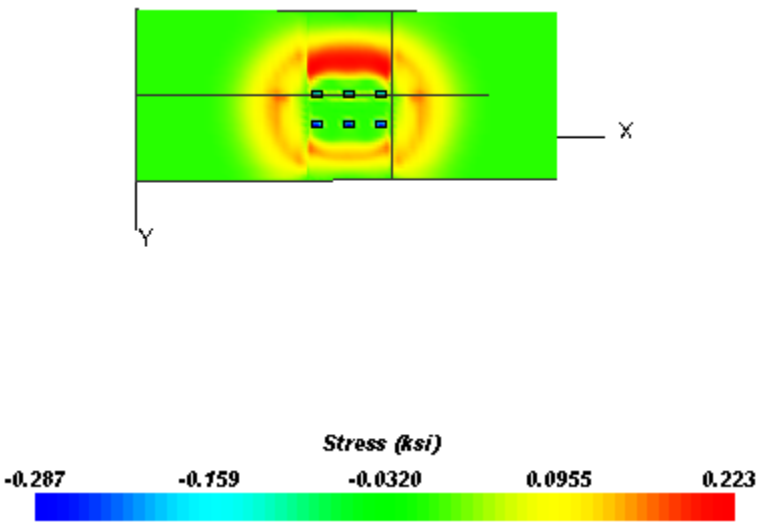

FIGURE 100. MAXIMUM PRINCIPAL STRESS DISTRIBUTION AT TOP OF OVERLAY FOR CENTER SLAB TRIPLE DUAL TANDEM LOADING CASE (TRACK -1)

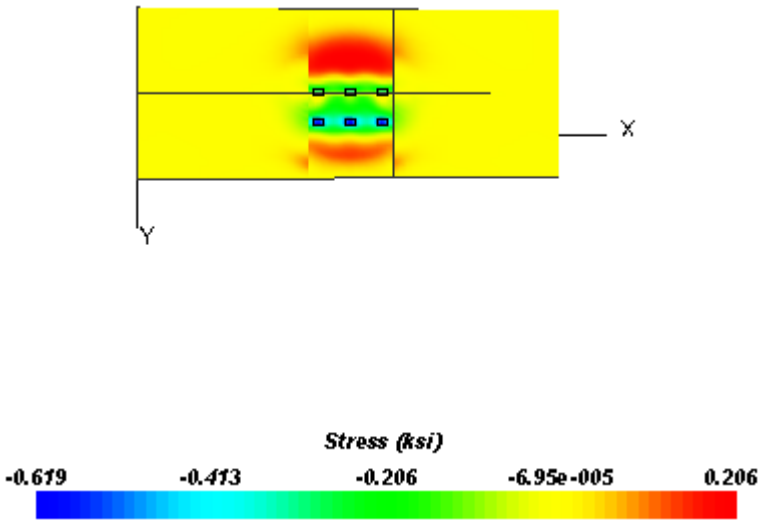

FIGURE 101. σ_{yy} STRESS DISTRIBUTION AT TOP OF OVERLAY FOR CENTER SLAB TRIPLE DUAL TANDEM LOADING CASE (TRACK -1)

In addition to examining the stress distributions and values that relate to life prediction and cracking modes, other response parameters were also examined. Particularly of interest were the corner deflections that should relate approximately to the behavior of the LPTs under load, as tabulated in Table 45.

TABLE 45. EverFE MAXIMUM CORNER DEFLECTION UNDER CORNER LOADING

Test Item	Maximum Corner Displacement (mils)
N1	87
N2	87
N3	81
S1	76
S2	74
S3	68

Also of interest was the pressure transferred to the underlying aggregate base. Although the base was not directly modeled in EverFE, the displacements directly under the underlay slab were considered to be indicative of the pressure. Figure 102 shows the load position (track -3) used to evaluate the base pressure for test items N1 and N3, where four of the soil pressure gages were located. Table 46 provides the maximum displacements at the top of the aggregate base, and the corresponding values of pressure.

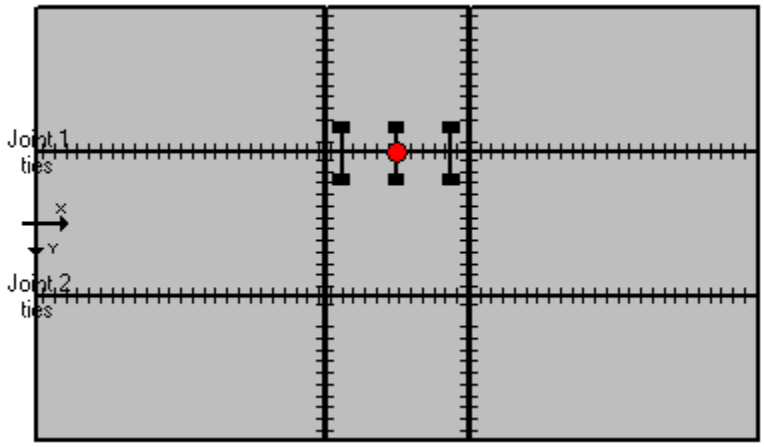

FIGURE 102. APPROXIMATE MAXIMUM DISPLACEMENT LOCATION

TABLE 46. MAXIMUM PRESSURE ON AGGREGATE BASE PREDICTED FROM EverFE

Test Item	Displacement (in)	Maximum Pressure on Aggregate Base Layer (psi)
N1	0.090	15.75
N3	0.082	14.35

4.3.4 Comparison of Predicted and Measured Responses.

As discussed, EverFE runs were completed for all loading conditions, tracks and test items. The major immediate focus at the time of the EverFE analysis was to locate and quantify the maximum principal and horizontal stresses. The longer-term goal, however, is to use these information types together to improve understanding of both the pavement performance and the modeling limitations.

The maximum EverFE-predicted corner displacements for the overlay, under loading, were indicated in table 45 for each test item. The corresponding maximum measured displacements of the overlays from the LPTs were provided in Table 47. Maximum corner deflections for test items N1 and S1, N2 and S2 compare well. Greater difference is observed between N3 and S3. In general, the deflection magnitude decreases from test item 1 to test item 3, for the south side, as well as N1 and N2. N3 exhibited nearly as much deflection as N1. These measured deflections represent the effects of combined slab curl and structural deterioration of the pavement sections. It can generally be concluded that these measurements correlate with the SCI reduction recorded for the various sections as load passes accumulated. As in earlier data comparisons, the balanced h/h section appears to perform better than the other sections, except S3.

TABLE 47. MAXIMUM CORNER DEFLECTION UNDER LOAD

Test Item	LPT	Deflection under load (mils)
N1	LPT-O-N1-6	61.19
N2	LPT-O-N2-5	48.49
N3	LPT-O-N3-7	58.64
S1	LPT-O-S1-5	51.49
S2	LPT-O-S2-6	48.36
S3	LPT-O-S3-5	41.59

The maximum EverFE-predicted pressures on the aggregate base layer were provided in table 46 for test items N1 and N3. These test items were the locations of the consistent pressure cells. The maximum pressure cell readings were provided in table 46. Comparison of the measured deflections and pressure cell readings for test items N1 and N3 indicate that even though the total cross sections for the two pavements are the same, N1 exhibited greater deflection and exerted greater pressure on the aggregate base material than N3.

A direct comparison was made between the strain gage responses and the EverFE predictions. Strains were extracted from EverFE for the elevations, locations and orientation of the embedded strain gages for all test items. To arrive at these strains, the three-dimensional stresses at the gage location were first obtained from EverFE. The three stresses were then used with Hooke's Law to find the strain in the gage orientation. The comparison for test item N1, for gage responses prior to visible distress, is shown in table 48, as an example. Tables for all test items are included in appendix J. The comparison was completed for three loading tracks for each test item. For test item N1, loading tracks 0, -1, and -3 were examined. The predicted strains both over and underpredicted the measured strains. For test item N1, the measured strains were typically lower than those predicted with the EverFE model.

The prediction error was calculated as a percentage of the measured strain. The predictions differ positively and negatively from the measured strains. However, the predictions were based on mean values of material properties, thicknesses and loads, so some variation both ways would be expected. There are many reasons that the measured and predicted strains may differ, including both modeling assumptions and limitations. Localized pavement and materials variability, underlying discontinuities, the asphalt interlayer, and the early development of distress may affect the responses. These considerations were not included in the modeling efforts.

TABLE 48. COMPARISON OF MEASURED STRAINS TO EverFE PREDICTED STRAINS FOR TEST ITEM N1

Test Item	Gage	Edge/Joint	Track Number	Measured Strain, E-6	EverFE Strain, E-6	Prediction Error, %	Absolute Error, %	EverFE Coordinates x	y	z
N1	EG-O-N1-1 B	E	-3	34	59	75	75	320.102	-72.00	-0.4375
N1	EG-O-N1-1 B	E	-1	52	65	26	26	372.241	-72.00	-0.4375
N1	EG-O-N1-1 B	E	0	66	73	11	11	372.241	-72.00	-0.4375
N1	EG-O-N1-1 T	E	-3	-45	-48	6	6	320.102	-72.00	-7.250
N1	EG-O-N1-1 T	E	-1	-66	-61	-8	8	372.241	-72.00	-7.250
N1	EG-O-N1-1 T	E	0	-105	-85	-19	19	372.241	-72.00	-7.250
N1	EG-O-N1-2 B	E	-3	31	56	83	83	320.102	-73.56	-0.4375
N1	EG-O-N1-2 B	E	-1	46	59	30	30	372.241	-73.56	-0.4375
N1	EG-O-N1-2 B	E	0	50	59	18	18	372.241	-73.56	-0.4375
N1	EG-O-N1-2 T	E	-3	-35	-49	39	39	320.102	-73.56	-7.250
N1	EG-O-N1-2 T	E	-1	-64	-68	6	6	372.241	-73.56	-7.250
N1	EG-O-N1-2 T	E	0	-83	-89	7	7	372.241	-73.56	-7.250
N1	EG-O-N1-3 B	E	-3	318	56	-82	82	320.102	-77.04	-0.4375
N1	EG-O-N1-3 B	E	-1	439	66	-85	85	372.241	-77.04	-0.4375
N1	EG-O-N1-3 B	E	0	595	63	-89	89	372.241	-77.04	-0.4375
N1	EG-O-N1-3 T	E	-3	-39	-50	29	29	320.102	-77.04	-7.250
N1	EG-O-N1-3 T	E	-1	-80	-88	10	10	372.241	-77.04	-7.250
N1	EG-O-N1-3 T	E	0	-117	-41	-65	65	372.241	-77.04	-7.250
N1	EG-U-N1-1 B	E	-3	23	46	103	103	320.102	-75.00	6.592
N1	EG-U-N1-1 B	E	-1	28	67	144	144	372.241	-75.00	6.592
N1	EG-U-N1-1 B	E	0	28	64	125	125	372.241	-75.00	6.592
N1	EG-U-N1-1 T	E	-3	-34	-10	-71	71	320.102	-75.00	2.779
N1	EG-U-N1-1 T	E	-1	-41	-22	-45	45	372.241	-75.00	2.779
N1	EG-U-N1-1 T	E	0	-43	-17	-61	61	372.241	-75.00	2.779
N1	EG-U-N1-2 B	E	-3	19	46	142	142	320.102	-75.00	6.720
N1	EG-U-N1-2 B	E	-1	22	67	203	203	372.241	-75.00	6.720
N1	EG-U-N1-2 B	E	0	29	64	123	123	372.241	-75.00	6.720
N1	EG-U-N1-2 T	E	-3	-21	-8	-62	62	320.102	-75.00	2.908
N1	EG-U-N1-2 T	E	-1	-23	-19	-17	17	372.241	-75.00	2.908
N1	EG-U-N1-2 T	E	0	-30	-14	-53	53	372.241	-75.00	2.908
N1	EG-U-N1-3 B	J	-3	31	40	28	28	433.933	-75.00	6.732
N1	EG-U-N1-3 B	J	-1	52	55	6	6	433.933	-75.00	6.732
N1	EG-U-N1-3 B	J	0	45	63	40	40	433.933	-75.00	6.732
N1	EG-U-N1-3 T	J	-3	-43	-6	-85	85	433.933	-75.00	2.920
N1	EG-U-N1-3 T	J	-1	-67	-13	-81	81	433.933	-75.00	2.920
N1	EG-U-N1-3 T	J	0	-54	-13	-76	76	433.933	-75.00	2.920
					AVERAGE	10	60			

The comparison was completed for all test items, with the results different for each. Further investigation is planned into the pattern of variation with loading and position. This analysis also revealed a few gages that were providing questionable responses. For example, the measured response for gage EG-O-N1-3-B is much greater than the predicted. This instrument is proximate to one of the early developed cracks. This area also is noted as having higher entrained air content than other surrounding concrete, which may have resulted in a localized reduction in concrete strength, and thus crack resistance.

5. SUMMARY, DISCUSSION AND RECOMMENDATIONS.

5.1 SUMMARY OF RESULTS.

A major objective of this project was the construction and testing to failure of full-scale unbonded concrete overlay test items at the NAPTF. The baseline experiment from the developed roadmap was executed. The six planned test items were successfully constructed, and all test items cracked and progressed to low SCI values at an acceptable number of passes of the test vehicle at a constant load level. Most of the embedded strain gages, linear position transducers, pressure cells and thermistors used for instrumentation of the pavement provided appropriate data throughout the course of the experiment. Periodic distress surveys and HWD testing were utilized for monitoring the pavement deterioration.

The structural deterioration of the test items, with respect to SCI, is shown in figure 103. The same information is shown in figure 104 on a log scale, which is a conventional method of presenting fatigue-type information. All test items were loaded with a 50,000-lb wheel load. The north test items (N1, N2, N3) were loaded with the triple dual tandem gear, for a total load of 300,000 lbs., while the south test items (S1, S2, S3) were tested with the dual tandem, for a total load of 200,000 lbs. Although the original experimental plan only included loading to an SCI of 80, the loading was extended until all test items reached a target SCI of 20. With only 12 slabs per test item, only minimal structural cracking on a couple of slabs is needed to reach an SCI of 80. The primary mode of cracking was longitudinal cracking, both top-down and bottom-up, and the loading proceeded in an attempt to induce transverse cracks, and to increase the severity of the existing cracks.

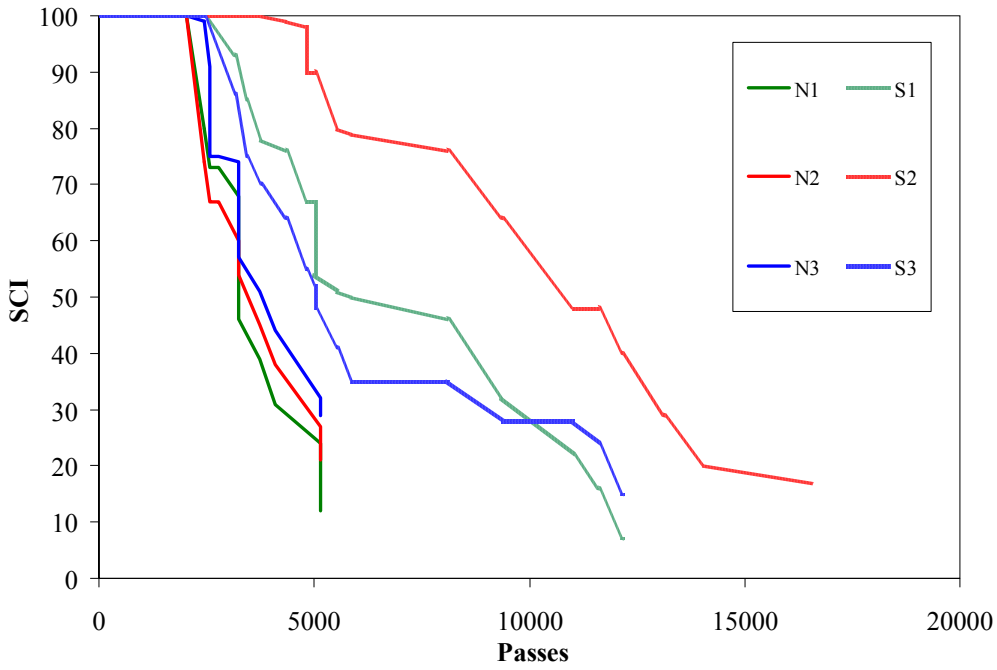

FIGURE 103. STRUCTURAL CONDITION INDEX VERSUS PASSES (ARITHMETIC SCALE) FOR EACH TEST ITEM

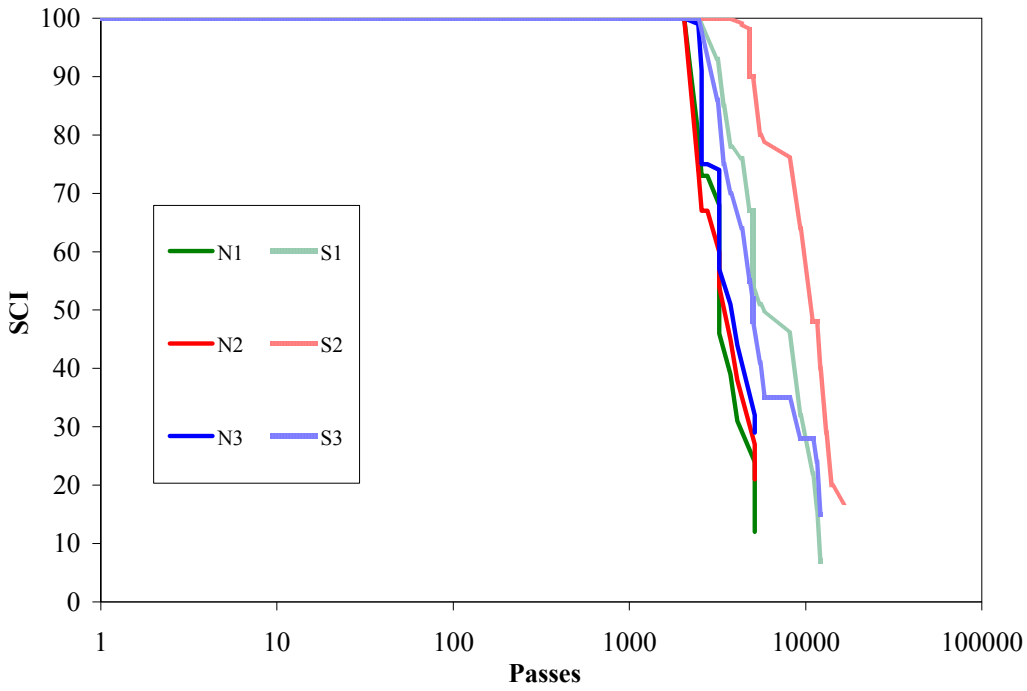

FIGURE 104. STRUCTURAL CONDITION INDEX VERSUS PASSES (LOG SCALE) FOR EACH TEST ITEM

For the north test items, loaded with the triple dual tandem gear from July to October, 2006, failure occurred at approximately the same number of passes for all thickness ratios, the dimensionless parameter for structure, and the ratio of the overlay to underlay slab thickness (h_{ol}/h_{sl}). The primary distress which developed under the triple dual tandem load was longitudinal cracking. Longitudinal cracking first developed during early August (8/1 at 2046 passes). This cracking developed first along the interior longitudinal joint within the wander pattern in the top slab, and inside the outer longitudinal joint within the wander pattern in the top slab. Additional longitudinal cracking also developed between the two longitudinal joints early in August (8/3 at 2524 passes). Additional interior cracking developed during early September. By September 19 (4552 passes), the north triple dual tandem-loaded test items had reached an SCI of approximately 20, and loading of these test items was discontinued after 5146 passes.

For the south test items, the thinnest overlay experienced the earliest cracking, although the thickest overlay reached a lower SCI with further testing. Test item S2 (thickness ratio of 1) was the last to crack. While longitudinal cracking was also a primary mode of distress under the dual tandem load, other transverse and "circular" crack patterns ultimately developed, particularly around joints. Loading began at the same time for both the south and north test items. However, loading of the south test items with the dual tandem continued until October 31, 2006. Test items S1 and S3 were loaded until October 3, while loading of test item S2 continued until the end of the month. Longitudinal cracking similar to that observed in the north test items developed in the south test items during August (8/7 at 3894 passes, but no cracking in S2 at this

time), but required higher loading repetitions to reach the same SCI levels. Additional cracking which appears to be associated with localized stress patterns also developed from August 11 (at 4818 passes) to 28 (5016 passes). Test items S1 and S3 reached the terminal SCI level by October 16, and loading was stopped after 12,142 passes. Section 2 developed significant additional distress between October 3 and October 31 (16,567 passes), and loading was stopped after 16,567 passes.

After completion of the testing, careful demolition of the overlay by the FAA enabled inspection of the underlay slabs. The final SCI values for the underlay slabs were, for each test item, higher than for the surface slabs. The SCI values of the underlay were also proportional to the thickness ratio, with the thickest 10-in underlay in test items N3 and S3 experiencing only minimal distress. The underlay in test item S2, which had the greatest number of load passes applied, had a lower SCI than that of test item N2.

5.2 OBSERVATIONS, CONCLUSIONS AND RECOMMENDATIONS.

5.2.1 Distress Modes and Design Considerations.

5.2.1.1 Dual Tandem and Triple Dual Tandem Differences

Observation: A greater number of passes were required for cracking and deterioration of the south test items than for the north test items. While the same wheel load was applied to the test items, the total load of the triple dual tandem was 150 percent of the total load on the dual tandem. After the passage of each axle, significant and sometimes full strain recovery was observed in the embedded gages.

Conclusion: Because of the number of axles on the triple dual tandem gear, with partial to full recovery between axles, the ratio of wheel loads per pass was 150 percent of the loads for the dual tandem gear.

Recommendation: Many instrument responses show variations in the peaks form axles within a load group, but there is not always complete pavement recovery between axles so the cumulative effect of these responses is not easily quantified. More research is needed to determine the conditions resulting in different degrees of between-axle strain recovery, and refine the analysis of the effect of different load groups.

5.2.1.2 Slab Size

Observation: The slab size may have affected the stress patterns on the north test items (loaded with the longer triple dual tandem gear) more, or differently, than the south test items (loaded with the dual tandem). The dimensionless parameter ESWR/ℓ was greater for the north test items than for the south; the "footprint" of the triple dual tandem gear contacts more of the slab. This was a consideration during the experiment design, but was a compromise in the balance of design factors.

Recommendation: Additional research is needed to understand the effect of different axle configurations and better characterize load group and slab size interactions.

5.2.1.3 Top-Down Cracking

Observation: Examination of the distress patterns shows that the loading resulted in the development of cracking in the top slab as a result of tensile stresses. Cracking outside of the main loading area was clearly predominantly initiated at the surface; while cracking near the center of the wheel track was typically bottom-up cracking. While EverFE analysis does show high surface tensile stresses at the top of the overlay near the top-down crack locations, the magnitude of those predicted stresses is significantly smaller than the maximum tensile strains near the bottom of the slab.

Conclusion: Top-down cracking is the effect of tensile stress at the top of the slab away from the load which results from slab counter-flexure bending. Bottom-up cracking is considered to be the result of conventional load-induced bending tensile stress at the bottom of the slab.

Recommendation: Additional measurements should be obtained on surface strains in subsequent full-scale testing. Top-down cracking should be considered as a potential mechanism in the development of future design models. Further research is needed to identify the pavement and loading characteristics that result in top-down cracking.

5.2.1.4 Longitudinal Cracking

Observation: The developed cracks were predominantly longitudinal cracks. While a reasonable aircraft wander pattern was utilized in the testing, the loading was still set along well-defined and repeated tracks. The loading and peak stresses were thus incremental transversely, but continuous longitudinally.

Conclusion: The loading pattern, while carefully designed, differs from airfield load wander. This pattern may have affected the crack initiation locations and orientations by localizing the transverse peak stresses to specific areas, thus accelerating the formation of longitudinal cracks relative to transverse cracks.

Recommendation: Further work is needed to more accurately characterize the difference in distress development between the experimental setup and actual loading.

5.2.1.5 Corresponding Crack Locations in Top and Bottom Slabs

Observation: The controlled demolition allowed for examination of the cracking patterns with depth. Cracking typically did not progress through the asphalt interlayer, with cracks often offset between the overlay and underlay slabs. Many of the longitudinal cracks were not full-depth over their entire length. In some cases, the longitudinal cracks aligned with dowels in the transverse joints, but in other cases, the cracks occurred between dowel bar locations.

Conclusion: Top slab cracking, particularly top-down cracking, often did not progress through the full depth of the slab. Since no cracking was observed in the asphalt interlayer, and cracks in the bottom slab were not aligned with those in the top slab, it can be concluded that the interlayer and/or the lack of bond relieves crack propagation.

Recommendation: Additional examination of the role of the interlayer and the degree of debonding is needed to better understand these cracking observations.

5.2.1.6 Corner Breaks

Observation: Only a few corner breaks occurred. These breaks occurred later in the testing when the temperatures were colder, mostly on the south test items. The corner breaks also occurred in the bottom slab, and could have originated in either the overlay or underlay, or independently due to changes in slab shape.

Conclusion: The thermal slab gradients produced during colder weather resulted in upward curling of slabs, as measured by the LPTs. When the compressive wheel loads were applied, this resulted in an unsupported corner condition, and corner breaks. However, the frequent watering of the slabs reduced the curl due to drying in the indoor conditions, enabling the key distress mechanisms not to be controlled by curl.

Recommendation: Future experiments should also employ surface watering to control corner breaks. Thermal and drying effects on corner curling should be considered in design.

5.2.1.7 Mismatched Joints

Observation: The distress maps show non-uniform distribution of distresses within some of the test items. The greatest difference observed was between the west slabs and east slabs of test item N1. The east slabs in both the overlay and underlay experienced significantly more deterioration. These slabs had mismatched joints, while the west slabs had matched joints. This pattern was not observed in other test items. No cracks were observed directly over mismatched underlay joints, although cracking was observed closely parallel to the mismatched longitudinal joint. Since the test item longitudinal joints were mismatched, no corner was fully matched.

Conclusion: No consistent and significant difference in performance was observed between the slabs with matched transverse joints and mismatched transverse joints.

Recommendation: The observed performance of these six test items does not support a strong recommendation for either matched or mismatched joints.

5.2.1.8 Relative Thickness of Overlay and Underlay

Observation: Within both the north (triple dual tandem loading) and south (dual tandem loading) test items, the thick overlay over thin underlay test items were observed to have the earliest top slab failure. Test items N2 and S2, with equal thickness of overlay and underlay, performed the longest.

Conclusion: Even with an SCI of 100 in the underlying pavement, a thick unbonded overlay over a thin underlay did not perform well, relative to the cross-sections with balanced structural capacity between the unbonded overlays or with greater structural capacity in the underlay.

Recommendation: Further testing is needed to evaluate the comparable response and performance on cracked underlying slabs. It is expected that threshold thickness or structural capacity ratios can be developed from this effort for implementation in design recommendations and performance prediction.

5.2.1.9 Initiation of Failure

Observation: Observed performance results indicate that unbonded concrete overlays perform well for long stretches of load repetition, with rapid deterioration once a critical threshold condition is reached.

Conclusion: This observation appears to confirm earlier predictions for concrete pavements.

Recommendations: Research is needed to quantify factors contributing to the "critical threshold" and how it can be determined.

5.2.1.10 Effect of Interlayer Bonding to Overlay

Observation: The interlayer was thoroughly bonded to the overlay, and entirely debonded from the underlay. The measured strains indicated that the neutral axis of the overlay slabs was shifted downward.

Conclusion: The bonding of the asphalt interlayer to the bottom of the overlay slab provided a protective effect to the bottom of the slab, reducing the maximum tensile strains in the concrete.

Recommendation: The location of the unbonded interface should be below the asphalt concrete interlayer to protect the bottom of the overlay slab. However, the effect of shifting the slab neutral axis on surface tensile strains should be further analyzed.

5.2.1.11 Base and Subgrade Protection

Observation: The pressure exerted by wheel loads applied to unbonded overlay pavement structures is relatively low, on the order of 15 psi or less.

Conclusion: The majority of the load was carried by the slab system, even after failure according to accepted definitions.

Recommendation: The pressure on the aggregate base should be monitored during loading of test items with damaged existing pavements or underlays.

5.2.2 Instrumentation Responses

In general, the instrumentation provided the expected responses to environmental and load inputs.

5.2.2.1 LPT Devices

For the LPTs, the expected responses generally occurred during periods of loading, with locations directly under the load experiencing downward movement. The underlying slab was not greatly affected in terms of LPT response, until crack damage began to develop in the overlay. Subsequently, the underlying slab experienced increased downward movement. One observation not necessarily anticipated was the recovery during rest periods between loadings; this trend was consistent for all periods without loading. The recovery is attributed principally to the viscoelastic behavior of the asphalt interlayer. Recovery varies somewhat with the length of rest period, and the level of deterioration present in the slabs at the time. When deterioration levels are relatively low, the recovery (as a percentage of maximum deflection) is in the range of 12-25%. Later in the loading cycle when distress was much greater, the recovery was more on the order of 5-10%.

5.2.2.2 Embedded Strain Gages

The embedded strain gages also responded as expected, with strain gages near the top of both the underlay and overlay experiencing compressive strains, and the gages near the bottom of both slabs experiencing tensile strains. All embedded gages are inside the longitudinal joint under the loading track, and not in an area that would experience top slab tension. The strain responses all demonstrated a counter-strain as the load approached, partial strain recovery between the axles, and another strain reversal as the load departed. The degree of strain recovery varied with gage position. For many gages, but notably less so for those near the surface, there was an increase in strain with the passage of each subsequent axle. The top strain gages in the overlay typically experienced a greater magnitude of strain than the bottom strain gages, apparently indicating a shifted neutral axis in the slab. One likely explanation was the asphalt interlayer, which was tightly adhered to the top slab. This may have affected the distribution of top tensile stresses and strains as well, although that could not be discerned with the available instrumentation.

5.2.2.3 Soil Pressure Cells

The soil pressure cells in the aggregate base course produced the greatest responses when the gear configuration was approximately centered over the underlying cell. The pressure increased significantly with pavement deterioration.

5.2.3 Comparison of Results to Design and Analysis Models.

5.2.3.1 FAARfield Passes and Observed Passes

Observation: The predicted passes to failure for the FAA pavement design programs, as used for selecting the testing wheel load level, were presented in table 22. The design predictions were computed for the as-built structural characteristics, but for standard aircraft and for a design k-

value of 175 pci, rather than for the exact test vehicle gear configurations and plate load test results. Table 49 and table 50 provide the FAARfield results for the NAPTF test gear configurations, using the external aircraft library.

A summary of the approximate number of passes required to reach SCI values of 80, 60 and 40 for each test item is presented in table 51. Comparison of the FAARfield predictions to the experimental test item results indicates that the FAARfield results are extremely conservative.

TABLE 51. TEST ITEM PASSES TO SELECTED SCI VALUES

Model or	**Passes (interpolation between survey dates)**					
SCI	**N1**	**S1**	**N2**	**S2**	**N3**	**S3**
SCI = 80	2456	3762	2456	5524	2574	3300
SCI = 60	3234	5016	3234	9370	3234	4580
SCI = 40	3742	8743	4088	12142	4440	5524

Conclusion: While a design program should be conservative, the difference between the observed and predicted passes to all SCI levels for all six test items is very large.

Recommendation: Sufficient information is not available from the six test sections studied to adequately determine the cause for these differences. Additional data points and evaluation will be required to accomplish this.

5.2.3.2 FAARfield Stresses

Observation: Tables 49 and table 50 also included the predicted maximum tensile stresses in both the overlay and underlay slabs.

Conclusion: The failure sequences observed on the test items were reasonably consistent with these predictions in a qualitative sense. For example, the stresses in the thick 10-in underlay as predicted by FAARfield were significantly lower than for the thinner underlay slabs. No explanation for this difference has been identified at the present time. After completion of the load tests and demolition, those thicker slabs had minimal distress as compared to the thinner underlay test items. The stress values in tables 49 and 50, however, are for intact pavement cross sections; once the overlays were severely deteriorated, the stress magnitudes in the underlay would have increased substantially.

Recommendation: Future experiments should be conducted including slabs with initial damage, and various ratios of overlay and underlay structural capacity.

TABLE 49. FAARFIELD RESULTS FOR VARIOUS TERMINAL SCI VALUES (MODULUS OF RUPTURE = 550 PSI)

FAARFIELD - Failure Criteria "SCI" Comparison						
Inputs	Section 1 (8.63 in. PCC / 6.32 in. PCC / 5.66 Agg base)		Section 2 (7.38 in. PCC / 7.51 in. PCC / 5.60 Agg base)		Section 3 (5.67 in. PCC / 9.78 in. PCC / 4.75 Agg base)	
	North	South	North	South	North	South
	Dual Spacing: 54in, Tandem Spacing: 57in, Gear Spacing: 354in, LOAD:50K lbs/wheel, Tire Pressure: 230psi, Annual Depature = 1					
	Epcc = 4000000psi, MR = 550psi, E_{base} = 21644psi, K_{sub} = 135psi, failure criteria: SCI = 80					
Passes	6	7.2	6.1	7.1	9.6	12.2
Stress (slab/overlay), psi	416.56 / 650.43	407.45 / 637.42	450.09 / 666.87	438.48 / 653.17	370.1 / 692.25	361.99 / 682.79
Variable	Failure Criteria: SCI = 60					
Passes	7.6	9.1	7.3	8.7	10.7	13.4
Stress (slab/overlay), psi	416.56 / 650.43	407.45 / 637.42	419.21 / 681.84	408.76 / 668.34	339.36 / 726.92	361.99 / 682.79
Variable	Failure Criteria: SCI = 40					
Passes	9.6	11.6	8.9	10.5	11.8	14.8
Stress (slab/overlay), psi	416.56 / 650.43	407.45 / 637.42	387.94 / 697.33	408.76 / 668.34	336.96 / 723.8	332.56 / 717.88

TABLE 50. FAARFIELD RESULTS FOR VARIOUS TERMINAL SCI VALUES (MODULUS OF RUPTURE = 700 PSI)

FAARFIELD - Failure Criteria "SCI" Comparison						
Inputs	Section 1 (8.63 in. PCC / 6.32 in. PCC / 5.66 Agg base)		Section 2 (7.38 in. PCC / 7.51 in. PCC / 5.60 Agg base)		Section 3 (5.67 in. PCC / 9.78 in. PCC / 4.75 Agg base)	
	North	South	North	South	North	South
	Dual Spacing: 54in, Tandem Spacing: 57in, Gear Spacing: 354in, LOAD:50K lbs/wheel, Tire Pressure: 230psi, Annual Depature = 1					
	Epcc = 4000000psi, MR = 700psi, E_{base} = 21644psi, K_{sub} = 135psi, failure criteria: SCI = 80					
Passes	40	50.7	44.4	55.3	78.1	104.5
Stress (slab/overlay), psi	419.65 / 654.42	407.45 / 637.42	450.09 / 666.87	467.87 / 638.47	370.1 / 692.25	390.08 / 651.2
Variable	Failure Criteria: SCI = 60					
Passes	50.5	64	53.3	66.4	84.5	114.5
Stress (slab/overlay), psi	419.65 / 654.42	407.45 / 637.42	450.09 / 666.87	438.48 / 653.17	370.1 / 692.25	361.99 / 682.79
Variable	Failure Criteria: SCI = 40					
Passes	63.8	80.7	64.5	79.8	92.4	123.6
Stress (slab/overlay), psi	419.65 / 654.42	407.45 / 637.42	450.09 / 666.87	438.48 / 653.17	339.36 / 726.92	361.99 / 682.79

5.2.3.3 Use of SCI to Estimate Reduced Effective Modulus

Observation: This experiment began with intact underlay slabs, but those slabs deteriorated during the testing. The condition of the underlay slabs could not be directly monitored during testing; the instrumentation and the HWD testing provided indications of cracking. Backcalculations from the HWD data did indicate that the effective modulus of the underlay slabs decreased as passes accumulated, as Rolling's SCI model indicates. However, direct comparisons could only be made for the final underlay SCI values as observed after demolition. Therefore, backcalculation results from the overlay were also used as a comparison to the observed SCI values at different points.

Conclusion: The moduli values from backcalculation tended to be significantly larger than those predicted by the Rolling's SCI model for the underlay. The backcalculated values for the overlay were not as sensitive to SCI as the model predictions. Additional values for comparison are needed. The structural distresses were dominated by longitudinal cracking; the results might compare differently for other distress combinations.

Recommendation: The comparison between backcalculated values and the Rolling's SCI model should be compared for additional levels of underlay SCI. Alternate measures of structural capacity or stiffness should also be considered.

5.3 RELATIONSHIP OF RESULTS TO STUDY OBJECTIVES

5.3.1 Overall Unbonded Overlay Roadmap and Research Program

Objective 1: Improve the understanding of how the underlying pavement's condition affects the unbonded overlay's performance. The six test items in the Baseline Experiment were constructed to provide a basis of comparison between the performance of an unbonded overlay on an intact slab and on slabs in various levels of deterioration. This baseline data has been successful collected, and the same underlying slabs remained available in a deteriorated condition for future testing.

Objective 2: Verify whether the measured responses match the predicted responses from the current models and overlay design methods. The measured responses were generally found to be significantly lower in magnitude than those from current models. Further, the number of passes to given levels of deterioration were found to be substantially higher than those from current overlay design methods.

Objective 3: Refine the relationship between the underlying pavement's condition (E-value of the underlying slab) and the structural condition index (SCI) by comparing predicted and actual response data. Two points are available for this relationship from the Baseline Experiment for each test item. Responses and backcalculations were produced for the initial intact condition (SCI = 100) and the condition of each test item's underlay SCI at the conclusion of loading. Additional points can be captured by carrying out the SCI experiment.

Objective 4: Quantify the differences in responses (strains, pressures, and deflections) and the resulting impacts on failure criteria between dual tandem and triple dual tandem gears on unbonded overlay performance. The number of passes to given SCI levels were substantially higher for the comparable test items loaded with the dual tandem gear. From the instrumentation, particularly in the overlay, significant and in some instances full strain recovery was recorded between passes of the tandem axles. This indicates that the overlay is subjected to approximately 1.5 times the number of axle passes for each pass of the triple dual tandem gear as compared to the dual tandem gear.

Objective 5: Improve the understanding of the interaction between the unbonded overlay's system layers (original pavement, interlayer, and overlay). The information collected during the baseline experiment provides the basis for additional insight into how the pavement layers behave, and interact. Observations from crack progression, and vertical deflection "recovery" for the overlay slab during rest periods in loading indicate that complex interactions may be taking place. Further assessment during completion of the Roadmap can contribute significantly to the current observations.

5.3.2 Questions to Be Answered by the Baseline Experiment

Chapter 1.4 about the Baseline Experiment discusses four questions which the experiment should address:

- How does the overlay respond?
- How do underlying discontinuities affect overlay response?
- What is the relative deterioration of the overlay and underlying pavement after loading?
- How do the overlay and underlying pavement deteriorate, in terms of distress and structural response, as compared to Rollings' SCI model?

These questions are very broad in nature, and cannot be fully satisfied by the baseline experiment alone. However, this research represents a strong beginning in obtaining better insight into each of these issues.

Additionally, Chapter 1.4 discusses the focus of analysis for the baseline experiment. Five items are presented:

- Verification of the mechanistic strain predictions in the unbonded overlay,
- Verification of the effects on overlay response of an underlying discontinuity,
- Verification of the failure mechanisms and relative deterioration of the overlay,
- Comparison of the predicted loads to failure with the experimental observations, and
- Verification of the deterioration of the failure mechanisms and distress in the underlying pavement, as a result of the traffic loading.

The construction plan, instrumentation plan, data collection, and analysis performed during this research have attempted to address each of these items. The results of these efforts are not presently clear. While all the work items have been carried out, results to date have been mixed, or variations cannot now be explained. For example, strain responses have been collected for the

unbonded overlay sections constructed. At present, no conclusion has been gained to explain differences between measured and predicted responses. Similarly, verification of failure mechanisms is not clear cut from the observations made.

The development of correlations between traffic loading and distress development were expressed as SCI was accomplished, but correlations are weak. Additional data points will be necessary to better clarify this relationship.

5.4 RECOMMENDATIONS.

5.4.1 Recommendations for Incorporation of Study Results into Design Practice.

The test item performance results from this study should be incorporated with existing data from other tests to verify or calibrate design models for unbonded concrete overlays for airfields. The design pass predictions from current FAA design methodologies are conservative as compared to the performance of these test items. The underlay slabs in this baseline experiment were intact at the initiation of the experiment. This data should be used with subsequent tests on distressed underlay slabs to improve the understanding of the effect of underlay condition on overlay response.

This baseline experiment did incorporate both matched and mismatched transverse joints, but no clear difference in performance or response has been discerned. Therefore, no recommendations can be made for decisions about this design feature.

5.4.2 Lessons Learned for Future Full-Scale Tests of Unbonded Overlays.

A predominant mode of cracking during this study was top-down longitudinal cracking, typically just inside the loading path, but outside the primary loading area. Well-placed, functioning surface strain gages could provide valuable insight into the level of tensile strains producing these cracks. The gages should be placed transversely instead of longitudinally, and should be at a number of transverse locations to assist in establishing the strain distribution.

The initiation of longitudinal top-down cracking has been previously observed, for example CC2, and various explanations for the causes of this crack initiation have been postulated. This longitudinal cracking is cracking resulting from slab corner curling. To enrich the database from the full-scale testing in this regard, it is recommended that additional concrete samples be made for supplemental materials characterization. By measuring flexure strengths and establishing a relationship with the elastic modulus of concrete, a better understanding of this top-down cracking mechanism can be achieved.

The asphalt interlayer may significantly affect the response and performance of the overlay. This was observed in the recovery of the LPTs during nonloading periods, the increase in strain with subsequent axle passes, and the difference in strain magnitude between the top and bottom of the overlay slabs. For future experiments, the thickness of the asphalt interlayer should be more carefully controlled, and material sampled for characterization. If possible, instrumentation

should be installed in the asphalt interlayer. Full-scale testing with interlayer parameter variables was recommended as part of the third stage of the experimental roadmap.

5.4.3 Recommendations for Future Analysis.

The data from this series of test items provide a rich resource for analysis. The data provide the baseline for subsequent stages in the experimental roadmap. The data will enable direct comparison of the responses from these cross-sections that were constructed on intact underlay slabs to the responses from later tests on distressed slabs.

Extensive additional analysis is possible with the instrumentation data. Only a portion of the data has been extracted as part of this study. Even the responses already examined can be further characterized. For example, only the peak strains have been directly considered in this analysis; the variation in responses with adjacent axles or with direction of loading should be evaluated in greater depth.

The experiment constructed, and the information collected, provides initial data points for evaluation of unbonded overlay performance during the initial stages of bottom slab deterioration. To increase the value of the experiment considerably more analysis will be required. Some of this analysis will be addressed in the integrated analysis planned for the structural condition index portion of the experiment, but additional in-depth analysis on a larger scale will continue to increase understanding of this design concept which offers many practical benefits.

5.4.4 Recommendations for Completion of the Roadmap

While this baseline experiment has provided a platform of reference information about the performance of unbonded concrete overlays, it provides only two points on the pavement deterioration curve. Further, the first point is that at which bottom slab SCI equals 100, which is unlikely to occur in practice. The conduct of additional phases identified in the Roadmap document are needed to provide sufficient additional information to make meaningful use of the data collected for the baseline condition.

Observations from vertical deflection responses from LPT instrumentation showed that when rest periods occurred during the loading phase of the experiment, the downward movement of the top slab observed during load application was reversed. Similar recovery was not observed in the bottom slab, and has been attributed to viscoelastic properties of the asphalt interlayer material. Additional investigation into this observation, and perhaps comparison with other interlayer material could add significantly to the understanding of this observed performance, and its relationship to the service life of unbonded concrete overlays.

To fully realize the benefit of the work completed so far, it is important that additional testing and evaluation be carried out. This effort has opened several new doors of inquiry, but there is much more work needed to reach full understanding of these issues.

REFERENCES

Rollings, R.S., *Design of Overlays for Rigid Airport Pavements*, FAA Report No. DOT/FAA/PM-87/19, Final Report 4/1988.

Brill, D.R., I Kawa, and G.F. Hayhoe, *Modeling Rigid overlays in FAA Thickness Design Procedures Using Three-dimensional Finite Element Methods*, 16th ASCE Engineering Mechanics Conference, July 16-18, 2003, University of Washington, Seattle, WA.

Guo, E., L. Ricalde, and I. Kawa, *FAA Finite Element Design Procedure for Rigid Pavements* (DRAFT), September 2005.

Khazanovich, L., *Improved Concrete Overlay Design Parameters for Airfield Pavements Report*, DOT/FAA-01-G-002-2, published by the Innovative Pavement Research Foundation for the Aviation Administration, Washington, D.C., 2001.

Mack, J., S. Stoffels, D. Morian, S. Wu, and A. Ioannides, *Improved Overlay Design Parameters for Concrete Airfield Pavements, 20% Report*, Innovative Pavement Research Foundation (IPRF) Project FAA-01-G-002-04-02, 2006.

Trost, S., G. Fick, J. Hunt, B. Post, and J. Pruitt, *Using Maturity testing for Airfield Concrete Pavement Construction Repai*r, Report IPRF-01-G-002-03-6, 2006.

Ye, D., D.G. Zollinger, and D.A. Morian, *Characterization and Analysis of Early Age Concrete Pavement Behavior at the National Airport Pavement Test Facility (NAPTF)*, Report IPRF 01-G-002-04-2(s), 2007(r).

ASTM Standard D5340, 2004el, "Standard Test Method for Airport Pavement Condition Index Surveys," ASTM International, West Conshohocken, PA, www.astm.org.

Khazanovich, L., *Structural Analysis of Multi-Layered Concrete Pavement Systems*, Ph.D. Thesis, Univesity of Illinois at Urbana-Champaign, Urbana, Illinois, 1994.

Ioannides, A.M., L. Khazanovich, and J.L. Becque, *Structural Evaluation of Base Layers in Concrete Pavement Systems*, Transportation Research Record No. 1370, Transportation Research Board, National Research Council, Washington, D.C., 1992.

Software for the 3D Finite Element Analysis of Jointed Plain Concrete Pavements, http://www.civil.umaine.edu/EverFE/, February 2003.

Navneet G., E. Guo, and R. McQueen, *Operational Life of Airport Pavements*, Report No. DOT/FAA/AR-04/46, U.S. Department of Transportation, Federal Aviation Administration, Washington, D.C., December, 2004.